LISTENING TO THE INTERNAL REPRESENTATION OF ACTIONS WITHIN THE POSTERIOR PARIETAL CORTEX

Thesis by

Whitney Griggs

In Partial Fulfillment of the Requirements for the

Degree of

Doctor of Philosophy

CALIFORNIA INSTITUTE OF

TECHNOLOGY

Pasadena, California

2023

(Defended April 12, 2023)

Whitney Griggs
ORCID: 0000-0003-2941-6803

Dedication

“I only went out for a walk and finally concluded to stay out till sundown, for going out, I found, was really going in.” – John Muir

Dedicated to James LaFortune, for inspiring me to become a physician scientist.

Acknowledgments

My motivation for my graduate work traces back to 2003 when I read about a scientist who controlled a robotic hand using electrodes surgically implanted in his forearm's median nerve. This neuroprosthetic sparked my imagination and drive to create a future that merged man and machine. Following the death of a family friend from brain cancer in 2010, I realized I wanted to become a physician and directly help patients regain and maintain their health. My dual interests in patient care and neuroprosthetics inspired me to become a restorative neurosurgeon developing brain-machine interfaces that restore lost function and improve quality of life in people with neurological impairments. I cannot adequately thank all the people who have helped me work towards this goal, but I would like to express gratitude to those most instrumental to my success at Caltech.

First, I would like to thank my advisor, Richard Andersen, for this truly amazing opportunity to work on brain-machine interface research, helping fulfill a childhood dream. Throughout my time at Caltech, you have been dedicated to my success, provided indispensable advice for my research projects, and provided me the space to develop as an independent neuroscientist. I would also like to thank Mikhail Shapiro for co-advising me and providing insightful feedback on my countless grant applications, research projects, and data presentations. I would like to thank my immediate mentor, Sumner Norman. You always had time for my questions. You taught me how to make my code reproducible and catapulted my scientific writing and data presentation skills to new levels. Thank you also for teaching me that things catching on fire (metaphorically, luckily) just means the Universe is trying to hide its secrets from me. I additionally want to thank the other members of my thesis committee, Ueli Rutishauser, Ralph Adolphs, and John O'Doherty, for their perceptive feedback and critical evaluation of my work.

I would like to thank all my lab's collaborators who provided thoughtful advice and guidance on my projects: Vasileios Christopoulos, for the discussions that lead to my Ph.D. projects; Mickael Tanter, for giving me a thorough understanding of ultrasound principles; Claire Rabut, for being a constant fountain of optimism and ultrasound knowledge; and Charles Liu and Ausaf Bari for neurosurgery advice.

Thank you to all my friends and colleagues at Caltech for all the great conversations, happy hour discussions, and memories: Kelly Kadlec, Sarah Wandelt, Charles Guan, Isabelle Rosenthal, Varun Wadia, Geeling Chau, Srinivas Chivukula, Mackenzie Thurston, and HyeongChan Jo for being the best fellow graduate students I could have asked for; Tyson Aflalo, Spencer Kellis, Luke Bashford,

David Bjånes, and Jorge Gamez for helping me develop my research ideas and experimental designs; Xinyun Zou, Liang She, and Thierri Callier for academic discussions; the Shapiro neuroscience subgroup members for constant feedback on my results and suggestions for future experiments; and Viktor Shcherbatyuk and Kelsie Pejsa for technical and administrative support.

Thank you to my fellow MD and MD-PhD classmates, especially Sabrina Levy, Jay Gill, and Hristos Courellis for discussions of clinical neuroscience; David Okikawa for advice about medical school and enabling my running addiction; Matiar Jafari, Prashant Bhat, Shannon Esswein, Sam Schulte, and Alex Viloria-Winnett for advice about navigating Caltech.

Thank you to our human subject, J.H., for always being willing to come to Caltech and participate in repetitive experiments.

Thank you to my running friends in Los Angeles who gave me an outlet from research. Anthony for introducing me to the Run With Us crew and Gabriele, Kate, Jaime, Daniel, Leamon, Rich, Kyle, Austin, and Domenico for supporting me throughout my knee injury and challenging me to run further and faster than I thought I could.

None of this would have been possible without my family. Thank you to my parents, Ann and Tom, for believing in me constantly, giving me countless opportunities throughout my life to explore my interests, and teaching me to be always inquisitive. Thank you to my brother, Russell, for being my role model throughout my life and inspiring me to always give 110% in anything I do. Thank you to my grandparents, Austen and Claire for telling me stories about their sabbatical in idyllic Caltech and Pasadena, Tutu for teaching me to be worldly and have well-informed opinions, and Walter for demonstrating how to have a long career as a compassionate physician.

My heartfelt gratitude to my wife, Mackinzie, for constantly supporting me and being a source of inspiration. Thank you for encouraging good work-life balance by being my adventure buddy on lots of crazy outdoor adventures. Your love and support gave me the strength and motivation to persevere through the hardest parts of the PhD.

Finally, I would like to acknowledge the National Institutes of Health, the Tianqiao and Chrissy Chen Institute for Neuroscience, and Josephine de Karman Fellowship for believing in my projects and providing the funding that supported this work.

Abstract

More than 5.4 million people in the United States live with chronic paralysis and roughly 20 million people worldwide live with spinal cord injuries. Brain-machine interfaces (BMIs) can be transformative for these people, enabling them to control computers, robots, and more with only thought. State-of-the-art BMIs have already made this future a reality in limited clinical trials. However, these state-of-the-art BMIs have shortcomings that limit user adoption; high-performance BMIs currently require highly invasive electrodes above or in the brain; device degradation limits longevity to about 5 years; and their field of view is small, restricting the number, and type, of applications possible. This illustrates the need for a new generation of BMIs with a brain recording modality that is longer lasting, less invasive, and scalable to sense activity from large regions of the brain.

Functional ultrasound imaging (fUSI) is a recently developed technique that meets these criteria. fUSI measures cerebral hemodynamics with exceptional spatiotemporal resolution (<100 μm; ~100 ms) and a large field of view (several cm)—specifications ideally suited to recording detailed activity of entire cortical regions in parallel. In a series of novel results, we work towards developing the first high-performance ultrasonic BMI for human use. We first demonstrate that posterior parietal cortex (PPC), an area important for sensorimotor transformation, contains mesoscopic populations tuned to the intended movement direction. Using offline recorded data from several rhesus macaque monkeys, we can decode intended movement direction, task state, and expected action reward magnitude on a single trial basis. Having demonstrated that we could decode a variety of motor and cognitive variables using offline data, we developed a real-time, closed-loop ultrasonic BMI capable of decoding up to eight directions of intended movement with high accuracy. Finally, we began to translate these results into human applications and demonstrate the ability to measure changes in cerebral hemodynamics with high sensitivity through an acoustically transparent skull replacement in human subjects.

Taken together, our work is a novel characterization of how functional ultrasound neuroimaging may enable a new generation of BMIs. Additionally, this work reinforces the validity of fUSI as a robust and accessible neuroimaging technique for future neuroscience questions about mesoscopic populations and their interrelationships throughout the brain.

Published Content and Contributions

Norman, SL, et al. 2021. Single-trial decoding of movement intentions using functional ultrasound neuroimaging. *Neuron*. 10.1016/j.neuron.2021.03.003.

WG participated in the collection of the data and in the editing of the manuscript.

Griggs, WS and Norman SL, et al. 2022. Decoding motor plans using a closed-loop ultrasonic brain-machine interface. *bioRxiv*. 10.1101/2022.11.10.515371.

WG participated in the conception, analysis, and interpretation of the data, as well as in the writing of the manuscript.

Table of Contents

Dedication ..... **iii**

Acknowledgments ..... **iv**

Abstract ..... **vi**

Published Content and Contributions ..... **vii**

Table of Contents ..... **viii**

List of Illustrations, Tables, and Movies ..... **xii**

Commonly Used Acronyms ..... **xiv**

1 Introduction **1**

2 Background **5**

2.1 Brain-machine interfaces (BMIs) **5**

2.1.1 Definition 5

2.1.2 Example BMI applications 5

2.1.3 Obstacles for broad adoption 6

2.2 Brain recording techniques for large animals and humans **6**

2.2.1 Electrical 7

2.2.2 Magnetic 10

2.2.3 Optical 11

2.2.4 Ultrasound 13

2.3 Posterior parietal cortex (PPC) **16**

2.3.1 Encoding of effector 16

2.3.2 Encoding of direction 17

2.3.3 Encoding of non-motor signals 17

2.3.4 BMI applications 18

2.4 Relevant previous fUSI results **18**

2.4.1 Single-trial decoding of direction, task state, and effector 18

3 Topographic organization of direction within posterior parietal cortex **28**

3.1 Background **28**

3.2 Results **29**

3.2.1 Are there mesoscopic populations tuned to different directions? 30

3.2.2 How consistent is this directional tuning within a session? 33

3.2.3 Are these mesoscopic populations stable across multiple days? 36

3.2.4 How does mesoscopic population tuning change across anterior and posterior portions of PPC? 39

3.3 Discussion **43**

3.3.1 Sensitivity of fUSI 43

3.3.2 Anterior-posterior gradient ... 43
3.3.3 Preference for contralateral space ... 45
3.3.4 Differences between dorsal and ventral LIP ... 45
3.3.5 Directional saccadic activity outside of LIP ... 45
3.3.6 Stability across time ... 46
3.3.7 Applications to ultrasonic brain-machine interfaces ... 47
3.3.8 Future studies and questions ... 48
3.4 Conclusion ... 50
3.5 Materials and Methods ... 51
3.5.1 Experimental model and subject details ... 51
3.5.2 General ... 51
3.5.3 Functional ultrasound imaging ... 52
3.5.4 Across session alignment and concatenation ... 52
3.5.5 – 3D visualization ... 53
3.5.6 Quantification and statistical analysis ... 53
3.6 Extended Data ... 57
3.6.1 Supplemental figures ... 57
3.6.2 Supplemental movies ... 61

4 Decoding of non-directional signals from PPC ... 62
4.1 Background ... 62
4.2 Results ... 63
4.2.1 Decoding of task state ... 63
4.2.2 Behavioral evidence of learning object outcome associations ... 66
4.2.3 Reward magnitude ... 68
4.3 Discussion ... 71
4.3.1 Decoding task state ... 71
4.3.2 Encoding of reward magnitude within PPC ... 75
4.3.3 Novelty ... 76
4.3.4 Effort ... 76
4.3.5 Future work ... 77
4.3.6 Conclusion ... 77
4.4 Materials and Methods ... 78
4.4.1 Experimental model and subject details ... 78
4.4.2 General ... 78
4.4.3 Functional ultrasound imaging ... 79
4.4.4 Across session alignment and concatenation ... 80
4.4.5 Quantification and statistical analysis ... 80
4.4.6 Within-session decoding analysis ... 81
4.4.7 Searchlight analysis ... 82
4.5 Extended Data ... 83
4.5.1 Supplemental movies ... 83

5 Decoding Motor Plans Using a Closed-Loop Ultrasonic Brain-Machine Interface . 84
5.1 Background ... 84
5.2 Results ... 85
5.2.1 Online decoding of two eye movement directions ... 87
5.2.2 Online decoding of eight eye movement directions ... 90
5.2.3 Online decoding of two hand movement directions ... 94

5.3 Discussion ... **98**
5.3.1 Decoding more movement directions ... 98
5.3.2 Stabilizing decoder across time ... 98
5.3.3 Improving performance ... 99
5.3.4 Advantages of fUS neuroimaging ... 100
5.3.5 Decoding hand, eye, or both? ... 101
5.3.6 Moving beyond a motor BMI ... 101
5.4 Materials and Methods ... **103**
5.4.1 Experimental model and subject details ... 103
5.4.2 General ... 103
5.4.3 Animal preparation and implant ... 103
5.4.4 Behavioral setup ... 103
5.4.5 Behavioral tasks ... 103
5.4.6 fUS-BMI ... 104
5.4.7 Across-session alignment ... 107
5.4.8 Quantification and statistical analysis ... 108
5.5 Extended Data ... **109**

6 Window to the Brain: Ultrasound Imaging of Human Neural Activity Through a Cranial Implant ... **112**
6.1 Background ... **112**
6.2 Results ... **116**
6.2.1 In vitro performance comparison ... 116
6.2.2 Functional activity comparison in rodent model ... 117
6.2.3 fUSI through decompressive craniectomy window ... 120
6.2.4 Cranial implant design for Patient J ... 121
6.2.5 First non-invasive fUSI activity recording in human through cranial implant ... 122
6.3 Discussion ... **125**
6.3.1 Diagnostics & monitoring after skull reconstruction (clinical use) ... 125
6.3.2 BMI & neuroscience (research use) ... 126
6.3.3 Future work ... 126
6.4 Conclusion ... **127**
6.5 Materials and Methods ... **127**
6.5.1 General ... 127
6.5.2 Implant materials ... 127
6.5.3 Functional ultrasound imaging ... 128
6.5.4 In vitro tissue anatomical and doppler phantoms ... 128
6.5.5 In vivo functional ultrasound imaging comparative study in rat ... 128
6.5.6 fUSI data processing ... 129
6.5.7 Decompressive hemicraniectomy and reconstruction procedure ... 129
6.5.8 Skull implant design ... 130
6.5.9 Human participant ... 130
6.5.10 Human fUSI task ... 130
6.5.11 Task decoding ... 131

7 Conclusion ... **132**
7.1 Summary of current work ... **132**
7.2 Future directions ... **134**
7.2.1 Neuropsychiatric BMIs for treating mood disorders ... 134

7.2.2 4D fUSI-BMI 135
7.2.3 fUSI-guided electrophysiology 136
7.3 Final thoughts 136

8 Bibliography 138

List of Illustrations, Tables, and Movies

Figure 2.1 Functional ultrasound enables mesoscopic imaging of neural populations 6
Figure 2.2 Functional ultrasound creates high-resolution, high-sensitivity Power Doppler images. 14
Figure 2.3 PPC is organized by different movement effectors..... 16
Figure 2.4 Anatomical imaging regions..... 19
Figure 2.5 Single-trial decoding of intended movement direction. 21
Figure 2.6 Decoding task, effector, and direction simultaneously. 23
Figure 2.7 Effects of spatial resolution, time window, and mean power Doppler intensity. 24
Figure 3.1 Monkeys perform memory-guided saccade task during fUSI acquisition. 30
Figure 3.2 PPC contains multiple distinct directionally-tuned mesoscopic populations. 32
Figure 3.3 Single-trial decoding of eight intended movement directions with high accuracy. 35
Figure 3.4 PPC stably encodes movement direction across many months to years. 38
Figure 3.5 Polar direction is topographically organized along anterior-posterior axis of LIP. 40
Supplemental Figure 3.1 Stability of directional preference across time..... 57
Supplemental Figure 3.2 Impact of image similarity on decoder performance. 58
Supplemental Figure 3.3 Linear decoders can decode intended movement direction from most fUSI sessions, regardless of PPC plane..... 59
Supplemental Figure 3.4 Power Doppler data displays spatial autocorrelation. 60
Supplemental Movie 3.1 Anatomy in Monkey P 61
Supplemental Movie 3.2 Anatomy in Monkey L 61
Figure 4.1 Complex spatiotemporal patterns across PPC during saccade task states. 64
Figure 4.2 High decoding accuracy for individual task states using single Power Doppler images. 65
Figure 4.3 Memory-guided saccade task variant with complex visual cues..... 68
Figure 4.4 Distinct mesoscopic PPC populations encode for reward magnitude. 70
Supplemental Movie 4.1 Example trial averaged activity..... 83
Figure 5.1 Anatomical recording planes and behavioral tasks. 86
Figure 5.2 Example sessions decoding two saccade directions. 88
Figure 5.3 Performance across sessions for decoding two saccade directions. 90
Figure 5.4 Example sessions decoding eight saccade directions. 92
Figure 5.5 Performance across sessions for decoding eight saccade directions. 94
Figure 5.6 Example sessions decoding two reach directions. 95
Figure 5.7 Performance across sessions for decoding two reach directions. 96
Supplemental Figure 5.1 Across session alignment algorithm. 109

Supplemental Figure 5.2 Closed-loop, real-time decoding of movement directions using pretrained model only. 110

Supplemental Figure 5.3 TCP Communication Architecture for real-time fUS-BMI..... 111

Figure 6.1 Functional ultrasound enables brain imaging in freely behaving subjects with high spatiotemporal resolution and large coverage. 115

Figure 6.2 Polymeric skull replacement materials enable power Doppler imaging with minimal SNR loss in an in vitro blood flow phantom..... 117

Figure 6.3 Acoustic window materials enable sensitive *in vivo* rodent fUSI imaging..... 119

Figure 6.4 Ultrasound enables vascular imaging through intact scalp after craniectomy..... 121

Figure 6.5 Patient J was reconstructed with a custom-designed acoustic window..... 122

Figure 6.6 Permanent acoustic window allows non-invasive fUSI. 124

Figure 6.7 Permanent acoustic window allows fUSI detection of guitar playing. 125

Commonly Used Acronyms

BMI: Brain-machine interface
CBV: Cerebral blood volume
fUSI: Functional ultrasound imaging
GLM: General linear model
ips: intraparietal sulcus
iti: intertrial interval
LFP: Local field potential
LIP: Lateral intraparietal area
MEA: Multi-electrode array
MIP: Medial intraparietal area
PPC: Posterior parietal cortex
PRR: Parietal reach region
ROI: Region of interest
SNR: Signal-to-noise ratio

1 Introduction

Motor actions require exceptional visual-motor coordination executed with precise spatial and temporal accuracy, such as the orchestrated action of a pianist's eyes, fingers, and feet while they read and play music. Complex neuronal circuits across multiple brain regions, including the posterior parietal cortex (PPC), represent these visual cues and associated movements. Within these complex circuits, PPC is believed to integrate visual information, represent possible action plans, and decide upon the optimal action for downstream execution (Colby and Duhamel, 1996; Snyder et al., 1997; Whitlock, 2017). These vital roles were first postulated by clinicians in 1909 when Dr. Bálint reported that bilateral parietal lobe damage impaired visually-guided reach accuracy (optic ataxia), eye movements (oculomotor apraxia), and visual perception (simultagnosia) (Bálint, 1909; Andersen et al., 2014; Parvathaneni and Das, 2020). Extensive animal and human studies have further established and elucidated PPC's role in planning movements (Fleming and Crosby, 1955; Yin and Mountcastle, 1977; Andersen et al., 1985; Gnadt and Andersen, 1988; Snyder et al., 1997; Cui and Andersen, 2007; Whitlock, 2017).

Approximately 5.4 million people worldwide live with chronic paralysis and are not able to complete these spatiotemporally precise motor actions that we usually take for granted (Armour et al., 2016). Brain-machine interfaces (BMIs) can be transformative for these people by enabling them to control computers, robots, and more with only thought. At its essence, brain-machine interfaces measure brain signals and use these signals to control external devices. State-of-the-art BMIs have already enabled a small number of these patients to regain some of their quality of life (Hochberg et al., 2006; Collinger et al., 2013; Aflalo et al., 2015; Anumanchipalli et al., 2019; Willett et al., 2021, 2023). BMIs need to record from brain regions involved in movement planning to decode the user's intended actions. The PPC is a good candidate region. Because the PPC encodes for a breadth of action-related variables, including goals of movements and movement trajectory, it enables a diversity of BMI applications (Andersen et al., 2019), including speech generation, decoding limb and finger movements, and computer cursor control (Musallam et al., 2004; Mulliken et al., 2008; Hwang and Andersen, 2009; Hauschild et al., 2012; Aflalo et al., 2015; Klaes et al., 2015; Andersen et al., 2019; Guan et al., 2022a, 2022a; Wandelt et al., 2022a).

However, existing state-of-the-art BMIs have shortcomings that limit user adoption; high performance BMIs currently require highly invasive electrodes above or in the brain; device degradation limits longevity to about 5 years (Bullard et al., 2020; Sponheim et al., 2021); and their field of view is small, restricting the number, and type, of applications possible. Less invasive techniques, such as EEG, offer substantially lower spatial resolution and cannot resolve signals below the brain surface, thus limiting their utility as a sensing technique for BMIs. This illustrates the need for a new generation of BMIs with a brain recording modality that is longer lasting, less invasive, and scalable to sense activity from large regions of the brain.

Functional ultrasound imaging (fUSI) is a recently developed ultrafast ultrasound technique that meets these criteria. Ultrafast ultrasound uses plane-wave pulse-echo transmissions ("one-shot"-"one-image") to acquire thousands of images per second and thus image transient phenomena (millisecond range) deep inside organs. This differs from the sequential focused beams commonly used in clinical ultrasonography. Combining ultrafast sonography with coherent compounding of tilted planar ultrasound illuminations enabled accurate measurement of transient changes in cerebral blood volume (CBV) (Macé et al., 2011). fUSI measure changes in CBV with high sensitivity, exceptional spatiotemporal resolution (100 µm; ~100 ms), deep brain coverage (2-7 cm), and a large field of view (several cm) (Montaldo et al., 2022) – specifications ideally suited to recording detailed mesoscopic activity of entire cortical regions in parallel. These hemodynamics reflect neuronal activity through neurovascular coupling (Mosso, 1881; Attwell et al., 2010; Macé et al., 2011; O'Herron et al., 2016; Bergel et al., 2018; Boido et al., 2019; Aydin et al., 2020; Nunez-Elizalde et al., 2022).

In this present work, we used fUSI to examine the mesoscopic representation of actions within PPC and develop the first high performance ultrasonic BMI. This work not only answers open neuroscience questions about the functional organization of PPC, but also contributes to our understanding of the pathophysiology of neurological disorders caused by PPC damage (e.g., optic ataxia and oculomotor apraxia) and begins developing a next generation of BMIs that are high-performing, minimally-invasive, long-lasting, and able to measure neural signals from large (or even separate) brain regions.

In **Chapter 2**, we provide relevant background on response properties of PPC, recording technologies for large animals and humans, fUSI, and BMIs. We also briefly discuss previous work on using fUSI for decoding information on single trials using offline data.

In **Chapter 3**, we identify mesoscopic populations tuned to individual directions. These populations were stable across more than 100-900 days and displayed a rough topography along an anterior-posterior axis. These results address a fundamental gap in our understanding of PPC's functional organization by developing mesoscopic maps of directional tuning previously unattainable with fMRI (poor resolution) or electrophysiology (poor coverage) methods.

In **Chapter 4**, we explore how non-directional information about future actions is represented within PPC. We first show that we can robustly decode multiple different task states in a memory-guided saccade task, supporting feasibility of a freely paced fUSI-BMI. We next identify robust value signals within mesoscopic PPC populations of one monkey. Higher rewarded actions were associated with increased hemodynamic activity. This chapter contributes to the development of a versatile closed-loop fUSI-BMI by showing that fUSI can decode non-directional signals, i.e., expected reward magnitude and current task state. This suggests that fUSI should be able to decode a variety of cognitive brain states, such as emotions, from the brain and be used as the sensing technique for a 'mood BMI' that models and decodes mood variations in real-time.

In **Chapter 5**, we present our work on developing the first high-performance, closed-loop ultrasonic BMI. We demonstrate that we can decode at least eight directions of intended movements. Building off **Chapter 3**, we develop a method to pretrain the decoder model and demonstrate that our ultrasonic BMI is stable across >30 days without retraining. This work establishes the feasibility of a real-time fUSI-BMI and prepares for future work translating this work into clinical applications that restore mobility to patients with neurological or psychiatric impairments.

In **Chapter 6**, we present our work on developing fUSI for awake, moving humans with a sonolucent skull replacement. We first characterize the skull replacement material in an *in vitro* setting and demonstrate that we can image through a variety of thicknesses. We next test the functional sensitivity in a visual experiment using rats. We finally demonstrate that we can detect task-related activity using fUSI in an awake human participant.

In **Chapter 7**, we summarize our results and describe future research directions. Together, these chapters help elucidate where motor and decision variables are encoded in PPC at the meso-scale (fUSI). These results also establish that fUSI is a highly sensitive method that can serve as a next generation of less-invasive, yet high-performing, BMIs. Through these monkey and human experiments, we developed a deeper understanding of the mesoscopic PPC circuits involved in motor

and cognitive decisions. This will enable future work to better decode intended actions and mood states using fUSI and develop a human fUSI-BMI.

2 Background

2.1 Brain-machine interfaces (BMIs)

2.1.1 Definition

Brain-machine interfaces (BMIs) enable direct communication between the brain and external devices. BMIs are broadly classified as either input or output devices. Input BMIs add external signals back into the brain, such as sensory information, while output BMIs read signals out from the brain and use these signals to control external devices, including robotic arms, computer cursors, and speech predictors. The long-term goal is to develop bidirectional BMIs that are capable of both input and output. This would allow sensory feedback from any externally controlled device, including proprioception, pain, pressure, temperature, and texture.

2.1.2 Example BMI applications

2.1.2.1 Input

Most input BMIs replace sensory information, including vision, hearing, and touch. The most common BMI is a cochlear implant with approximately 200,000 devices implanted in the United State and 750,000 devices implanted worldwide (Anon, 2021). First developed in the early 1960s, cochlear implants are a type of input BMI that restores hearing to people with partial to complete hearing loss. It uses multi-electrode arrays to directly stimulate the cochlear nerve, thus bypassing damage or lack of development of the middle or inner ear (Rao, 2020).

More recently, researchers have made progress in using electrode-based BMIs to evoke naturalistic sensations (Flesher et al., 2016, 2021; Armenta Salas et al., 2018; Callier et al., 2020; Bjånes et al., 2022; Fifer et al., 2022) and restore vision in humans (Beauchamp et al., 2020; Chen et al., 2020).

2.1.2.2 Output

Applications for output BMIs are likely only limited by the imagination. Since BMIs learn the mapping between neural activity and the desired activity, humans can be trained to control a variety of different effectors with their brain. Currently, output effectors have been focused on speech and movement decoding. These areas of focus are likely due in part to invasive BMIs being limited to patients with partial to complete paralysis, such as patients with spinal cord injuries or amyotrophic lateral sclerosis (ALS). In these patients, recent work has demonstrated that the motor representation within PPC is consistent before and after paralysis (Guan et al., 2022b). These motor representations

of arm and hand movements have been used by many groups to enable dexterous control of robotic limbs (Hochberg et al., 2006; Collinger et al., 2013; Aflalo et al., 2015). Some notable recent examples include decoding handwriting (Willett et al., 2021), decoding external speech (Anumanchipalli et al., 2019; Moses et al., 2021; Willett et al., 2023), decoding individual finger movements (Guan et al., 2022a), and decoding internal speech (Wandelt et al., 2022a).

2.1.3 Obstacles for broad adoption

Despite how impressive output BMIs have become, state-of-the-art output BMIs currently require invasive electrodes below the dura or in the brain, limiting the number and type of applications possible. Electrode-based BMIs suffer from additional factors that further limit the technology's adoption to a broader patient population. These include device degradation limiting the BMI's longevity to typically around 5 years (Bullard et al., 2020; Sponheim et al., 2021) and the implants only sampling from small regions of superficial cortex. An ideal BMI technology would be non-invasive, long-lasting, sensitive to rapid changes in small groups of neurons, and able to image from multiple large cortical and subcortical brain regions simultaneously.

2.2 Brain recording techniques for large animals and humans

BMIs need to measure brain signals from the brain. A variety of methods exist for recording brain activity in large animals, including humans. These methods vary in terms of invasiveness, spatiotemporal resolution, spatial coverage, specificity for neuronal activity, cost, portability, and other factors. Recording methods can be broadly categorized by the type of signal they detect and measure: electrical, magnetic, optical, or acoustic.

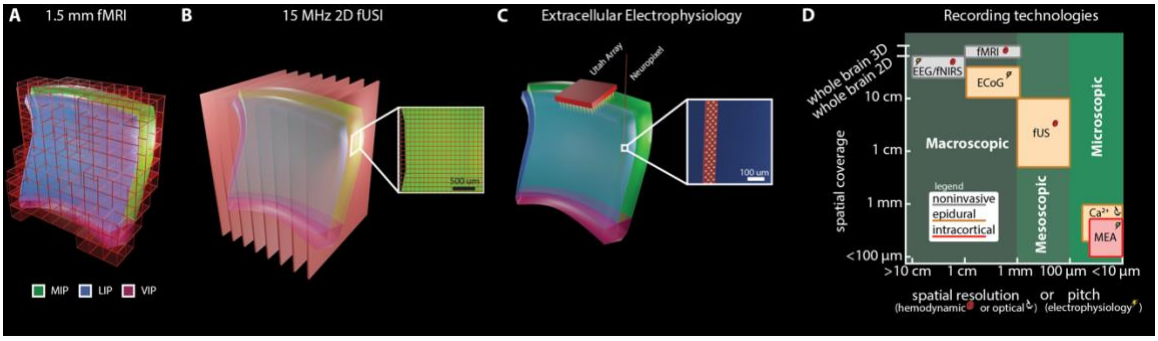

Figure 2.1 Functional ultrasound enables mesoscopic imaging of neural populations
(A) 1.5 mm isotropic fMRI. Each box represents one voxel. (B) 15.6 MHz 2D fUSI. Each red sheet represents one coronal imaging plane. Inset shows 100 µm x 100 µm voxel size. (C) Utah array and Neuropixel recording methods for recording from intraparietal sulcus. (D) Comparison of spatial resolution and spatial coverage for each method.

2.2.1 Electrical

The most direct way to monitor brain activity is to measure the electrical activity directly emanating from neurons. These sensing modalities can be non-invasive (EEG), minimally-invasive (ECoG), or highly invasive (intracortical electrodes).

2.2.1.1 Electroencephalography (EEG)

Electroencephalography (EEG) is one of the oldest, if not the oldest, technique for measuring brain activity. Non-invasive electrodes are placed across the scalp and record voltage fluctuations. It is believed these voltage fluctuations represent an attenuated and transformed version of the local field potentials resulting from pyramidal neurons in the cortex (Lopes da Silva, 2013, Anon, 2023a). Although EEG can record temporally precise activity from across the entire scalp, it is difficult to accurately estimate the cortical sources of the electrical fields detectable at the scalp (Lopes da Silva, 2013). This limits EEG's spatial resolution (**Figure 2.1D**) even with high numbers of EEG electrodes.

The first output brain-machine interface (BMI) used EEG and could achieve a one-bit decode (Nowlis and Kamiya, 1970). Scalp EEG has since been used to decode individual trials and control BMIs with higher bit-rates (Wolpaw et al., 1991; Wolpaw and McFarland, 2004; Norman et al., 2018). Performance of modern EEG BMIs varies greatly across users (Ahn and Jun, 2015) but can yield two degrees of freedom with 70%–90% accuracy (Huang et al., 2009).

2.2.1.2 Electrocorticography (ECoG)

Electrocorticography (ECoG), a type of intracortical EEG (iEEG), is a minimally-invasive technique where a grid of electrodes is surgically placed epidurally or subdurally above the brain region(s) of interest. As with scalp EEG, voltage fluctuations from LFPs are measured. However, the measured signal more directly reflects the neuronal activity because there are not as many layers of tissue (including bone) to attenuate and transform the electrical signals. These grids of electrode arrays generally have better spatial resolution than EEG, but sample from a smaller region of the brain (**Figure 2.1D**).

Subdural and epidural ECoG arrays have different risk profiles. Epidural ECoG is believed to be safer because it is part of the peripheral immune system and reduces the risk of infection within the central nervous system (Mollman and Haines, 1986; Korinek, 1997). Both types of ECoG generally have immune responses that lead to granulation tissue, glial scarring, and signal degradation across time (Schendel et al., 2014; Kozai et al., 2015; Alahi et al., 2022).

Micro-ECoG arrays have been developed that have a much smaller distance (i.e., pitch) between electrodes (Hosp et al., 2008; Kellis et al., 2016; Konerding et al., 2018). These are believed to be better for a number of neuroscience applications, including BMIs (Wang et al., 2009), and have even been able to detect action potentials (Khodagholy et al., 2015, 2016). Although epidural ECoG is preferable from a risk standpoint, subdural ECoG has better signal quality, especially for micro-ECoG (Bundy et al., 2014).

Epidural and subdural ECoG arrays have been used for a number of high-performance BMIs, including speech decoding (Moses et al., 2021) and movement decoding (Spüler et al., 2014; Benabid et al., 2019). The speech BMIs could decode approximately 12-15 words/minute or 29 character/minute (Moses et al., 2021; Metzger et al., 2022). The movement BMIs were capable of decoding eight degrees of freedom at ~70% accuracy (Benabid et al., 2019). ECoG arrays can additionally record stable signals across many months, if not years, thus reducing the need for daily recalibration (Moses et al., 2021).

Recently, endovascular electrodes have been developed that have similar signal quality to subdural and epidural ECoG arrays (John et al., 2018). These endovascular electrodes require much less invasive procedures to place (endovascular access instead of brain surgery). However, they can only be placed in blood vessels of at least 1 mm diameter, limiting which brain regions can be accessed (Oxley et al., 2018). Additionally, endovascular electrodes currently have much lower information transfer rates (~12 character per minute) than ECoG BMIs (Oxley et al., 2021).

2.2.1.3 Intracortical electrode(s)

Intracortical electrodes are invasive electrodes inserted into the brain to record action potentials and LFPs from nearby neurons. While activity from single neurons can be isolated using intracortical electrodes, these electrodes can only record from very small volumes of the brain (**Figure 2.1C, D**). Additionally, a craniotomy is required above the area of interest to allow the intracortical electrode access. Traditionally, researchers inserted a single microelectrode through the cranial opening into the brain and used a micromanipulator to precisely control the depth of the electrode. With the assistance of an audio monitor or computer software, researchers could then precisely position the microelectrode to isolate and record neurons of interest. As technology advanced, multi-electrode arrays (MEAs) became available, enabling researchers to record from multiple electrodes simultaneously. Recording from multiple electrodes not only allowed more neurons to be recorded during a single electrode penetration, but also enabled better isolation of individual neurons' activity

and simultaneous recording of the activity of multiple neurons. These MEAs are either a linear electrode array, a grid of electrodes, or a combination of the two. A linear electrode array has all the electrodes spaced along a shank, allowing the depth of the shank to be controlled but no adjustment of the individual electrode positions relative to each other. High-density linear electrode arrays, e.g., Neuropixels, now exist that allow simultaneous recording (~30 KHz) of >300 channels spaced along a 10-40 mm silicon shank (**Figure 2.1C**). The electrode grids have the electrodes spaced across a grid, i.e., the electrodes are all parallel to each other rather than along a linear shank. Some of these electrode grids allow the researcher to control the depth of individual electrodes (Dotson et al., 2017).

In humans, the most common type of chronic intracortical electrode used for neuroscience research and BMI applications is the Utah array, a 4.2 mm square grid with 100 evenly-spaced microelectrodes (0.4 mm pitch), 1 or 1.5 mm deep (**Figure 2.1C**). This limits the recordings to superficial cortex in areas previously identified to be task relevant. Additionally, these devices are implanted beneath the dura, increasing the risk for infections of the central nervous system (Mollman and Haines, 1986; Korinek, 1997). A number of companies have begun to develop new chronic intracortical electrodes for human applications, including the neural threads being developed by Neuralink (Drew, 2023). There are a variety of semi-acute intracortical electrodes commonly used simultaneously for epilepsy monitoring and human neuroscience, such as the Behnke Fried electrode used for stereotactic EEG (Fried et al., 1997).

Stereotactic EEG (sEEG) is a type of intracortical electrophysiology commonly used to map epileptogenic zones for surgical resection (Chassoux et al., 2018). It uses one or more semi-acute intracortical electrode arrays with each of these electrode arrays containing macroelectrodes, microelectrodes, or both electrode types. These macroelectrodes usually have a lower impedance that is good at measuring lower-frequency signals originating from LFPs, similar to the signal measured by ECoG electrodes. The microelectrodes typically have high impedances that are well-suited for recording single-unit activity (Fried et al., 1999). These macro-micro sEEG electrodes have a few advantages and disadvantages compared to other intracranial electrophysiology and ECoG methods. Although sEEG electrodes have sparser coverage within a given brain volume due to the large spacing between macroelectrodes on a single shank, typically multiple electrodes are used simultaneously. This allows bilateral monitoring of multiple brain regions of clinical interest. These depth sEEG electrodes can also be used to access subcortical structures, such as thalamus, subthalamus, hippocampus, and basal ganglia (Herff et al., 2020). sEEG electrodes may also have lower surgical

and long-term complications than ECoG or Utah Arrays (Cardinale et al., 2013; Hader et al., 2013; Mullin et al., 2016) due to sEEG electrode implantation only requiring small burr holes whereas Utah Array and ECoG implantation require more extensive craniotomies.

Recently, Neuropixel probes, a type of high-density linear electrode array, have been used for acute intrasurgical human recordings (Chung et al., 2022; Paulk et al., 2022). Other high-density electrode arrays are being developed that may be better for future human neuroscience research. For example, stronger and longer primate Neuropixels that will reduce the likelihood of the electrode shank from breaking while also enabling the electrodes to reach regions deeper than 1 cm from the brain surface (Trautmann et al., 2023).

Intracortical electrodes have been used for a number of BMI applications in both monkeys (Wessberg et al., 2000; Musallam et al., 2004) and humans (Hochberg et al., 2006; Collinger et al., 2013; Aflalo et al., 2015). In humans, sEEG electrodes have been used for a number of neural decoding and BMI applications (Herff et al., 2020), including spatial navigation (Vass et al., 2016; Watrous et al., 2018), motor control (Vadera et al., 2013; Li et al., 2017), and speech (Akbari et al., 2019; Han et al., 2019), but the most impressive BMI results with intracortical electrodes continue to be obtained with Utah Arrays. Recently, these Utah Array BMIs have been used to decode individual finger movements at >85% accuracy (Guan et al., 2022a), decode handwriting at 90 characters/min (Willett et al., 2021) and decode intended speech at 62 words/min (Willett et al., 2023).

2.2.2 Magnetic

2.2.2.1 Functional magnetic resonance imaging (fMRI)

Functional magnetic resonance imaging (fMRI) measures brain activity by detecting changes associated with blood flow. There are multiple versions of fMRI but the most common is Blood-Oxygen-Level-Dependent (BOLD) fMRI. BOLD fMRI generates a homogeneous strong magnetic field (1.5+ T) and can measure the difference between oxygenated (diamagnetic) and deoxygenated (paramagnetic) hemoglobin (Ogawa et al., 1990). Since neurons and other brain cells need oxygen, this shift between oxygenated and deoxygenated blood is well correlated with neuronal activity (Logothetis et al., 2001; Goense and Logothetis, 2008; Op de Beeck et al., 2008). This phenomena is called neurovascular coupling (Attwell et al., 2010). fMRI can measure the entire brain but suffers from low spatiotemporal resolution and sensitivity (**Figure 2.1A, D**). Additionally, the subject is confined to a magnetic bore and needs to minimize all body movements, thus limiting the type of neuroscience questions that can be answered.

High and ultra-high field fMRI (7-14 Tesla) has been developed that allows higher spatial resolution and sensitivity (Goense et al., 2016), but have a number of limitations including cost. Additionally, many people report adverse side effects when they enter/exit the ultra-high magnetic fields, including nausea and dizziness (Hoff et al., 2019).

fMRI has been used for various BMI applications, but has been limited by its low sensitivity, lack of portability, high cost, and requirement for the participant to minimize head and body movements (Sorger and Goebel, 2020).

2.2.2.2 Magnetoencephalography (MEG)

Magnetoencephalography (MEG) is similar to EEG since the source of the signal is the same, coordinated activity in cortical neurons that causes ionic currents and local magnetic fields (LMFs) (Buzsáki et al., 2012; Malmivuo, 2012; Lopes da Silva, 2013). Although it used to be believed that MEG had much better spatial resolution than EEG, recent work has disabused that idea and suggests that MEG and EEG have similar ability to source localize (Malmivuo, 2012). EEG is marginally better at recording activity that results from deep brain sources (Malmivuo, 2012). MEG instrumentation is an order of magnitude more expensive than EEG instrumentation and additionally currently require a stationary head dewar, restricting what activities the experimental subject can do. Some researchers have developed successful MEG-based BMIs (Mellinger et al., 2007; Wittevrongel et al., 2021), buts the limitations described above make MEG a non-ideal recording modality for most BMI applications. Despite these limitations, Kernel, a neurotechnology company, has developed a portable MEG system based on optically-pumped magnetometry and has plans to use this technology for BMI applications (Pratt et al., 2021).

2.2.3 Optical

2.2.3.1 Calcium imaging

Calcium imaging is a microscopy technique that measures the flux of calcium (Ca^{2+}) via calcium indicators, fluorescent molecules that fluoresce upon binding of Ca^{2+}. Measuring the fluorescence from these calcium indicators allows The activity of individual neurons and glia can be measured across time by quantifying the amount of fluorescence emitted by these calcium indicators. These calcium indicators are typically genetically-encoded calcium indicators (GECIs), thus requiring viral injections or transgenic animals. Until recently, this property has limited its use in nonhuman primates (Heider et al., 2010; Sadakane et al., 2015; O'Shea et al., 2017) and prevented it from being a usable technology for human applications. Although calcium imaging can image individual neurons and

track them across days, it can only image a small part of the brain (**Figure 2.1D**), lacks sufficient temporal discriminability to track sequential activation of neurons (Knöpfel and Song, 2019), and is limited to measuring activity within 0.6-1.4 mm of the brain surface (Glickfeld et al., 2013; Kawakami et al., 2013; Masamizu et al., 2014).

Imaging of dendritic calcium signals in nonhuman primate motor cortex has been used to control an online motor BMI and could be used to decode between four target locations at ~40-60% accuracy (Trautmann et al., 2021). Although the requirement for viral transfection currently prevents this technique from having human applications, it can be used to address neuroscience questions relevant to BMIs that have been difficult to answer with electrode-based techniques, such as linking population dynamics in motor cortex to the anatomical circuit structure and neuron cell types (O'Shea et al., 2017; Trautmann et al., 2021).

2.2.3.2 Voltage imaging

Voltage imaging is a mixture between optical and electrical acquisition methods. Like calcium imaging, it uses microscopy and fluorescent molecules to measure from individual neurons within its field of view. Like electrical methods, it tracks voltage fluctuations. However, instead of using electrodes, this method uses genetically encoded voltage indicators (GEVIs) to measure voltage fluctuations. It has some advantages over calcium imaging, including temporal resolution and tracking hyperpolarizing and subthreshold depolarizing signals within neurons (Knöpfel and Song, 2019; Zhu et al., 2021). However, it possesses most of the same limitations of calcium imaging, including inability to only record from superficial cortex, inability to record from large regions of the brain, and need for viral transfection or transgenic animals. Additionally, the current generation of GEVIs still have substantially worse signal amplitudes and signal-to-noise ratios than GECIs (Zhu et al., 2021).

2.2.3.3 Functional near-infrared spectroscopy (fNIRS)

Functional near-infrared spectroscopy (fNIRS) is an optical technique that uses near-infrared spectroscopy to measure concentrations of deoxygenated and oxygenated hemoglobin (Anon, 2023b). Similar to fMRI, it measures a hemodynamic proxy for neural activity. Although fNIRS has lower spatial resolution than fMRI (**Figure 2.1D**), it is a portable technique and allows subjects to freely move about and interact with their environment (Sakai, 2022). As with other optical techniques, this method is limited by light's ability to penetrate into tissue and is restricted to imaging neurovascular activity within superficial cortex (1-2 cm). Despite these limitations, fNIRS has been

used to successfully control BMIs (Coyle et al., 2007; Sitaram et al., 2007; Naseer et al., 2014; Shin and Im, 2020). Kernel, a neurotechnology company, aims to commercialize fNIRS as a sensitive method to noninvasively measure brain activity, including for BMI applications (Ban et al., 2022; Drew, 2023).

2.2.4 Ultrasound

2.2.4.1 Transcranial Doppler (TCD)

Transcranial Doppler (TCD) uses an ultrasound transducer placed above "acoustic windows," i.e., thinner regions of the skull, to measure blood flow velocity in the basal arteries of the brain. There are four commonly used acoustic windows in adults (transtemporal, transorbital, suboccipital, and submandibular), each with their own advantages and disadvantages (Carrizosa, 2022). TCD is used predominately for clinical applications, including microemboli detection, cerebral vasospasm detection, and measuring amount of stenosis (Purkayastha and Sorond, 2013). Since it is a low-cost and non-invasive method, it has additionally been used for several neuroscience applications (Duschek and Schandry, 2003).

Researchers have built TCD-based BMIs (Myrden et al., 2011; Aleem and Chau, 2013; Faress and Chau, 2013; Lu et al., 2015; Khalaf et al., 2018), but their performance (1-2 bits/min) has been underwhelming compared to other non-invasive methods. TCD suffers additional limitations that restrict its future use as a BMI. First, it is currently limited to recording through acoustic windows, which restricts TCD to imaging large basal arteries and providing a measure of global, rather than local, cerebrovascular activity (Purkayastha and Sorond, 2013). Second, TCD requires a skill operator to position the transducer appropriately and 10-15% of patients do not have adequate acoustic windows, even with optimal transducer placement (Carrizosa, 2022). Additionally, TCD produces a lot of heat, limiting the length of time that it can be safely used continuously (British Medical Ultrasound Society, 2010).

2.2.4.2 Functional ultrasound imaging

Functional ultrasound imaging (fUSI) is an emerging technology to detect changes in cerebral blood volume (CBV) with high sensitivity and spatiotemporal precision. It was first used in 2011 to identify cortical and thalamic areas activated by whisker stimulation and to track the propagation of seizures in rats (Macé et al., 2011). Since then it has been used in a variety of other model organisms, including ferrets (Bimbard et al., 2018), mice (Tiran et al., 2017), rabbits (Demené et al., 2018), nonhuman

primates (Dizeux et al., 2019; Blaize et al., 2020), and humans (Demene et al., 2016; Imbault et al., 2017).

fUSI takes advantage of ultrafast plane-wave ultrasound and pulsed-wave Doppler to form Power Doppler images at 1-10 Hz. Briefly, plane wave ultrasound pulses are generated at a high frequency (pulse repetition frequency; PRF) and multiple angles (**Figure 2.2A**). The resulting plane wave ultrasound images are coherently combined to form a single compounded image (**Figure 2.2B**). A series of these compounded images is used in turn to generate each Power Doppler image **(Figure 2.2C**). An SVD-based clutter filter or high-pass filter is used to isolate the signal from the red blood cells and ignore the brain tissue motion (Demené et al., 2015). Parameters at each stage of this process can be optimized for different objectives. See (Montaldo et al., 2022) for a detailed, yet intuitive, explanation of pulsed-wave Doppler and functional ultrasound neuroimaging.

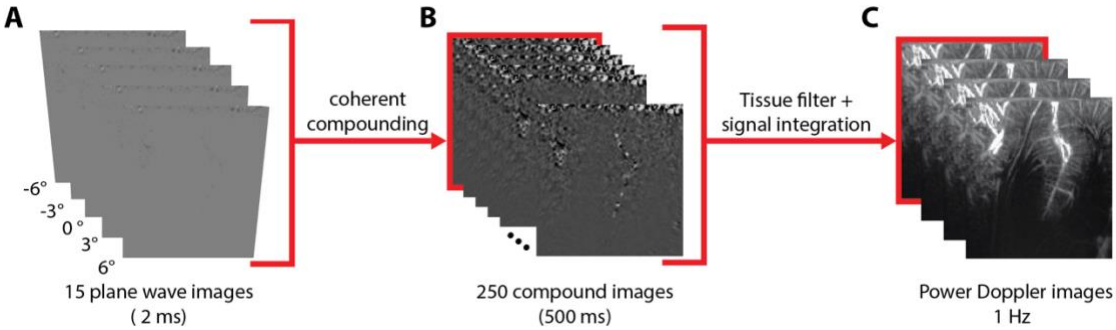

Figure 2.2 Functional ultrasound creates high-resolution, high-sensitivity Power Doppler images.
(A) Ultrafast plane wave ultrasound images are acquired at 5 angles with 3 accumulations in a total of 2 ms. (B) These plane-wave images are coherently compounded into a single image. These compounded images are generated at 500 Hz. (C) A series of compounded images are formed into a single Power Doppler image. The final images are 1 Hz instead of 2 Hz due to hardware and software limitations requiring ~500 ms of downtime to transfer and save the compounded images.

The parameters at each stage of this image acquisition can be tailored for different applications and trade-offs. The central frequency of the ultrasound transducer determines the spatial resolution limit. With a 15.6 MHz linear transducer, the voxel resolution is ~100 x ~100 μm for a 2D imaging plane with a variable slice thickness dependent upon the transducer lens (Montaldo et al., 2022). The Power Doppler framerate can be increased at the cost of sensitivity. Compounded images are acquired at 500 Hz, but different numbers of these compounded images can be used to form each Power Doppler image. For example, for 10 Hz Power Doppler images, 50 compounded images are used while for 2 Hz Power Doppler images, 250 compounded images are used. Using less compounded images leads to reduced sensitivity to CBV changes. An additional consideration is the speed of data transfer and

saving. For the ultrasound acquisition system used in majority of studies described in this dissertation, we acquired ~500 ms of compounded images, which took ~500 ms to save to our solid-state hard drive. Newer fUS systems have accelerated the data saving process to allow continuous acquisition and saving of compounded images or Power Doppler images.

As we discussed above, current BMI technologies have various limitations and an ideal BMI technology would be non-invasive, long-lasting, sensitive to rapid changes in small groups of neurons, and able to image from multiple large cortical and subcortical brain regions simultaneously. Functional ultrasound imaging (fUSI) is an emerging neuroimaging technology that is well-positioned to achieve many of these criteria.

In this dissertation, we used a 256-channel ultrafast ultrasound acquisition machine (Verasonics Vantage 256) and a 128-element linear ultrasound probe. Since fUS is currently unable to penetrate primate skulls, we performed fUSI through a craniectomy or sonolucent skull replacement. For the monkey studies, we used a 15.6 MHz ultrasound transducer and acquired fUS data at 1 or 2 Hz with high spatial resolution (~100 µm in-plane) and large field of view (12.8 X 16-20 mm; H X W). For the human studies, we used a 7.5 MHz ultrasound transducer and acquired fUS data at ~0.7 Hz with high spatial resolution (~200 µm in-plane) and large field of view (38.4 X 50 mm; H X W).

2.3 Posterior parietal cortex (PPC)

The posterior parietal cortex (PPC) is a good candidate region for BMI applications because it is a visuomotor area with many movement-related signals. This allows a BMI implanted in PPC to decode intended movements with high accuracy and speed (Andersen et al., 2019). It is anatomically situated between the visual cortex and motor cortex, fitting its role as a sensorimotor transformation area. PPC neurons encode a variety of different variables related to movements, including effector, direction, and action desirability.

2.3.1 Encoding of effector

Separate PPC regions preferentially encode different movement types (Cui and Andersen, 2007; Hadjidimitrakis et al., 2019), or "effectors". For example, lateral intraparietal area (LIP) preferentially encodes saccades (Gnadt and Andersen, 1988), parietal reach region (PRR) preferentially encodes limb reaches (Snyder et al., 1997), and anterior intraparietal area (AIP) preferentially encodes grasping movements (Taira et al., 1990) (**Figure 2.3**). These areas reveal an effector-dependent functional organization across PPC.

In this dissertation, we focus on saccadic eye movements to corroborate our fUSI results with the extensive electrophysiology and fMRI literature on saccadic decision-making within LIP. However, the methods developed here generalize to non-saccadic tasks and to regions outside of PPC.

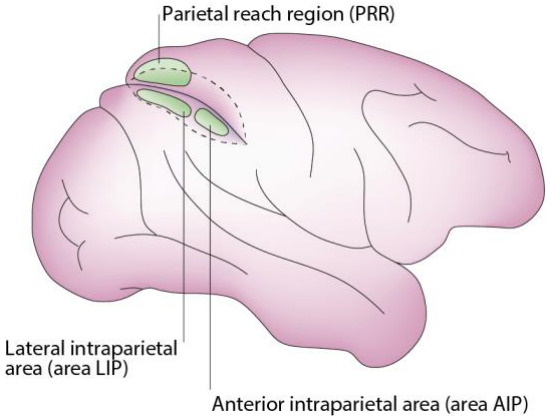

Figure 2.3 PPC is organized by different movement effectors.
LIP predominately encodes eye movements. PRR predominately encodes reaches. AIP predominately encodes grasps. Figure modified with permission from (Cohen and Andersen, 2002).

2.3.2 Encoding of direction

Many PPC neurons exhibit increased activity to visual stimuli within its visual receptive field and before movement onset to their response field (Andersen, 1988; Gnadt and Andersen, 1988; Colby et al., 1996). The width of the visual response field for each LIP neuron varies greatly (<3° to >30°) and is positively correlated with response field eccentricity (Ben Hamed et al., 2001). The visual response field and saccadic response field are highly overlapping, if not identical, (Gnadt and Andersen, 1988; Barash et al., 1991; Platt and Glimcher, 1997, 1998a; Shadlen and Newsome, 2001), so we will use the more general terminology "response field".

LIP's response fields are spatially organized, with adjacent neurons having similar response fields (Blatt et al., 1990; Ben Hamed et al., 2001; Patel et al., 2010, 2014; Savaki et al., 2010; Arcaro et al., 2011). However, the specific organization of these response fields remains debated (Patel et al., 2014). This debate about spatial organization of LIP neurons continues in part due to the limited field of view, sensitivity, and/or spatial resolution of existing recording techniques (**Figure 2.1**). fMRI can record whole brain activity but lacks the spatiotemporal resolution and signal sensitivity to refine our knowledge of PPC's spatial organization (**Figure 2.1A**). Electrophysiology can measure single neuron activity but cannot simultaneously record from entire large brain volumes such as primate PPC (**Figure 2.1C**). It can additionally be difficult to align and reconstruct electrophysiology data recorded over many months. This suggests the need for a sensitive technique that can bridge the gap in spatiotemporal resolution between single neurons (microscopic) and millimeter-sized patches of cortex (macroscopic), such as fUSI.

In this dissertation, we use fUSI to explore how saccade direction is represented at the mesoscopic level and we report results that help reconcile the differences between the previously reported microscopic and macroscopic functional organizations.

2.3.3 Encoding of non-motor signals

Variables relevant to future movements are encoded by neurons in multiple PPC regions. These include anticipated reward (Platt and Glimcher, 1999; Dorris and Glimcher, 2004; Musallam et al., 2004; Sugrue, 2004; Sugrue et al., 2005; Iyer et al., 2010; Ghazizadeh et al., 2018), categorization (Freedman and Assad, 2006), cue salience (Leathers and Olson, 2012), and task strategy (Zhang et al., 2017). However, much remains unknown about whether (and how) these variables are spatially organized within PPC regions or if they are more diffusely encoded. LIP and possibly other PPC regions integrates many of these decision variables to reflect the overall desirability of an action

(Dorris and Glimcher, 2004; Sugrue et al., 2005; Christopoulos et al., 2015). In this dissertation, we used fUSI to explore how many of these non-motor signals are encoded within PPC, including reward size, effort, and object novelty. fUSI has a large field of view capable of imaging an entire coronal plane of the intraparietal sulcus, allowing us to simultaneously measure multiple subregions of PPC, including LIP, VIP, and MIP. This will allow us to determine whether these non-motor signals are encoded within intermixed or discrete mesoscopic populations.

2.3.4 BMI applications

PPC has several advantages over primary motor (M1) cortex (PMv) for BMI applications. PPC encodes for higher-level aspects of movement intention, such as goal trajectory, while M1 encodes lower-level aspects, such as muscle activity or force (Townsend et al., 2006; Park et al., 2014; Gallivan et al., 2018). Additionally, PPC receives input from multiple sensory modalities, such as vision, proprioception, and audition, while M1 predominately receive inputs related to motor execution (Holsapple et al., 1991; Luppino and Rizzolatti, 2000). This would allow PPC to provide a greater diversity of control signals for a BMI. As discussed previously, BMIs implanted in PPC have been used for numerous human applications (Andersen et al., 2019), including control of individual finger movements (Guan et al., 2022a), speech generation (Wandelt et al., 2022a, 2022b), and control of robotic limbs (Aflalo et al., 2015). In this dissertation, we develop the first ultrasonic BMI by taking advantage of the higher-level visuomotor signals encoded within PPC.

2.4 Relevant previous fUSI results

2.4.1 Single-trial decoding of direction, task state, and effector

We previously showed that we could use fUSI to decode a variety of information from offline pre-recorded data, including target direction (left/right), task state (memory/not-memory), and effector (hand/eye). The following content is modified from this previous work for brevity and relevance (Norman et al., 2021).

To look for goal-related hemodynamic signals in the PPC, we acquired fUS images from NHPs using a miniaturized 15-MHz, linear array transducer placed on the dura via a cranial window. The transducer provided a spatial resolution of 100 μm × 100 μm in-plane, slice thicknesses of ~400 μm, covering a plane with a width of 12.8 mm and penetration depth of 16 mm. We positioned the probe surface-normal in a coronal orientation above the PPC (**Figure 2.4A, B**). We then selected planes of interest for each animal from the volumes available (**Figure 2.4C, F**). Specifically, we chose planes

that captured both the lateral and medial banks of the intraparietal sulcus (ips) within a single image and exhibited behaviorally tuned hemodynamic activity.

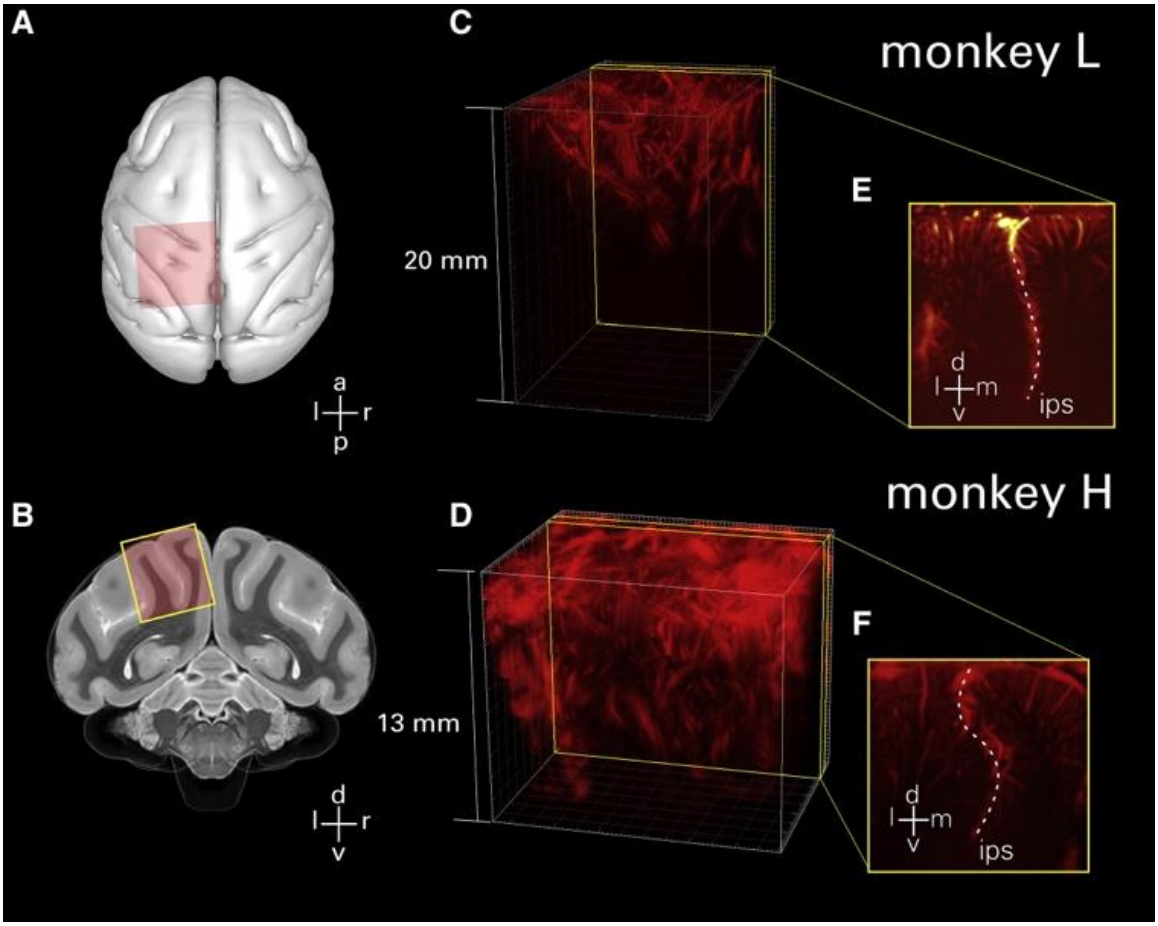

Figure 2.4 Anatomical imaging regions.
(A and B) Illustrations of craniotomy field of view in the axial plane (A) and coronal cross-section (B), overlaid on a NHP brain atlas (Calabrese et al., 2015). The 24 × 24-mm (inner dimension) chambers were placed surface normal to the brain on top of the craniotomized skull. (C and D) 3D vascular maps for monkey L and monkey H. The field of view included the central and intraparietal sulci for both monkeys. (E and F) Representative slices for monkey L and monkey H show the intraparietal sulcus (dotted line, labeled ips) with orientation markers (l, lateral or left; r, right; m, medial; v, ventral; d, dorsal; a, anterior; p, posterior).

We recorded 1 Hz fUSI data while two NHPs (Monkey L and H) performed memory-delayed instructed saccades and reaches. The monkeys were required to memorize the location of a cue presented in either the left or right hemifield and execute the eye or hand movement once the center fixation cue extinguished. For the reaches, the animal's gaze remained fixated throughout the trial, including during the fixation, memory, and reach movement phases.

2.4.1.1 Decoding two directions of eye or hand movements

We predicted the direction of upcoming movements using single trials of fUSI data (**Figure 2.5A**). Briefly, we used class-wise principal-component analysis (CPCA) to reduce data dimensionality. We chose CPCA because it is ideally suited to discrimination problems with high dimension and small sample size (Das and Nenadic, 2008, 2009). We then used ordinary least-squares regression (OLSR) to regress the transformed fUS data (from the memory delay period) to the movement direction (i.e., class label). Finally, we used linear discriminant analysis (LDA) to classify the resulting value for each trial as a presumed left or right movement plan. All reported results were generated using a 10-fold cross-validation. Saccade direction prediction accuracy within a session (i.e., decoded from the memory delay) ranged from 61.5% (binomial test versus chance level, $p = 0.012$) to 100% ($p < 0.001$) on a given 30-min run. The mean accuracy across all sessions and runs was 78.6% ($p < 0.001$). Reach direction prediction accuracy ranged from 73.0% (binomial test versus chance level, $p < 0.001$) to 100% ($p < 0.001$). The mean accuracy across all sessions and runs was 88.5% ($p < 0.001$).

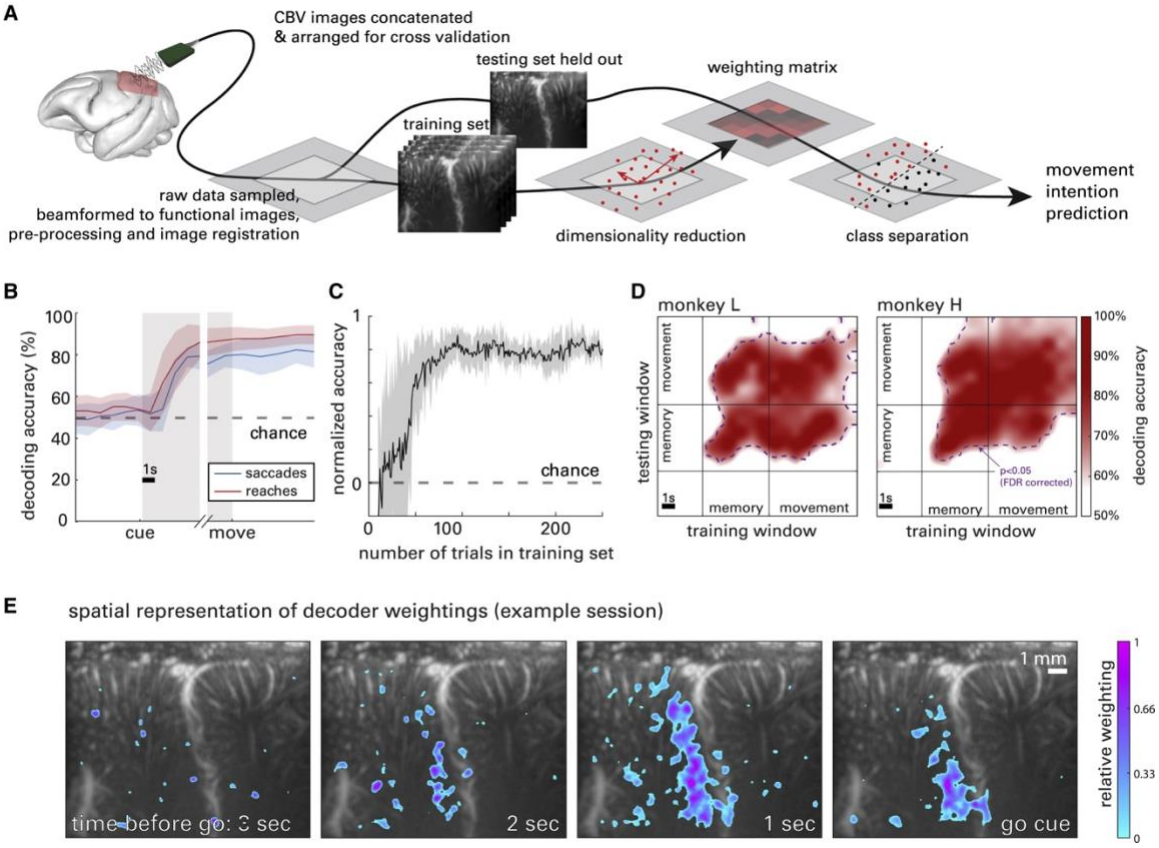

Figure 2.5 Single-trial decoding of intended movement direction.
(A) Data flow chart for cross-validated single-trial movement direction decoding. Training images were separated from testing data according to the cross-validation technique being used. Movement intention predictions were made for single trials based on the dimensionality reduction and a classification model built by the training data with corresponding class labels (i.e., actual movement direction). (B) Decoding accuracy as a function of time across all datasets. (C) Decoding accuracy as a function of the number of trials used to train the decoder. Data points in (B) and (C) are means, and shaded areas represent standard error (SEM) across sessions. (D) Cross-temporal decoder accuracy, using all combinations of training and testing data with a 1-s sliding window. Results are shown in an example session for each animal. Significance threshold is shown as a contour line ($p < 0.05$, FDR corrected). Training the classifiers during the memory or movement phase enabled successful decoding of the memory and movement phases. (E) Representative decoder weighting maps (monkey L). The top 10% most heavily weighted voxels are shown as a function of space and time before the go cue was given, overlaid on the vascular map.

To analyze the temporal evolution of direction-specific information in PPC, we attempted to decode the movement direction across time through the trial phases (fixation, memory, and movement). For each time point, we accumulated the preceding data. For example, at t = 2 s, we included imaging data from t = 0–2 s (where t = 0 s corresponds to the beginning of fixation). The resulting cross-validated accuracy curves (**Figure 2.5B**) show accuracy at chance level during the fixation phase, increasing discriminability during the memory phase, and sustained decode accuracy during the movement phase. During the memory phase, decoder accuracy improved, surpassing significance

2.08 s ± 0.82 s after the monkey received the target cue for saccades (2.32 s ± 0.82 s before moving, binomial test versus chance level, $p < 0.05$, Bonferroni corrected for 18 comparisons across time) and 1.92 s ± 1.4 s for reaches (2.28 s ± 1.4 s before moving). Decoding accuracy between saccades and reaches was not significantly different.

To determine the amount of data required to achieve maximum decode accuracy, we systematically removed trials from the training set (**Figure 2.5C**). Using just 27 trials, decoder accuracy reached significance for all datasets (binomial test, $p < 0.05$) and continued to increase. Decoder accuracy reached a maximum when given 75 trials of training data, on average.

Were we decoding the neural correlates of positions, trajectories, or goals? To answer this question, we used a cross-temporal decoding technique. We used a 1-s sliding window of data to train the decoder and then attempted to decode the intended direction from another 1-s sliding window. We repeated this process for all time points through the trial duration, resulting in an n × n array of accuracies, where n is the number of time windows tested. Cross-validated accuracy was significantly above chance level throughout the memory and movement phases (**Figure 2.5D**, purple line, binomial test versus chance level, $p < 0.05$, Bonferroni corrected for 18 time points). In other words, the information we are decoding from this brain region was highly similar during movement preparation and execution. This result suggests that this area is encoding movement plans (Snyder et al., 1997), visuo-spatial attention (Colby and Goldberg, 1999), or both. Although intention and attention are overlapping abstract concepts that cannot be separated by this experimental design, dissociating their contribution would not fundamentally change our interpretation. Distinct spatial locations within PPC encoded this information, a fact reflected in the variable weighting assigned to each voxel in our decoding algorithm. The decoder placed the highest weightings in area LIP (**Figure 2.5E**). This also agrees with the canonical function of this region for the planning of eye movements (Gnadt and Andersen, 1988; Andersen and Buneo, 2002).

2.4.1.2 Simultaneously decoding memory period, effector, and direction

To demonstrate the ability of fUS to decode multiple dimensions of behavior from a single trial of data, we trained the same two animals to perform a memory-delayed, intermingled effectors task. This task was similar to the saccade and reach tasks in its temporal structure. However, in addition to the animals fixating their gaze during the fixation period, they also moved a joystick to a central cue with their right hand. This cue's color indicated which effector they should move when the go cue

arrived (blue for saccades and red for reaches). If the monkey moved the correct effector (eye/hand) to the correct direction (left/right), then they received a liquid reward (**Figure 2.6A**).

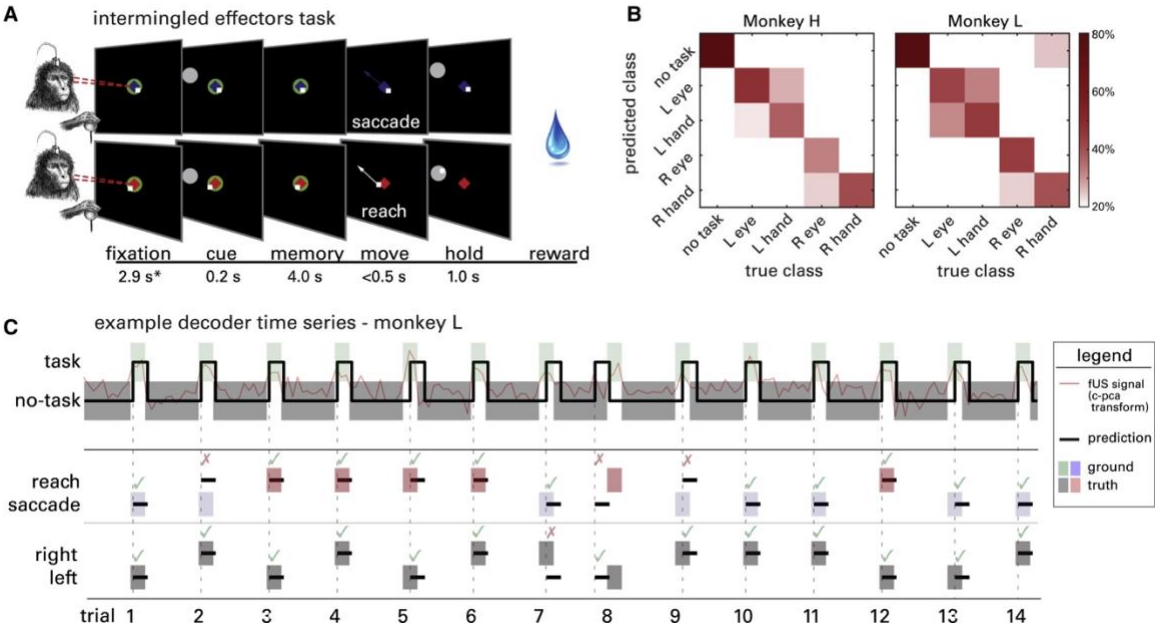

Figure 2.6 Decoding task, effector, and direction simultaneously.
(A) Intermingled memory-delayed saccade and reach task. A trial started with the animals fixating their gaze (and moving the joystick to) a central cue. The center fixation cue was either colored blue to cue saccades (top row) or red to cue reaches (bottom row), randomized trial by trial (i.e., not blocked). Next, a target (white circle) was flashed on either the left or right visual field. The animals had to remember its location while continuing to fixate their eye and hand on the center cue. When the center was extinguished (go signal), the animals performed a movement of either the eye or hand to the remembered peripheral target location. ∗Mean values across sessions shown; the fixation period was consistent within each session but varied across sessions from 2.4 to 4.3 s. (B) Confusion matrices of decoding accuracy represented as percentage (columns add to 100%). (C) Example classification of 14 consecutive trials. Classification predictions are shown as lines, and shaded areas indicate ground truth. An example of the fUS image time series transformed by the classifier subspace appears in red. After predicting the task period, the classifier decoded effector (second row) and movement direction (third row) using data only from the predicted task period (first row).

We decoded the temporal course of (1) the task structure, (2) the effector, and (3) the target direction of the animal using a decision tree decoder. First, we predicted the task memory periods versus non-memory periods (including movement, inter-trial interval, and fixation). We refer to this distinction as task/no task (**Figure 2.6C**, task/no task). To predict when the monkey entered the memory period, the decoder used continuous data where each power Doppler image was labeled as task or no task. After predicting the animal entered the task phase, the second layer of the decision tree used data from the predicted task phase period to classify effector and direction (**Figure 2.6C**, reach/saccade, left/right). Each of these decodes used the same strategy as before (cross-validated CPCA). **Figure 2.6B** depicts the confusion matrix of decoding accuracy for each class for monkeys H and L. The

classifier correctly predicted no-task periods 85.9% and 88.8% of the time for monkeys H and L, respectively, left versus right on 72.8% and 81.5% of trials for monkeys H and L, and eye versus hand on 65.3% and 62.1% of trials for monkeys H and L. All three decodes were significantly above chance level ($p < 0.05$, binomial test versus chance, Bonferroni corrected for three comparisons).

2.4.1.3 Vascular signal and information content

The purported benefits of fUS compared to established neuroimaging techniques include increased resolution and sensitivity. To test the benefit of increased resolution, we classified movement goals while systematically decreasing the resolution of the image. We resized the images using a low-pass filter in each of the dimensions of the imaging plane, x (across the probe surface) and z (with image depth). We then used the entire image (where the downsized images contained fewer pixels) to decode movement direction. Accuracy continuously decreased as voxel sizes increased (**Figure 2.7A**). This effect was isotropic (i.e., similar for both x and z directions).

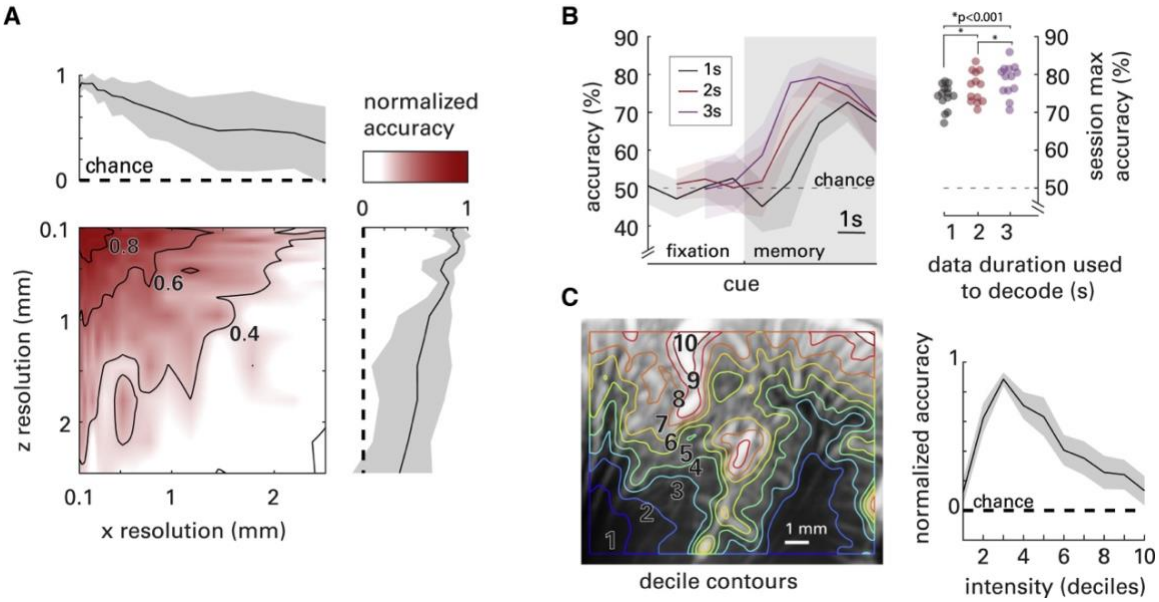

Figure 2.7 Effects of spatial resolution, time window, and mean power Doppler intensity.
(A) Accuracy decreases with resolution in both the x direction (across the imaging plane) and z direction (depth in the plane) in an isotropic manner. (B) Decoding accuracy as a function of decoder time bin durations (1-, 2-, and 3-s bins represented by black, red, and purple, respectively). Data are aligned to the end of the time bin used for decoding. Dots represent maximum decoder accuracy for each session for each of the bin sizes. Stars indicate statistical significance between groups (Student's t test, $p < 0.001$ for all combinations). (C) A typical vascular map overlaid with contours dividing the image into deciles of mean power Doppler intensity. Decoding accuracy is shown as a function of the mean power Doppler intensity. Information content is greatest in quantile 3, which mostly contains small vasculature within the cortex. Subcortical and primary unit vasculature (i.e., deciles 1 and 10) are least informative to decoding movement direction. All data represent means, and shaded areas, when present, represent standard error (SEM) across sessions.

We hypothesized that functional information useful for decoding would primarily be located in subresolution (<100 μm) vessels within the imaging plane. This hypothesis was based on the function of hyperemia, which starts in parenchymal arterioles and first-order capillaries (i.e., vessels of diameter <50 μm; (Rungta et al., 2018)). To test this hypothesis, we rank ordered voxels by their mean power Doppler intensity and segmented them by deciles, resulting in a spatial map of ranked deciles (**Figure 2.7C**). Deciles 1–2 mostly captured subcortical areas. Deciles 3–8 mostly captured cortical layers. Deciles 9 and 10 were largely restricted to large arteries, commonly on the cortical surface and in the sulci. We then classified movement goals using data from each decile. We normalized accuracy for each session, where 0 represents chance level (50%) and 1 represents the maximum accuracy reached across deciles. Accuracy peaked when the regions of the image within the third decile of mean Doppler power were used to decode movement direction. This decile was mostly represented by cortex vasculature, much of which is at or below the limits of fUS resolution. This result is consistent with our hypothesis that functional hyperemia arises from subresolution vessels (Boido et al., 2019; Maresca et al., 2020) and agrees with previous studies in rodents (Demené et al., 2016) and ferrets (Bimbard et al., 2018).

This work presented a high-water mark for ultrasound neuroimaging sensitivity that builds on the two previous studies of fUS in NHPs (Dizeux et al., 2019; Blaize et al., 2020). Significant advances include (1) classification of behavior using fUS data from a single trial, (2) detection of the neural correlates of behavior before its onset, (3) the first investigation of motor planning using fUS, and (4) significant advances in ultrafast ultrasound imaging for single trial and real-time imaging as a precursor to BMI. Our study is the first to successfully classify fUS activity with just a single trial of data. Furthermore, we predicted the differences between multiple task variables (e.g., effector, direction) in addition to detecting the task itself. We also decoded the behavior of the animal before it was executed.

2.4.1.4 Simultaneous effector and direction decoding

PPC's location within the dorsal stream suggests that while visuospatial variables are well represented, other movement variables such as effector may be more difficult to detect. Indeed, decoding accuracy was higher for direction (i.e., left versus right) than for effector (i.e., hand versus eye) (**Figure 2.5B**). The observed difference in performance is likely due to PPCs bias toward the contralateral side and partially intermixed populations for effectors in some regions. In addition to direction and effector, we decoded the task versus no-task phases. This is a critical step toward closed-

loop feedback environments such as BMI, where the user gates their own movement or the decoder is otherwise not privy to movement or task timing information. Furthermore, simultaneous decoding of task state, direction, and effector is a promising step forward for the use of fUS in both complex behaviors and BMIs.

2.4.1.5 Goal decoding for BMI

The results presented here suggest that fUS has potential as a recording technique for BMI. A potential limitation is the temporal latency of the hemodynamic response to neural activity. Electrophysiology-based BMIs that decode velocity of intended limb movements require as little latency as possible. However, in many cases, goal decoding circumvents the need for instantaneous updates. For example, if a BMI decodes the visuospatial location of a goal (as we do here), then the external effector (e.g., a robotic arm) can complete the movement without low-level, short-latency information (e.g., joint angles). Furthermore, goal information as found in PPC can represent sequences of consecutive movements (Baldauf et al., 2008) and multiple effectors simultaneously (Chang and Snyder, 2012). Finally, future goal decoders could potentially leverage information from regions in the ventral stream to decode object semantics directly (Bao et al., 2020). These unique advantages of goal decoding could thus improve BMI efficacy without requiring short-latency signals.

2.4.1.6 Comparison to other non-invasive and minimally-invasive recording methods

Other techniques, such as noninvasive scalp EEG, have been used to decode single trials and as a neural basis for control of BMI systems (Wolpaw et al., 1991; Wolpaw and McFarland, 2004; Norman et al., 2018). The earliest proof-of-concept EEG-based BMI achieved a one-bit decode (Nowlis and Kamiya, 1970). Performance of modern EEG BMIs varies greatly across users (Ahn and Jun, 2015) but can yield two degrees of freedom with 70–90% accuracy (Huang et al., 2009). This performance is comparable to that described here using fUS. However, fUS performance is rapidly increasing as an evolving neuroimaging technique, including recent breakthroughs in 3D fUS neuroimaging (Sauvage et al., 2018; Rabut et al., 2019). These technological advances are likely to herald improvements in fUS single-trial decoding and future BMIs.

Epidural ECoG is a minimally invasive technique used for neuroscientific investigation, clinical diagnostics, and as a recording method for BMIs. Building on the success of more-invasive subdural ECoG, early epidural ECoG in monkeys enabled decoding of continuous 3D hand trajectories with slightly worse accuracy than subdural ECoG (Shimoda et al., 2012). More recently, bilateral epidural

ECoG over human somatosensory cortex facilitated decoding of 8 degrees of freedom (4 degrees of freedom per arm, including 3D translation of a robotic arm and wrist flexion) with ~70% accuracy (Benabid et al., 2019). In this study, we demonstrated that unilateral fUS imaging of PPC enabled 3 degrees of freedom with similar accuracy. This is fewer degrees than attainable using modern bilateral ECoG grids. However, it demonstrates that, as a young technique, fUS holds excellent potential. Future work can, for example, extend these findings to similarly record bilateral cortical and subcortical structures, such as M1, PPC, and basal ganglia. As fUS recording technology rapidly advances toward high-speed, wide-coverage, and 3D scanning, these types of recordings will become commonplace.

2.4.1.7 Non-motor applications

fUS BMI in its form in the current study could also enable BMIs outside the motor system. Optimal applications might require access to deep brain structures or large fields of view on timescales compatible with hemodynamics. For example, cognitive BMIs such as state decoding of mood and other psychiatric states (Shanechi, 2019) are of great interest due to the astounding prevalence of psychiatric disorders. Like fUS, cognitive BMI is a small but rapidly advancing area of research (Musallam et al., 2004; Andersen et al., 2019). It is our mission that these areas of research mature together, as they are well matched in timescale and spatial coverage.

2.4.1.8 Relevance to current work

This previous work demonstrated that fUSI possessed the sensitivity to decode single-trial motor variables, including time of initiation (task/no-task), effector (hand/eye), and direction (left/right). However, this just scratches the surface of what should be possible with fUSI in PPC or other cortical areas. In this dissertation, we work to expand the dimensions (increased number of directions and task states) and number of features (reward size) decodable by fUSI. We additionally demonstrate how this technology can reveal novel information about mesoscopic neural populations. Finally, we describe the first efforts at translating this fUSI-BMI technology into human applications.

3 Topographic organization of direction within posterior parietal cortex

3.1 Background

The posterior parietal cortex (PPC) integrates visual information, represents possible action plans, and decides upon the optimal action for downstream execution (Colby and Duhamel, 1996; Snyder et al., 1997; Whitlock, 2017). Separate PPC regions preferentially encode different movement types (Cui and Andersen, 2007; Hadjidimitrakis et al., 2019), or "effectors". Lateral intraparietal area (LIP) preferentially encodes saccades (Gnadt and Andersen, 1988), parietal reach region (PRR) preferentially encodes limb reaches (Snyder et al., 1997), and anterior intraparietal area (AIP) preferentially encodes grasping movements (Taira et al., 1990). These areas reveal an effector-dependent functional organization across PPC.

It remains debated about whether PPC possesses functional organization along other dimensions, including response field location (Patel et al., 2014; Hadjidimitrakis et al., 2019). Several papers have found that LIP's response fields are spatially organized, with adjacent neurons having similar response fields (Blatt et al., 1990; Ben Hamed et al., 2001; Patel et al., 2010; Savaki et al., 2010; Arcaro et al., 2011), however, the specific organization of these response fields remains debated (Patel et al., 2014). This debate about spatial organization of LIP neurons continues in part due to the limited field of view, sensitivity, and/or spatial resolution of existing recording techniques (**Figure 2.1**). fMRI can record whole brain activity but lacks the spatiotemporal resolution and signal sensitivity to refine our knowledge of PPC's spatial organization (**Figure 2.1A**). Electrophysiology can measure single neuron activity but cannot simultaneously record from entire large brain volumes such as primate PPC (**Figure 2.1C**). It can additionally be difficult to align and reconstruct data recorded over many months. This suggests the need for a sensitive technique that can bridge the gap in spatiotemporal resolution between microscopic single neurons and macroscopic patches of cortex.

Here, we use an emerging technique, functional ultrasound imaging (fUSI), with a large field of view, excellent sensitivity, and high spatiotemporal resolution (**Figure 2.1B**, **D**) to determine the mesoscopic spatial organization of saccadic response fields within PPC. We found functionally distinct subregions within (dorsal-ventral) and across (anterior-posterior) coronal PPC planes where small mesoscopic patches of neighboring cortex encode different movement directions consistently

across many months to years. These results fill a gap in our understanding of PPC's functional organization and demonstrate that fUSI can help elucidate the function of other mesoscopic populations throughout the brain.

3.2 Results

We used a miniaturized 15.6-MHz, 128-channel, linear ultrasound transducer array paired with an ultrafast ultrasound acquisition system to record 1 Hz fUS images from two rhesus macaque monkeys (Monkey L and Monkey P; **Figure 3.1**). We positioned the transducer surface normal to the brain above the dura mater and recorded from multiple evenly spaced coronal planes of the left posterior parietal cortex (PPC). We centered the recording chamber over the intraparietal sulcus to record from as much of the posterior parietal cortex as possible, both medial-lateral, but also anterior-posterior (**Supplemental Movie 3.1**, **Supplemental Movie 3.2**). The 15.6-MHz transducer provided a high spatial resolution (100 μm x 100 μm in-plane) and a large field of view (12.8 mm width, 16 mm depth, 400 μm plane thickness).

We recorded 1 Hz fUSI data as Monkey L and P performed memory-guided saccades (**Figure 3.1B**). Each monkey was cued with one of eight directions, remembered the cue location, and executed a saccade to the remembered location once the central fixation point extinguished. This enabled us to measure high-resolution changes in cerebral blood volume (CBV) from multiple PPC subregions simultaneously as the monkeys performed multiple directions of saccades. These areas included lateral intraparietal area (LIP), ventral intraparietal area (VIP), medial intraparietal area (MIP), Area 5, Area 7, and medial parietal cortex (MP).

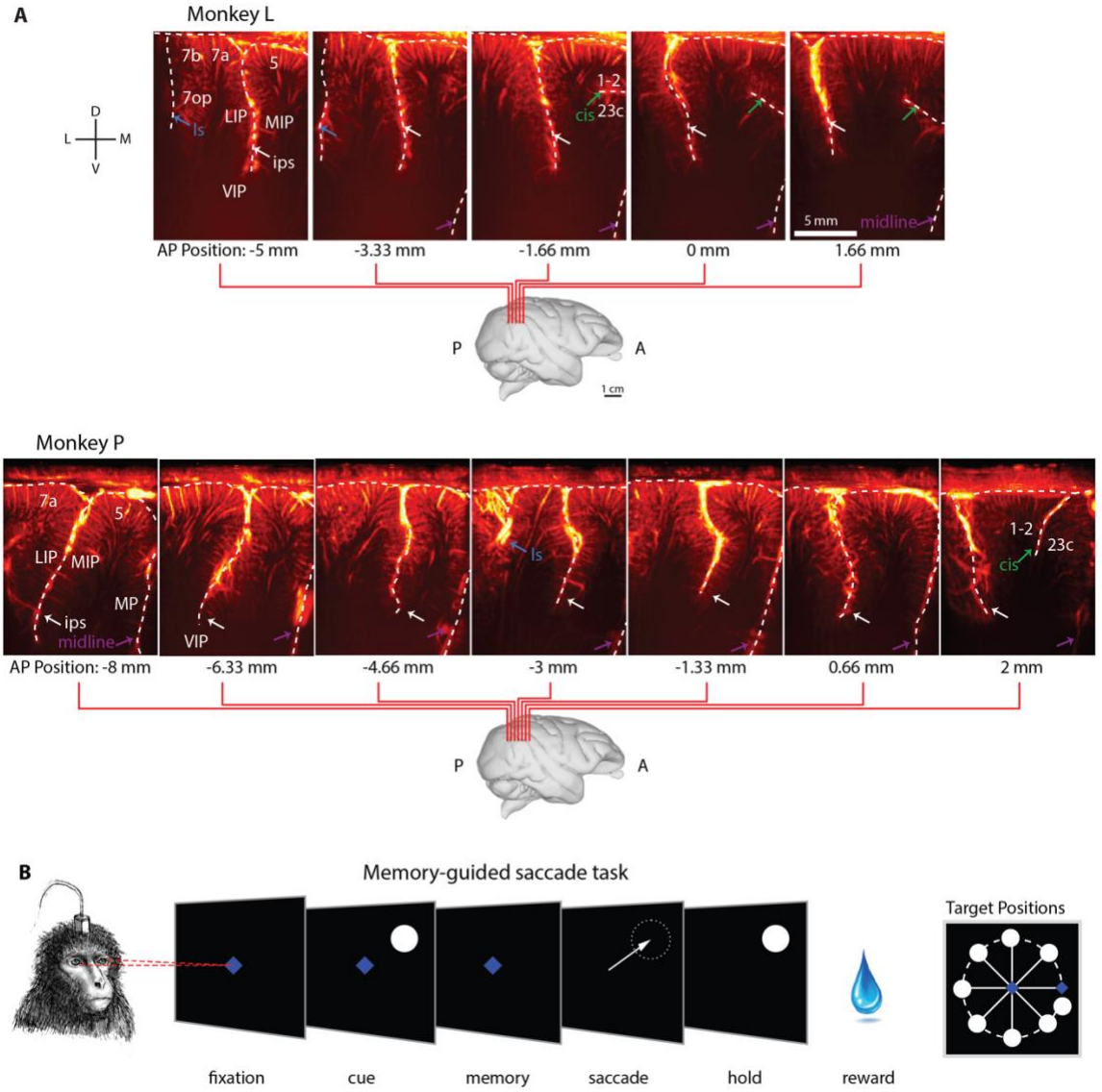

Figure 3.1 Monkeys perform memory-guided saccade task during fUSI acquisition.
(A) Coronal imaging planes in Monkey L and P. Position relative to estimated ear-bar zero (EBZ) overlaid on a NHP brain atlas (Calabrese et al., 2015). Anatomical labels based upon (Saleem, 2012). (B) Memory-guided saccade task. A trial began with the monkey fixating on a center blue diamond. After the monkey fixated, a white circular cue was flashed in one of 8 peripheral locations. Once the center fixation diamond extinguished, the monkey made a saccade to the remembered cue location and maintained fixation on the peripheral location. If the saccade was to the correct location, the peripheral cue reappeared and the monkey received a liquid reward.

3.2.1 Are there mesoscopic populations tuned to different directions?

To identify mesoscopic populations tuned to different directions, we convolved our task design with a single gamma hemodynamic response function and used a general linear model (GLM) to identify voxels that responded differently to the eight directions. In both monkeys, mesoscopic PPC

populations had clear directional tuning. In an example session from Monkey P (**Figure 3.2A-C**), the majority of LIP voxels showed directional tuning while very few voxels outside of the LIP showed directionally modulated activity. Some of these directionally-modulated voxels showed substantial increases in CBV (>20%) from baseline where the magnitude of the increase depended on the direction while other voxels displayed suppression from baseline for certain movement directions (**Figure 3.2B**). To quantify the example regions' tuning, we averaged the response to each of the directions at the end of the memory period across all the voxels in each ROI (**Figure 3.2C**). Different populations within a single coronal plane had different preferred directions and different widths of their tuning curves. Some ROIs were tightly tuned to a few specific directions (**Figure 3.2B**, **C** – ROI 2) while other ROIs had broader tuning to the entire contralateral hemifield (**Figure 3.2B, C** – ROI 1). The example session from Monkey L displayed similar phenomena (**Figure 3.2D-F**). Most voxels within the LIP displayed directional modulation and these voxels were clumped into multiple subpopulations with different tuning curves. These tuning curves had different preferred directions and tuning curve width. In Monkey L, the mid-MIP directly adjacent to the sulcus had some directionally tuned vascular response, but this activity did not penetrate into deeper cortical layers.

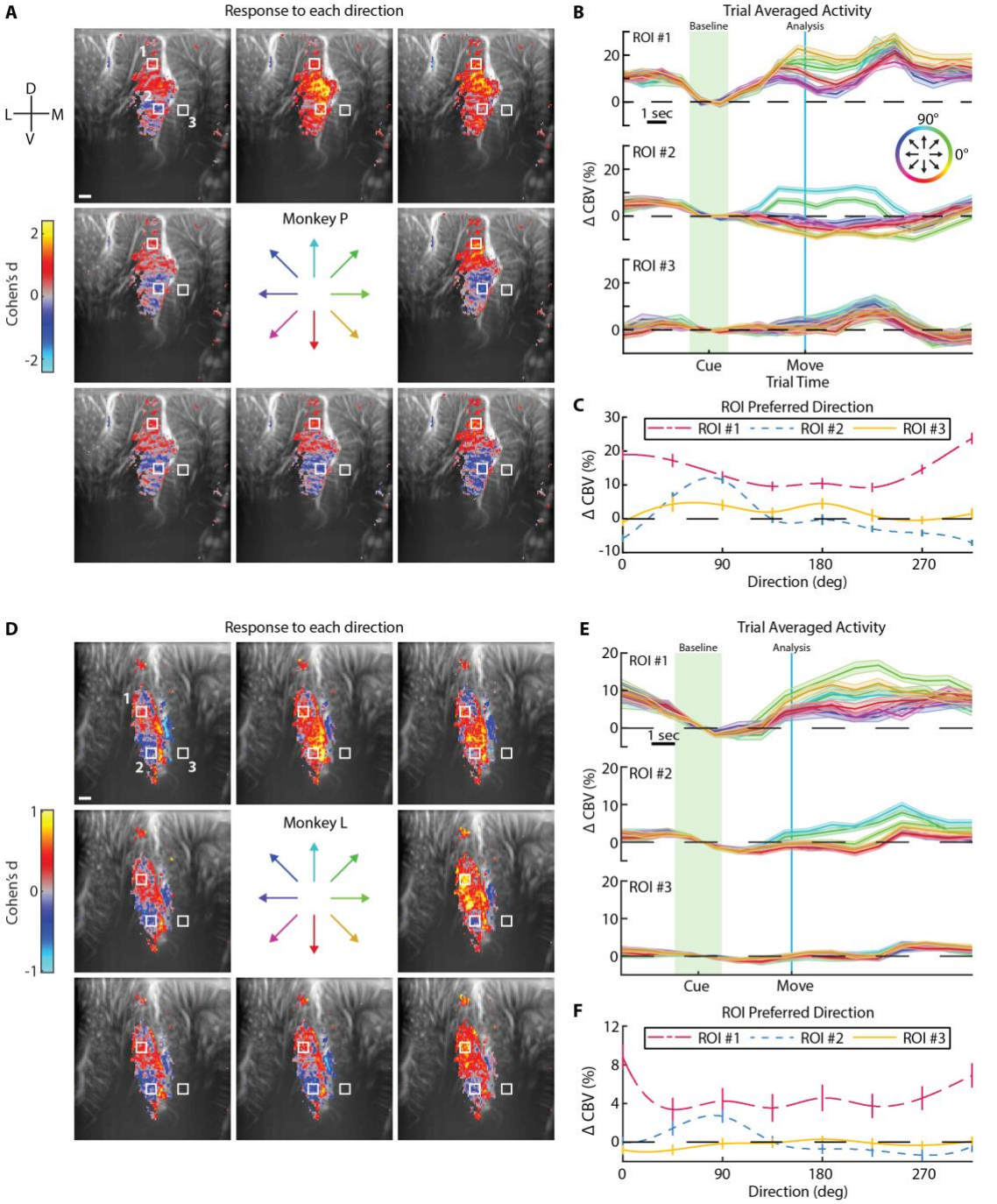

Figure 3.2 PPC contains multiple distinct directionally-tuned mesoscopic populations.
(A) Statistical parametric maps showing the average activity during the memory period. Voxel threshold determined by GLM F-test for voxels where q < 0.001 (FDR-corrected). White scale bar – 1 mm. Center arrows indicate the 8 directions tested. (B) Event-related average of activity within each ROI. Each line represents one direction. The circular color scale indicates the direction of each line. Error shading shows SEM. Green shading shows timepoints used for calculating baseline and blue line shows timepoint used for analyzing memory response to the different directions. (C) Tuning curves. Each line shows a cubic spline fit to the directional responses at the end of the memory period within each ROI. Error bars show SEM. (D-F) Example session for Monkey L. Same format as A-C.

3.2.2 How consistent is this directional tuning within a session?

Having observed clear mesoscopic populations with directional preference in both monkeys, we performed decoding analyses for each example session to better understand the information content within these voxel subpopulations and how consistent their responses were. We used principal component analysis (PCA) to reduce the dimensionality of the fUSI data and linear discriminant analysis (LDA) to predict one of the eight movement directions using the PCA-transformed data. We used a "multicoder" architecture where we predicted the horizontal (left, middle, or right) and vertical (up, middle, or down) components of intended movement separately and then combined those independent predictions to form a final prediction (e.g., up and to the right). We examined the ability to decode intended movement direction throughout the trial (**Figure 3.3**) and found that we could begin decoding the intended movement direction significantly above chance ($p<0.01$; 1-sided binomial test) within 3 seconds of the directional cue (**Figure 3.3A, D**). In both monkeys, the percent correct exceeded 50% (leave-one-out cross-validation; Monkey P – 59.6% correct, Monkey L – 54.1%). The missed predictions typically bordered the true movement direction (**Figure 3.3B, E**). To capture this information about the closeness of each prediction, we examined the mean absolute angular error (MAAE), i.e., the mean unsigned angular error between the predicted and true movement direction. As with the percent correct, the MAAE reached significance ($p<0.01$; 1-sided permutation test) within 3 seconds of the directional cue. The MAAE converged to <35° for both monkeys (Monkey P – 23.7°, Monkey L – 32.8°, **Figure 3.3A, D-bottom**).

The decoding analyses used the entire image at each timepoint to decode the intended movement direction on individual trials. To understand which portions of the vascular anatomy contributed the most to the decoding performance, we performed a searchlight analysis. We moved a pillbox (200 μm radius) across the entire image and assessed the ability of each pillbox to decode the intended movement direction (**Figure 3.3C, F**). For the searchlight analysis, we ignored voxels within and across the sulcal fold, i.e., we only used voxels on the same side of the sulcus for a given searchlight pillbox. We observed that LIP contained the most informative voxels and that these informative voxels overlapped with the same voxels identified with the previous GLM analysis. In both animals, a small number of voxels within the MIP were within the 10% most significant voxels (threshold: Monkey L – $p<0.005$, Monkey P – $p<10^{-5}$). These significant voxels were in the superficial cortical layers along the sulcus and did not extend into deeper cortical layers, matching the results from Monkey L's GLM analysis.

The searchlight analyses helped reveal which voxels were important for the overall decoding performance but did not answer which voxels are important for discriminating between specific direction pairs. To begin answering this question, we projected the LDA class-class boundaries back through the PCA transform to represent each LDA boundary in the vascular image space (**Figure 3.3G, H**). We observed several interesting patterns. First, different populations were important for maximally discriminating between different direction pairs. This might seem to disagree with the searchlight results where voxels within a 200 μm radius patch could robustly decode eight movement directions but we believe it means that discriminability between specific direction pairs improves if you have more of the image. In other words, the discriminability is improved by having more information rather than just a few voxels ($\leq$ 13 voxels) with similar directional preferences. Second, the importance of a given voxel for the boundary followed a gradient. For example, in **Figure 3.3G**, the importance of the voxels in the mid-LIP for ipsilateral upwards (Class 1) vs other directions (Class 2) displays a gradient where the boundary is stronger for neighboring directions. This agrees with there being different populations with strong tuning for specific directions. An ideal boundary should be comprised of the voxels with the strongest difference in response to a given direction to help reduce the trial-to-trial variability in the discriminability. Third, the conjunction of the boundary voxels matched with the GLM and searchlight analyses, further supporting that mesoscopic LIP subpopulations robustly encoded for different movement directions.

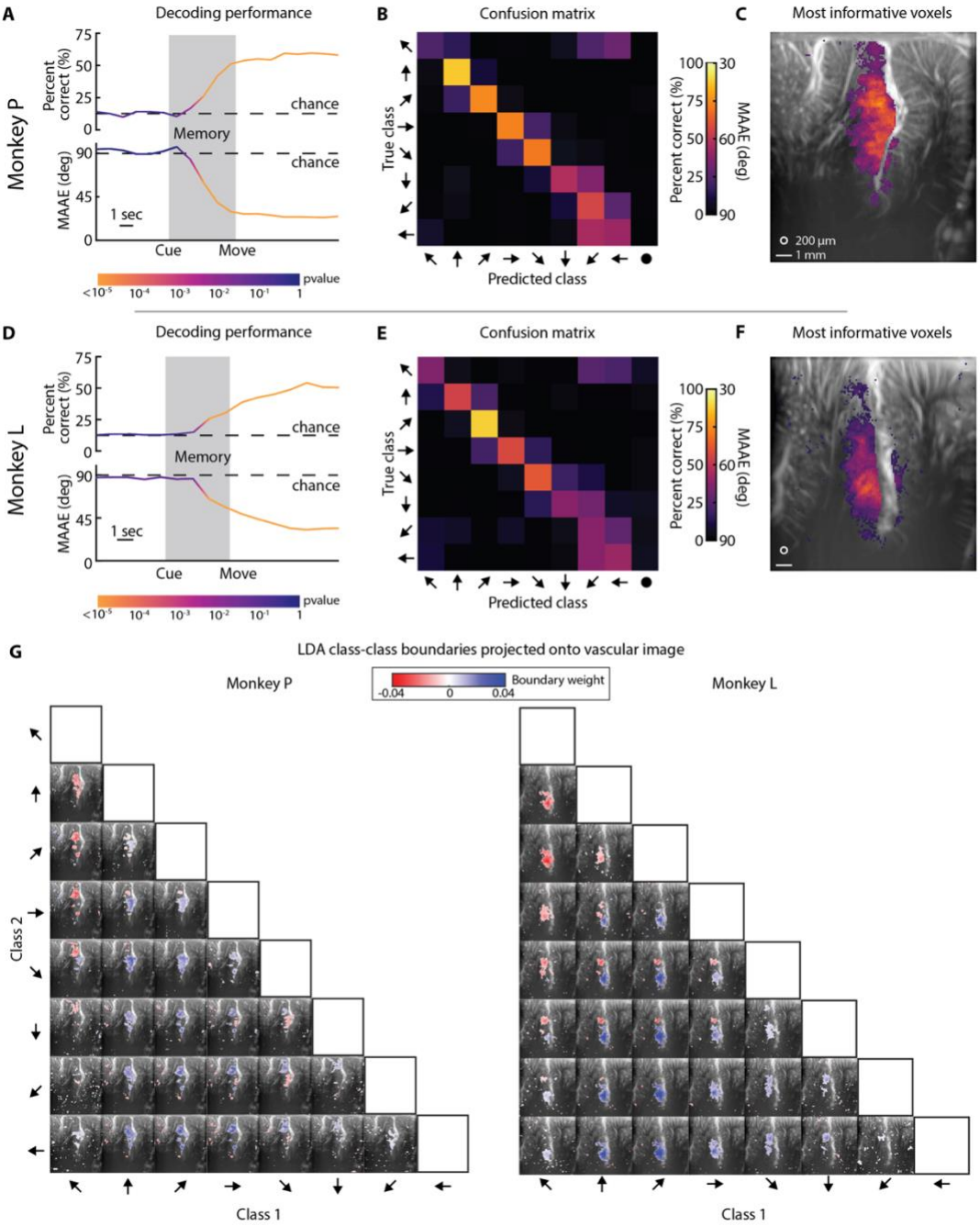

Figure 3.3 Single-trial decoding of eight intended movement directions with high accuracy.
(A) Decoding performance as a function of time. Top plot shows percent correct. Bottom plot shows mean absolute angular error (MAAE). Dashed lines show chance level performance. Color of the line shows statistical significance (1-sided binomial test or permutation test). (B) Confusion matrix of decoding represented as percentage (rows adds to 100%). (C) Searchlight analysis. Top 10% of voxels with the lowest MAAE. White circle – 200 µm searchlight radius. White line – 1 mm scalebar. Masked voxels correspond to threshold of $p<10^{-5}$. (D-F) Decoding performance for Monkey L. Same format as A-C. Masked voxels corresponds to threshold of $p<0.005$. (G) Projection of LDA boundaries onto vascular image for Monkey P. Each tile represents the boundary between two direction classes. (H) Projection of LDA boundaries onto vascular image for Monkey L.

3.2.3 Are these mesoscopic populations stable across multiple days?

In the example sessions, PPC subpopulations were robustly tuned to individual movement directions, but are these mesoscopic regions stable across time? To begin answering this question, we collected data from the same coronal plane across many months. We then trained our decoder on one day's data and tested how well we could use this trained decoder to predict movement direction on other sessions from that same plane without any retraining of the decoder. We repeated this analysis using each session as the training set and testing all the other sessions. If the subpopulations are constant across time, then we should be able to decode intended movement direction using a decoder trained on another session's data from the same coronal imaging plane. If the subpopulations change across time, then we would expect decoder performance to get worse and for the confusion matrices to become random.

In Monkey P, the decoder performance remained significant even after more than 100 days between the training and testing sessions (**Figure 3.4A**). All pairs of training and testing session for Monkey P showed significant decoding performance ($p<10^{-5}$; 36/36 pairs) (**Figure 3.4B**). In Monkey L, the decoder performance remained significant across more than 900 days (**Figure 3.4D**). Almost all pairs of training and testing session for Monkey L showed significant decoding performance ($p<0.01$; 117/121 pairs) (**Figure 3.4E**). Different training sessions had different decoding performance when tested on itself using cross-validation (diagonal of performance matrices), so we also examined the accuracy normalized to the training session's cross-validated accuracy. We did not observe any clear differences between the absolute and normalized accuracy measures. Interestingly, in Monkey L, the decoder trained on the March 13, 2021 session performed the best for three directions (contralateral up, contralateral down, and ipsilateral down) in the training set and continued to decode these same three directions the best consistently throughout the test sessions (**Figure 3.4D**). We saw this pattern consistently where the decoder could best predict certain directions, even when the training session had poor cross-validated performance by itself (**Supplemental Figure 3.1**).

In both monkeys, temporally adjacent sessions had better performance (**Figure 3.4C, F**). In Monkey L, the performance was clumped into two temporal groups (before and after May 3, 2023) where training on a session within its same temporal group provided the best performance. Physical changes in the imaging plane across time may explain the decrease in performance. Although we did our best to align our recordings to the exact same imaging plane from day to day, there was out-of-plane alignment issues where the major blood vessels were very similar but mesovasculature would change

(**Supplemental Figure 3.2A, D**). This suggested that we might be decoding from slightly different neural populations. This out-of-plane difference was <400 μm across all recording sessions based upon comparing the fUSI imaging planes with anatomical MRIs of our monkeys' brains. To test our hypothesis that differences in vascular anatomy led to the decrease in decoder performance, we looked at the similarity of the vascular anatomy across time using an image similarity metric, the complex-wavelet structural similarity index measure (CW-SSIM)(Sampat et al., 2009). The CW-SSIM clumped the vascular images into discrete groups (**Supplemental Figure 3.2B, E**), matching our qualitative assessment of image similarity. The similarity grouping also matched the pairwise decoding performance grouping in Monkey L (**Figure 3.4E**). The decoder performance and image similarity were correlated (**Supplemental Figure 3.2C, F**). As image similarity decreased between the training session and each test session, the decoder performance also decreased. This supports our hypothesis that the decrease in decoder performance resulted from changes in the imaging plane rather than drift in each subpopulation's tuning.

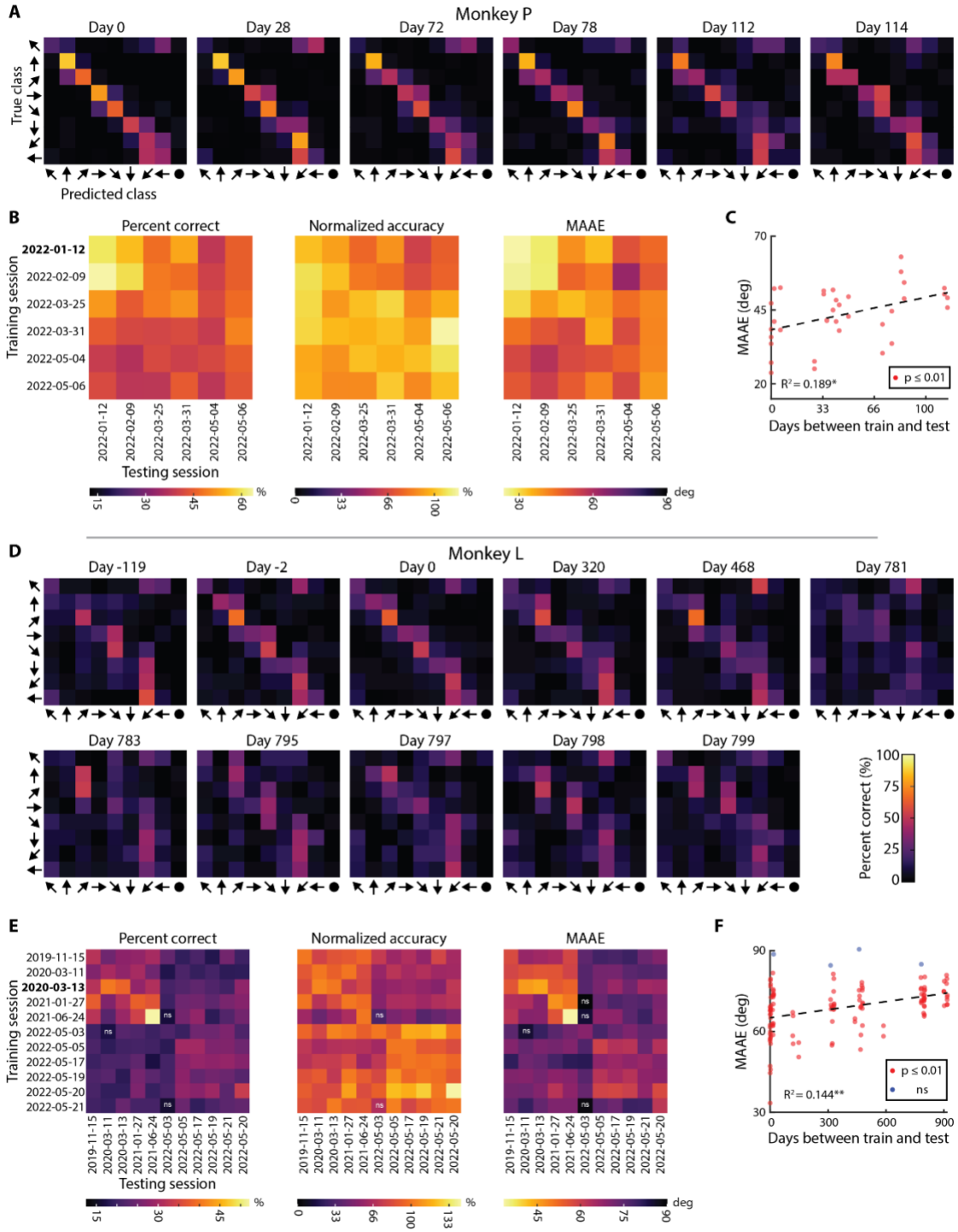

Figure 3.4 PPC stably encodes movement direction across many months to years.
(A) Example decoder stability for Monkey P. Trained the decoder on Day 0 data and tested the trained decoder on other sessions from the same imaging plane without any retraining. (B) Decoder stability for training and testing on each session. ns – nonsignificant decoding performance ($\alpha = 0.01$). Bold text represents example session shown in **Fig. 5A**. (C) MAAE as a function of days between the training and testing session (absolute difference in time). Dashed line – Linear fit to data. *=$p<10^{-2}$, **=$p<10^{-4}$. (D-F) Decoder stability for Monkey L. Same format as **Fig. 5A-C.**

3.2.4 How does mesoscopic population tuning change across anterior and posterior portions of PPC?

Having demonstrated that there are PPC subpopulations robustly tuned to individual movement directions and these subpopulations' tuning is consistent across many months to years, we next asked how this varied across different anterior to posterior coronal imaging planes. We repeated the same GLM analysis for data acquired from coronal planes evenly spaced throughout the PPC (**Figure 3.1A**, Supplemental Movie 3.1, **Supplemental Movie 3.2)** and found the peak preferred direction for every voxel (**Figure 3.5A**). Several patterns appeared. First, each coronal plane contained LIP voxels with directional modulation. Some of these planes contained large, contiguous patches of activity while other planes contained multiple discrete patches of activity. Second, most anatomical planes in both monkeys contained multiple LIP subpopulations with different tuning properties. These different subpopulations were sometimes in discrete patches and sometimes in the same contiguous patch. Third, posterior planes encoded more contralateral upward movements while anterior planes encoded more contralateral downward movements. Fourth, in Monkey P, regions outside of the LIP contained directionally modulated voxels, including in medial intraparietal (MIP), medial parietal (MP), and Area 5 cortex. We did not observe any activity within Area 5 of Monkey L and only observed very superficial activity within MIP of a single coronal plane (-3.33 mm of EBZ). Unfortunately, Monkey L's chamber was more medial and did not contain the same posterior portion of MP where we observed activity in Monkey P.

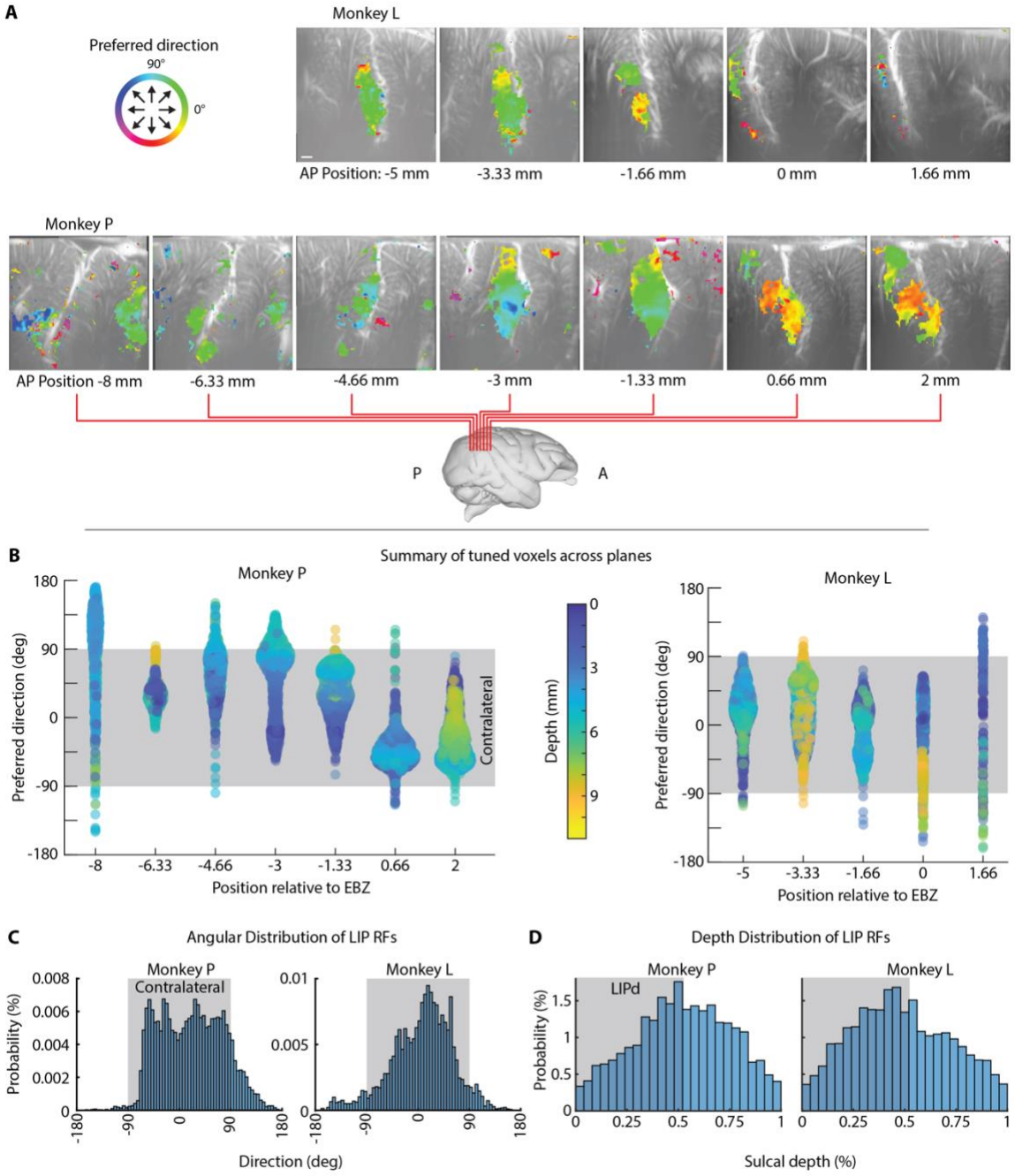

Figure 3.5 Polar direction is topographically organized along anterior-posterior axis of LIP.
A. Color overlays showing preferred direction for voxels with statistically significant difference in response for different movement directions. Threshold based upon GLM F-test where q < 0.01 (FDR-corrected). (B) Preferred direction for all significant voxels within each coronal plane. Color represents depth from brain surface. Grey shaded area shows contralateral angles. (C) Angular distribution of response fields within LIP. Gray shaded area shows contralateral angles. (D) Depth of tuned LIP voxels. Gray shaded area shows approximate LIPd.

To further understand the directional encoding across different coronal planes, we extracted the directional-modulated voxels and created a beeswarm chart of each voxel's directional preference (**Figure 3.5B**). As expected, certain directions within a given plane were over-represented, i.e., clumps of similarly tuned neurons in the beeswarm plot. The anterior-posterior gradient was still evident where more anterior planes had more voxels tuned for downwards directions while posterior planes had more voxels tuned for upwards directions. The majority of voxels encoded for contralateral movements (-90° to +90°) although there were some voxels that responded most strongly for ipsilateral movements. Each of the planes had broad and overlapping representation of contralateral movements. To better quantify these observations, we collapsed the voxels across planes (**Figure 3.5C**) and found that >85% of tuned LIP voxels were contralaterally preferring (Monkey P – 87.7%; Monkey L – 89.4%).

Dorsal (LIPd) and ventral (LIPv) LIP are believed to have different functions (Liu et al., 2010). According to theories of topographic encoding (Patel et al., 2014), we would expect separate representations of movement directions within LIPd and LIPv. In the statistical parametric maps, more anterior planes had more activity within LIPd than posterior planes, however the middle of the LIP seemed to have the most activity consistently across all planes. To help quantify this, we labeled the beeswarm chart with the depth of each voxel (**Figure 3.5B**). We did not observe any clear trends in the data to distinguish between LIPd and LIPv. We additionally collapsed all the tuned voxels across planes and looked at their percent depth within the sulcus (**Figure 3.5D**). LIPd is approximately the dorsal 53% of the lateral intraparietal sulcus (Liu et al., 2010). Instead of observing clear separation between LIPd and LIPv, we observed one homogenous group with the most activity peaking at the boundary between LIPd and LIPv, suggesting that LIPd and LIPv may share a topographic representation and/or that they receive common shared inputs.

Certain planes had better representation of specific directions, so we next asked whether there would be any performance difference in fUSI decoders trained on the different anatomical planes. We applied our decoding analysis to every recorded session (**Supplemental Figure 3.3A, B**). In Monkey P, all sessions reached statistical significance (18/18 sessions). In Monkey L, almost all sessions reached statistical significance (19/20 sessions). Decoder performance within a session depended on the monkey. In Monkey P, the peak MAAE ranged from 17° to 55° (29.97° ± 2.32° mean ± SEM). In Monkey L, the MAAE ranged from 33° to 85° (57.98° ± 3.35° mean ± SEM). This supports that on individual sessions we could accurately decode at least eight intended movement directions on a

single-trial basis and that there are individual populations that robustly encode for specific directions. There was no statistical difference (1-way ANOVA, α=0.01) between the percent correct or MAAE depending on the plane (**Supplemental Figure 3.3C**).

3.3 Discussion

This work demonstrates that posterior parietal cortex (PPC) contains voxels tuned to different directions. These tuned voxels were predominately within LIP and grouped into contiguous mesoscopic subpopulations. Multiple subpopulations existed within a given coronal plane, i.e., multiple preferred directions in a given plane. A rough topography exists where anterior LIP had more voxels tuned to contralateral downwards saccades and posterior LIP had more voxels tuned to contralateral upwards saccades. These populations remained stable across more than 100 – 900 days.

3.3.1 Sensitivity of fUSI

We observed large effect sizes with changes in cerebral blood volume (CBV) on the order of 10 – 30% change from baseline activity (**Figure 3.2**). This is much larger than observed with BOLD fMRI where on similar saccade-based event-related tasks, the effect size was approximately 0.4 – 2% (Kagan et al., 2010; Wilke et al., 2012). Our results agree with previous papers that found fUSI is a sensitive neuroimaging technique for detecting mesoscopic functional activity in a diversity of model organisms, including pigeons, rats, mice, nonhuman primates, ferrets, and infant and adult humans (Macé et al., 2011, 2018; Demene et al., 2016; Imbault et al., 2017; Bimbard et al., 2018; Demené et al., 2018; Rau et al., 2018; Dizeux et al., 2019).

3.3.2 Anterior-posterior gradient

Our results agree with previous studies of topography within LIP. Our fUSI data (**Figure 3.5**) matches two fMRI (Patel et al., 2010; Arcaro et al., 2011) and two electrophysiology (Ben Hamed et al., 2001; Wardak et al., 2004) studies that found an anterior-posterior gradient where anterior LIP encodes for more downwards movements and posterior LIP encoded for more upwards movements. Ben Hamed et al. 2001 stated "LIP does not appear to contain a continuous and orderly retinotopic organization. Across nearby and successive penetrations, neurons seemed to be organized in clusters of cells with similar visual and oculomotor properties, but sharp transitions from one cluster to another could be observed." This matches very closely with the results observed in this study where we found clusters within LIP tightly tuned to one direction with differently tuned clusters in close proximity within a given plane.

Two additional studies (Blatt et al., 1990; Savaki et al., 2010) found the opposite anterior-posterior gradient where anterior LIP encoded for upwards movements while posterior LIP encoded for downward movements. To reconcile these contradictory results, (Patel et al., 2014) suggested that there existed separate topographies for two of the main functions of LIP. One topography for

attentional processing (anterior LIP—downward attention; posterior LIP—upward attention) and one topography for saccade planning (anterior LIP—upward saccades; posterior LIP—downward saccades). Our results where we used a memory-guided saccade task disagree with this interpretation and instead suggest another explanation. Arcaro et al. 2011 reconciled their fMRI data with the two electrophysiology studies by suggesting that the differences result solely because of differences in recording site location within the lateral intraparietal sulcus, i.e., the two electrophysiology papers recorded from different overlapping anterior-posterior ranges of LIP. The combined range of recording agreed with the results that Arcaro et al. 2011 showed for visuotopic LIP (LIP_{vt}) and caudal intraparietal cortex (CIP-2). Our data supports this interpretation. The provided stereotactic zero, i.e., ear-bar zero (EBZ), in Blatt, Andersen, and Stoner 1990 agree with our results. Our results overlap with their results for approximately 4 mm (–4 to –8 mm of EBZ) and over that range, we observed the same tuning of LIPv for contralateral upward saccades.

However, this does not explain the difference between Savaki et al. 2010 and the other studies, including the present results. This may be caused by a unique task and methodology not used in any of the other studies. The researchers had each monkey perform hundreds of saccades back and forth in just one direction (horizontal, vertical, or oblique) before euthanizing the monkeys and looking at accumulation of tritiated deoxyglucose in post-mortem tissue. They assumed that ipsilateral movements would not cause increases in deoxyglucose concentrations, e.g., that rightward saccades would not lead to increased deoxyglucose within the right LIP. However, our results and other studies (Ben Hamed et al., 2001) show that this assumption is false. For example, we found that some mesoscopic areas within LIP had increased neurovascular activity for all directions with a stronger response to contralateral targets (**Figure 3.2**). We also saw that some LIP regions could have higher neurovascular activity for ipsilateral movements than its polar opposite (**Figure 3.5**, –3 and –8 of EBZ in Monkey P). This suggests that Savaki et al. 2010 could identify regions tuned to horizontal, vertical, and oblique directions, but not comment on the sign of that tuning. This means their study may be limited in its ability to identify areas encoding for specific angles, i.e., their results showing upward or downward preference for different anterior-posterior regions of LIP may be reversed for at least some of LIP.

Together, our results agree broadly with the previous results and help resolve some of the disagreements about the specific organization of LIP for different angles of movement.

3.3.3 Preference for contralateral space

Previous studies found that LIP responds strongest to contralateral stimuli and movements. At the single neuron level, approximately 80-90% of LIP neurons are tuned to contralateral directions (Blatt et al., 1990; Ben Hamed et al., 2001). Of note, (Platt and Glimcher, 1998b) reported no bias towards contralateral or ipsilateral in their recorded LIP neurons. At the macroscopic population level, the BOLD response in LIP is also almost exclusively contralateral preferring (Kagan et al., 2010; Patel et al., 2010; Arcaro et al., 2011). In the present study, we found our results quite closely agreed with LIP having strongly lateralized responses with ~88% of LIP voxels preferred contralateral directions. The reasons for the apparent discrepancy with (Platt and Glimcher, 1998b) remains unknown.

3.3.4 Differences between dorsal and ventral LIP

Previous studies found that peripheral targets were represented within the ventral LIP (LIPv) while foveal and parafoveal targets were represented within the dorsal LIP (LIPd) (Blatt et al., 1990; Ben Hamed et al., 2001; Patel et al., 2010; Arcaro et al., 2011). In our study, we only tested a single eccentricity (20°) and observed activity within both LIPd and LIPv. In both monkeys, we observed less LIPd activity in the more posterior planes (< -3.33 mm of EBZ). The overall distribution of tuned LIP voxels did not demonstrate a clear separation between LIPd and LIPv. We do not know why our results disagree with previous studies. Future fUSI studies with foveal, parafoveal, and peripheral targets will be needed to explore the mesoscopic representation of eccentricity within LIP and PPC.

3.3.5 Directional saccadic activity outside of LIP

In Monkey P, we additionally observed directionally modulated activity outside of the LIP in the posterior-ventral MIP, Area 7, and medial parietal area (MP). MP has been previously identified as a saccade-related area in single-unit electrophysiology and fUSI studies (Thier and Andersen, 1998; Norman et al., 2021). In Monkey L, our recording chamber was too lateral and we were unable to record signals from MP. Our results in Monkey P further support that MP may be an underexplored oculomotor planning region. The MP voxels preferred contralateral directions and did not display any clear organization of their response fields.

The posterior-medial MIP also contained directionally tuned activity. Some of this activity (-8 mm of EBZ) is in superficial cortical layers, perhaps reflecting inputs to MIP that relay directional information from upstream brain regions. We do not know why we see activity within the deeper layers of posterior-ventral MIP. Previous work found the functionally-defined parietal reach region

(PRR), overlapping with the anatomical area MIP, responds predominately to reach movements or eye-hand movements (Snyder et al., 1997, 2000; Cui and Andersen, 2007). Our task was a memory-guided saccade task with no reach component. Monkey P sat in an open chair with his hands and arms free while Monkey L sat in an enclosed chair with his hands and arms confined. Despite Monkey P being free to move his arms, we did not observe any arm movements related to the task itself. Future fUSI studies where we use a task with intermingled reaches and saccades will be useful in elucidating why we see activity within MIP of one monkey.

More anterior portions of putative Area 7a displayed directionally tuned activity to contralateral movement directions. This is consistent with previous literature that found Area 7a neurons have visual receptive fields and display saccade-related activity (Hyvarinen, 1981; Motter and Mountcastle, 1981; Andersen et al., 1985, 1987). We do not know why only a small region of Area 7A in Monkey P showed directional tuning or why Area 7a in Monkey L did not have directionally tuned activity. One possibility is that the neurons within individual voxels of Area 7a display high heterogeneity in their response fields such that no consistent tuning appears at the mesoscopic population level.

3.3.6 Stability across time

We demonstrated that we could decode intended movement direction using a decoder trained on data from a different session many months to years apart. This strongly suggests that the directional preference for the LIP subpopulations remained stable. The decoder performed best when the training and testing sessions were close in time. We have three possible interpretations for this. First, the representations of direction within subpopulations randomly drift across time. Under this interpretation, we would expect that the predicted movement direction would become increasingly random as more time elapses as the tuned voxels used for the model decorrelate. A second interpretation is that the subpopulations drift, but they drift at the same rate and in the same directions. This would lead to the tuned voxels staying correlated but encode for different directions. Under this interpretation, we would expect to see the decoder make increasingly more mistakes, but in a consistent manner. In other words, the decoder might develop an error bias where instead of predicting the correct class, it consistently predicts a different direction in its place. A third interpretation is that the vascular anatomy relative to our recording plane changed across time and that we are decoding from slightly different neural populations. Under this interpretation, the decoding errors should increase for neighboring directions because the tuned mesoscopic populations

observed in this study extend in both anterior-posterior directions and smoothly transition to encoding different directions rather than having sharp transitions where neighboring voxels encode for completely different directions. This smooth transition means that the populations used for decoding will still be quite similar to the original populations being measured.

Our data best supports this third interpretation. Rather than the error's becoming increasingly random as time progresses, the confusion matrices still had strong diagonal, i.e., correct predictions, but just much higher variance about that diagonal. If the subpopulations tuning had drifted at different rates and in different directions, then the voxel-direction correlation learned by the decoder would have vanished. The decoder would then have made random errors for all directions and the confusion matrix would be random. When we looked at the image similarity across time, we know that the imaging plane did change despite attempting to align our recordings to the same imaging plane from day to day (**Supplemental Figure 3.2**). Additionally, the decoder performance and image similarity were positively correlated. This supports that the subpopulations are stable across time with our decoder performance decreasing because of our imaging plane changing.

3.3.7 Applications to ultrasonic brain-machine interfaces

We previously showed that we could decode movement timing (memory/not-memory), direction (contralateral/ipsilateral), and effector (hand/eye) simultaneously on a single-trial basis with high accuracy (Norman et al., 2021). We recently also demonstrated that we could train monkeys to use a real-time fUSI BMI for up to eight directions of eye movements (Griggs et al., 2022). Here, we extended these papers' results in several aspects.

First, we demonstrated that we could achieve better decoding performance using offline recorded data (50-60% correct) than the accuracy reported for the online real-time fUSI-BMI data (~38% correct). Much work remains to quantify why this difference exists, but we believe one reason is motion-correction. In the present study, we used *post hoc* motion-correction to minimize movement of the imaging plane across a session. In the real-time fUSI-BMI study, we did not implement online motion-correction. Although the mesoscopic populations are tolerant to a small amount of motion due to similarly tuned voxels being clumped together, the information in adjacent voxels is sufficiently decorrelated that our machine learning algorithms need to keep track of the same voxel across time for peak performance. This similarly agrees with our interpretation for why the decoder performance decreases across time. One future method that may be well-suited to this problem is

convolutional neural networks that can utilize local structure in images to maintain high performance rather than our existing decoder algorithms that assume features do not move across time.

Second, we demonstrated that we could decode above chance level with a static decoder model even after several years. In the fUSI-BMI paper, we only had data out to 79 days, which is much less than the 900 days reported here. This suggests that future ultrasonic BMIs can constantly update an existing model rather than needing to be recalibrated daily. This is one current advantage of imaging-based BMIs over electrode-based BMIs. Electrode-based BMIs require calibration or retraining for each subsequent session due to their inability to record from the same neurons across multiple days, let alone multiple months (Downey et al., 2018). Imaging-based BMIs just require precise alignment of the current field of view (2D plane or 3D volume) to a previous session's field of view.

3.3.8 Future studies and questions

3.3.8.1 Record along intraparietal sulcus axis

In our study and most of the previous studies of LIP response fields, the topography changed along an anterior-posterior axis. It will be interesting in future studies to align the ultrasound transducer along the intraparietal sulcus so that our imaging plane acquires a large anterior-posterior slice of LIP. This was not possible in the current animals due to the size of the ultrasound transducer and positioning of the chamber relative to the intraparietal sulcus.

3.3.8.2 Eccentricity axis

Many studies have found a topography along an eccentricity axis with foveal and parafoveal targets being anterior of the peripheral targets representation (Blatt et al., 1990; Ben Hamed et al., 2001; Patel et al., 2010; Savaki et al., 2010; Arcaro et al., 2011). In the current study, we presented our stimuli at a single eccentricity. It will be interesting to compare the representation of foveal, parafoveal, and peripheral targets within the LIP to see whether we observe a similar patchy organization to angular direction for eccentricity.

3.3.8.3 Relation of changes in CBV to underlying cellular activity

Each voxel (~100 μm x ~100 μm x ~400 μm) contains approximately 65 neurons and 130 glia (Shapson-Coe et al., 2021), whereas each 1-1.5 mm^3 fMRI voxel contains approximately 16,000-24,000 neurons and 32,000-48,000 glia. This suggests that fUSI may be able to detect very local activity within neural circuits, including from within different cortical layers. However, fUSI measures changes in cerebral blood volume (CBV) and neurovascular coupling is complex (Hillman,

2014; O'Herron et al., 2016; Iadecola, 2017; Kaplan et al., 2020). Although every neuron within the brain is positioned within 15 μm of a blood vessel (Tsai et al., 2009), we do not understand the contributions of different cell types sufficiently well to disentangle their contribution to the CBV signal. Given the small number of cells in a fUSI voxel and the recent advent of primate-specific Neuropixel probes capable of recording high-density electrophysiological activity a few centimeters in the brain (Trautmann et al., 2023), future experiments combining these two methodologies will help us better understand the specific relationship between the hemodynamic and underlying cellular activity within these mesoscopic populations. Several people have already begun to characterize the relationships between fUSI signals and other measures of neuronal activity, such as electrical activity and calcium fluxes (Boido et al., 2019; Aydin et al., 2020; Bourgeais-Rambur et al., 2022; Nunez-Elizalde et al., 2022). These papers found that fUSI was well correlated with both calcium and electrophysiological activity with some evidence that inhibitory neurons contribute more to the fUSI signal than excitatory neurons.

3.3.8.4 Spatial autocorrelation of fUSI voxels

Despite there only being ~65 neurons in a fUSI voxel, neighboring voxels are supplied oxygen and nutrients by the same neurovasculature. This leads to spatial autocorrelation between neighboring voxels (**Supplemental Figure 3.4**) and confounds our ability to precisely identify the size and spatial separation of tuned populations. Motion of our imaging plane and spatial smoothing further worsens this spatial autocorrelation. There have been a variety of methods proposed for fMRI to handle the statistical consequences of spatial autocorrelation and calculate accurate statistical thresholds for cluster-wise inference (Worsley et al., 1996; Eklund et al., 2016; Gopinath et al., 2018b, 2018a). However, to the best of our knowledge, no methods have been devised to separate the various contributors to the spatial autocorrelation, including correlated neuronal activity. Future experiments will be needed to tease apart the contribution of correlated neurons versus other contributors to the size of neurovascular patches with similar tuning. Each voxel most likely contains neurons with a mixture of response fields with a bias towards specific response fields. Simultaneously recording fUSI signals and single neurons will be crucial for understanding the response properties within individual voxels and patches of similarly tuned voxels.

3.3.8.5 Directional tuning of cortical layers

Ultra-high field fMRI has enabled sub-millimeter voxel resolution and allowed researchers to study layer-specific activity (Dumoulin et al., 2018), especially with CBV-based fMRI (Huber et al., 2015).

Similar laminar analyses are possible with fUSI because it measures CBV and has higher spatiotemporal resolution and sensitivity than UHF fMRI. To date, only one fUSI study has begun to explore this possibility. Blaize et al. 2020 inferred cortical layer based upon cortical depth from the sulcus and found layer-specific ocular dominance within deep visual cortex. In the present study, we observed broad activity within LIP that did not appear to respect any laminar boundaries within the cortex. In both monkeys, we detected some directionally-specific activity within the shallower layers of MIP (**Figure 3.2D**, **Figure 3.3C**, **Figure 3.3F**, **Figure 3.5A**). This may reflect activity within superficial input layers. We could qualitatively estimate the boundary between white matter and grey matter based upon the amount of organized mesovasculature observed in our vascular maps. However, the thickness of PPC cortex varied within and across imaging planes, which prevented reliable estimates of cell layer based upon cortical depth. Future studies will be needed to better understand how to define cortical layers with fUSI, including studies to identify layer-specific properties detectable by ultrasound.

3.4 Conclusion

Here, we used functional ultrasound imaging to demonstrate that the posterior parietal cortex (PPC) contains mesoscopic populations of neurons tuned to different movement directions. This organization changed along an anterior-posterior gradient and remained stable across many months to years. It helped unify previous findings that had examined the topographic organization of LIP at the macroscopic (fMRI) and microscopic (electrophysiology) levels. In one monkey, we additionally found robust saccade-related activity within the medial parietal (MP) cortex, a parietal area that warrants further investigation. Using the methods established here for tracking the same populations across many months to years, it will be possible to quantify the topographic organization of different brain regions and study how each area's mesoscopic and macroscopic organizations change across time.

3.5 Materials and Methods

3.5.1 Experimental model and subject details

All training, recording, surgical, and animal care procedures were approved by the California Institute of Technology Institutional Animal Care and Use Committee and complied with the Public Health Service Policy on the Humane Care and Use of Laboratory Animals. We worked with two rhesus macaque monkeys (*Mucaca mulatta*; 14-years old, male, 14-17 kg). Monkey L participated in two previous fUSI experiments (Norman et al., 2021; Griggs et al., 2022). Monkey P participated in one previous fUSI experiment (Griggs et al., 2022).

3.5.2 General

3.5.2.1 Animal preparation and implant

We implanted a titanium headpost and custom square recording chamber on each monkey's skull under general anesthesia and sterile surgical conditions. We printed or machined each 24 x 24 mm (inner dimension) chamber using Onyx filament (Markforged) or PEEK. We placed the recording chamber over a craniectomy centered above the left intraparietal sulcus.

3.5.2.2 Behavioral setup and task

Each monkey sat head-fixed in custom-designed primate chairs facing an LCD screen ~30 cm away. We used a custom Python 2.7 software based upon PsychoPy (Peirce, 2007) to control the behavioral task and visual stimuli. We tracked their left eye position using an infrared eyetracker at 500 Hz (EyeLink 1000, Ottawa, Canada). Eye position was recorded simultaneously with stimulus information for offline analysis.

Monkeys performed a memory-guided saccade task (**Figure 3.1B**) where they fixated on a center dot (fixation state), maintained fixation while a peripheral cue was flashed for 400 ms in one of eight locations (20d eccentricity, equally spaced around circle), continued to maintain fixation on center dot (memory state), and finally made a saccade to the remembered cue location (movement state). If they correctly made a saccade to the cued location, then the peripheral cue was redisplayed and the monkey had to maintain fixation on the peripheral target until the liquid reward (30% juice; 0.35 mL monkey L and 0.75 mL monkey P) was delivered. To avoid the monkeys predicting state transitions, we used variable durations sampled from a uniform distribution for each task state. In Monkey L, the fixation and memory phase was 4 ± 0.25 seconds, the movement phase was 0.75 ± 0.15, and the

intertrial interval (ITI) was 5 ± 1. For Monkey P, the fixation and memory phase were 5 ± 1 seconds, the movement phase was 1 ± 0.5 seconds, and the ITI was 8 ± 2 seconds.

3.5.3 Functional ultrasound imaging

We used a programmable high-framerate ultrasound scanner (Vantage 256; Verasonics, Kirkland, WA) to drive the ultrasound transducer and collect pulse echo radiofrequency data. We used a custom plane-wave imaging sequence to acquire the 1 Hz Power Doppler images. We used a pulse repetition frequency of 7500 Hz with 5 evenly spaced tilted angles (-6° to 6°) with 3 accumulations to create one high-contrast compounded ultrasound image. We acquired the high-contrast compound images at 500 Hz and saved the images for offline construction of Power Doppler images. We constructed each Power Doppler image using 250 compound images acquired over 0.5 seconds. To separate the blood echoes from background tissue motion, we used a SVD clutter filter (Demené et al., 2015). For more details on the functional ultrasound imaging sequence and Power Doppler image formation, please see (Macé et al., 2013; Norman et al., 2021).

We used a 15.6 MHz ultrasound transducer (128-element miniaturized linear array probe, 100 μm pitch, Vermon, France). This transducer and imaging sequenced provided us with a 12.8 mm (width) and 13-20 mm (height) field of view. The in-plane resolution was approximately 100 μm x 100 μm with a plane thickness of ~400 μm. During each recording session, we placed the ultrasound transducer on the dura with sterile ultrasound gel. We held the transducer using a 3D-printed slotted chamber plug that minimized motion of the transducer relative to the brain. The slots were spaced 1.66 mm apart. This slotted chamber plug allowed us to acquire specific imaging planes across sessions. To help with later offline data concatenation, we acquired vascular maps using a single Power Doppler image and adjusted the transducer until the acquired vascular map closely matched a previously acquired vascular image for that chamber slot.

3.5.4 Across session alignment and concatenation

We concatenated data across multiple sessions for each imaging plane. We first performed a semi-automated intensity-based rigid-body registration to align the vascular anatomy between sessions. As described above, during the acquisition, we minimized out-of-plane movement between sessions by matching each session's imaging plane to a previously acquired template image for each chamber slot. See (Griggs et al., 2022) for more details.

3.5.5 – 3D visualization

We used MATLAB to export the vascular images to NIFTI format. We used Napari (Sofroniew et al., 2022), the `napari-medical-image-formats` plugin (Boucsein, 2022), and custom Python code to visualize the 3D reconstruction and save as a movie.

3.5.6 Quantification and statistical analysis

Unless reported otherwise, summary statistics reported as XX ± XX are mean ± SEM.

3.5.6.1 General linear model (GLM)

We applied several pre-processing steps before creating the GLM to explain the data. We first applied a Gaussian spatial filter (FWHM – 100 μm). We then applied a pixelwise high-pass temporal filter (1/128 Hz) to remove low-frequency drift. We finally used grand mean scaling to scale each voxel's intensity to a common scale (Penny et al., 2006; Ashby, 2019). To build the general linear model, we convolved the regressors of interest with a hemodynamic response function (HRF). We used a single gamma function with a time constant (τ) of 1 second, a pure delay (δ) of 1 second, and a phase delay (n) of 3 seconds based upon a previous monkey event-related fMRI study (Kagan et al., 2010). The regressors of interest were fixation period, memory period, movement period, and reward delivery. For the memory and movement periods, we used separate regressors for each direction. We then fit the GLM model using the convolved regressors and scaled fUSI data. We used an F-test to identify voxels that had a statistically significant difference to the eight directions during the memory period.

3.5.6.2 Multiple comparison correction

For all voxel-wise p-values used and reported, we used false-discovery rate correction (FDR) to correct for the simultaneous multiple comparisons. This was implemented using MATLAB's `mafdr` function.

3.5.6.3 Preferred direction

We used a center-of-mass approach to find the preferred tuning of each voxel. For each voxel, we first calculated the Cohen's d measure of effect size by comparing the response at the end of the memory period to the baseline (-1 to 1 seconds relative to cue onset). This gave us a standardized measure of response strength for each direction. We then scaled the peak response at each voxel to be 1. We then found the centroid for each voxel, which provided both a direction and magnitude. The direction represents the peak tuning direction while the magnitude represents the strength of that tuning. A value close to zero means no tuning while a value close to 1 means highly tuned to a specific

direction. This method minimizes assumptions about shape of the response field, such as whether it is Gaussian. We then smoothed the resulting statistical map using a pillbox spatial filter (1-voxel radius).

3.5.6.4 Within-session decoding analysis

Decoding intended movement direction on a single trial basis had five steps: 1) aligning the fUSI data and behavioral data, 2) preprocessing, 3) selecting data to analyze, 4) dimensionality reduction and class separation, and 5) cross-validation. First, we created the behavioral labels by temporally aligning the fUS data with the behavioral data. We could then label each fUSI timepoint with its corresponding task state and movement direction.

Second, we preprocessed the data by applying several operations. The first operation was motion correction. We used NoRMCorre to perform rigid registration between all the Power Doppler images in a session (Pnevmatikakis and Giovannucci, 2017). We then applied temporal detrending (50 timepoints) and a pillbox spatial filter (2-voxel radius) to each Power Doppler image.

Third, we would then select what spatial and temporal portions of the data to use in the decoder model. We always used the entire image where each pixel is a single feature. We used a dynamic time window. At each timepoint before the cue, we used all timepoints since the start of the trial. For example, to test our ability to decode at 3 seconds after the trial start, we used the fUS images at 0, 1, 2, and 3 seconds. At each timepoint after the cue, we used all previous timepoints after the cue in the trial. For example, to test our ability to decode at 2 seconds after cue onset, we concatenated the data from 0, 1, and 2 seconds after the cue. We treated these timepoints as additional features in the decoder model. In other words, the input to our decoder model had N*T features, where N is the number of pixels in a single Power Doppler image and T is the number of timepoints.

Fourth, we split the data into train and test folds according to a leave-one-out or 10-fold cross-validation scheme. For the test sets, we stripped the behavioral labels. We then scaled the train and test splits by applying a z-score operation fit to the train data. We used the entire image as our features, i.e., each voxel's activity was a single feature. To train the linear decoder on the training data, we used principal component analysis (PCA) for dimensionality reduction and linear discriminant analysis (LDA) for class separation. For the PCA, we kept 95% of the variance. For the LDA, we used MATLAB's `fitcdiscr` function with default parameters. We used a multicoder approach where the horizontal (left, center, or right) and vertical components (down, center, or up) were separately

predicted and combined to form the final prediction. As a result of this separate decoding of horizontal and vertical movement components, "center" predictions are possible (horizontal—center and vertical—center) despite this not being one of the eight possible peripheral target locations. We then calculated the percent correct and absolute angular error for each sample in the test data.

Fifth, we then repeated the model training and testing for each consecutive fold of data. We finally found the mean accuracy metrics across all the folds, i.e., mean accuracy and mean absolute angular error (MAAE). To correct for testing the performance at every trial timepoint, we used a Bonferroni correction.

We used a 1-sided binomial test to calculate the p-values associated with the percent correct results and used a permutation test with 100,000 replicates to calculate the p-values associated with the angular error results. For the permutation test, a single replicate was created by sequentially drawing X directional guesses from a uniform distribution of the eight possible directions, where X is the number of trials in the session. We then calculated the 1-sided p-value of each of our results by finding how many of the replicates were less than our observed mean angular error.

See (Norman et al., 2021; Griggs et al., 2022) for more details on these methods.

3.5.6.5 Across-session decoding analysis

To test whether we could use a decoder trained on a separate session's data to decode movement intent in a different session, we applied the same steps as for the within-session decoding analysis with two differences. First, the training set was all the data from a specific session and the testing set was all the data from a different specific session. Second, to assess performance within the same train and test session, we used 10-fold cross-validation instead of leave-one-out cross-validation. The later sessions' data (after March 25, 2022) are used in a previous publication and were acquired at a 2 Hz imaging rate with slightly different acquisition parameters. See (Griggs et al., 2022) for more details about the acquisition of these data. For the across-session decoding analysis, we downsampled this 2 Hz data to 1 Hz to allow us to easily compare the same trial timepoints between the two sets of data.

3.5.6.6 Image similarity

We compared the pairwise similarity of vascular images from different sessions by using the complex wavelet structural similarity index measure (CW-SSIM). The CW-SSIM quantifies the similarity of two images, where 0 is dissimilar and 1 is the same image (Sampat et al., 2009). We used the CW-SSIM over other forms of SSIM because it is more flexible in incorporating variations in image

resolution, luminance change, contrast change, rotations, and translations. We used an implementation freely available from the MATLAB Central File Exchange (Wang et al., 2023) with 4 levels and 16 orientations.

3.5.6.7 PCA-LDA projection

To visualize the boundaries between pairwise classes, we projected the LDA boundaries through the PCA space. For each class-class pair, we obtained the LDA boundary weights (constant and linear components) which has a single weight for each principal component. We discarded the constant components and weighted each principal component by the linear component of the LDA weights and added all the principal components together. We then applied a threshold to each image where we kept the 10% most extreme values (positive or negative).

3.5.6.8 Searchlight analysis

We defined a circular region of interest (ROI) and, using only the pixels within the ROI, we performed the within-session decoding analysis using 10-fold cross-validation. We assigned that ROI's percent correct and MAAE metrics to the center voxel. We then repeated this across the entire image, such that each image pixel is the center of one ROI. To visualize the results, we overlaid the performance metric (MAAE or percent correct) onto a vascular map and kept up to the 10% most significant voxels. As part of this searchlight analysis, we ignored activity within the sulcal fold or activity on the other side of the sulcal fold. To do this, we defined the boundaries of the sulcal folds using a custom GUI in MATLAB and only used voxels on the same side of the sulcal fold as the searchlight center. This is similar in principle to the cortical surface-based searchlight decoding developed for fMRI (Chen et al., 2011).

3.5.6.9 Spatial autocorrelation

For every pixel in the image, we examined voxels at different distances from the seed voxel. For each distance tested, we identified voxels that were between [max(0, i-0.1) mm, i mm] away. We then performed Pearson linear correlation between these identified voxels and the seed voxel. We then assigned the mean correlation to the seed voxel.

To calculate the mean correlation for each distance, we took the mean and standard deviation across the entire image.

3.6 Extended Data

3.6.1 Supplemental figures

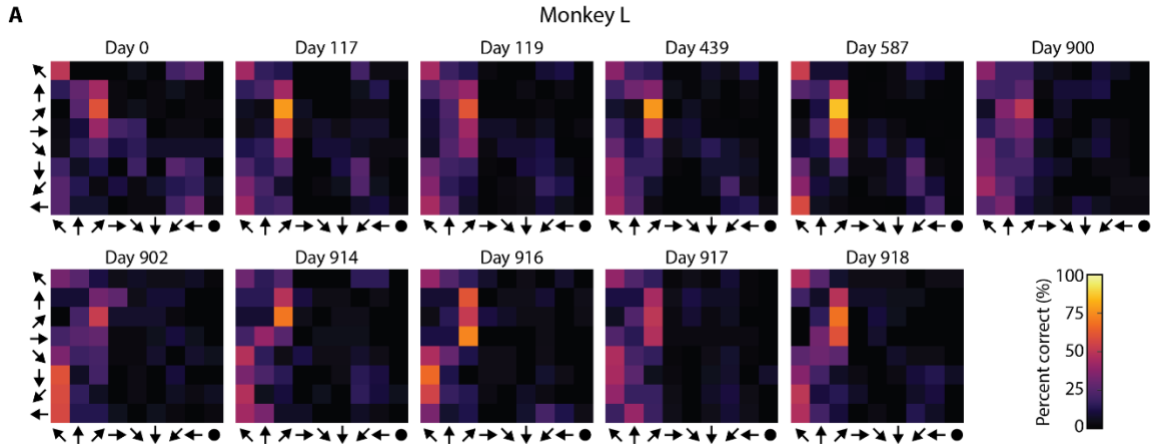

Supplemental Figure 3.1 Stability of directional preference across time.
Same format as **Figure 3.4C** but using different training session. (A) Example decoder stability for Monkey L. Trained the decoder on Day 0 data and tested the trained decoder on other sessions from the same imaging plane without any retraining.

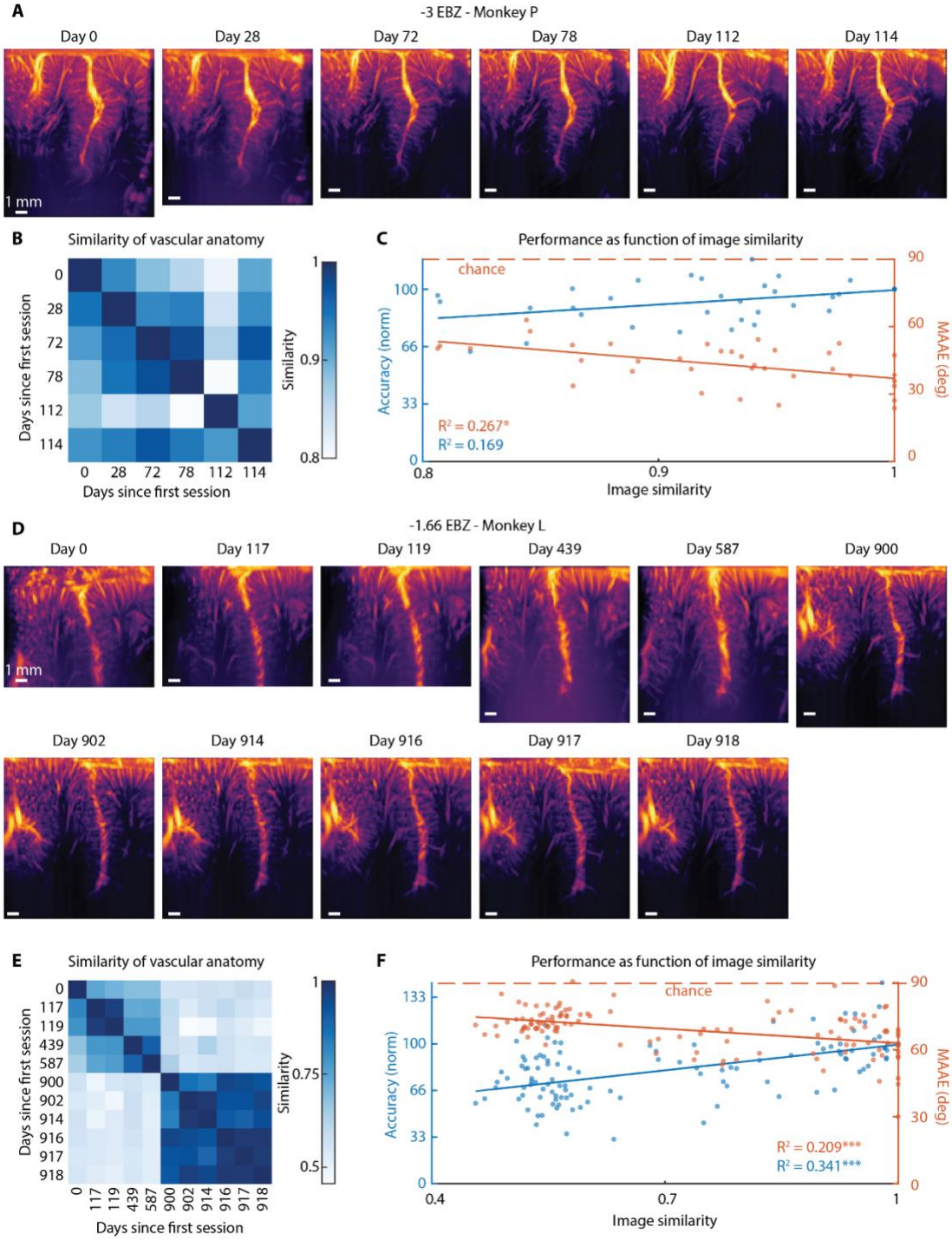

Supplemental Figure 3.2 Impact of image similarity on decoder performance.
(A) Vascular anatomy for each recording session from the same recording slot in Monkey P. White scalebar – 1 mm. (B) Pair-wise similarity between different vascular images for Monkey P. (C) Performance as a function of image similarity for Monkey P. Left axis (blue) shows normalized accuracy. Right axis (orange) shows mean absolute angular error (MAAE). Each session is represented by a pair of blue and orange dots. *=$p<10^{-2}$, **=$p<10^{-4}$, ***=$p<10^{-6}$. (D-F) Same format as (A-C) for Monkey L.

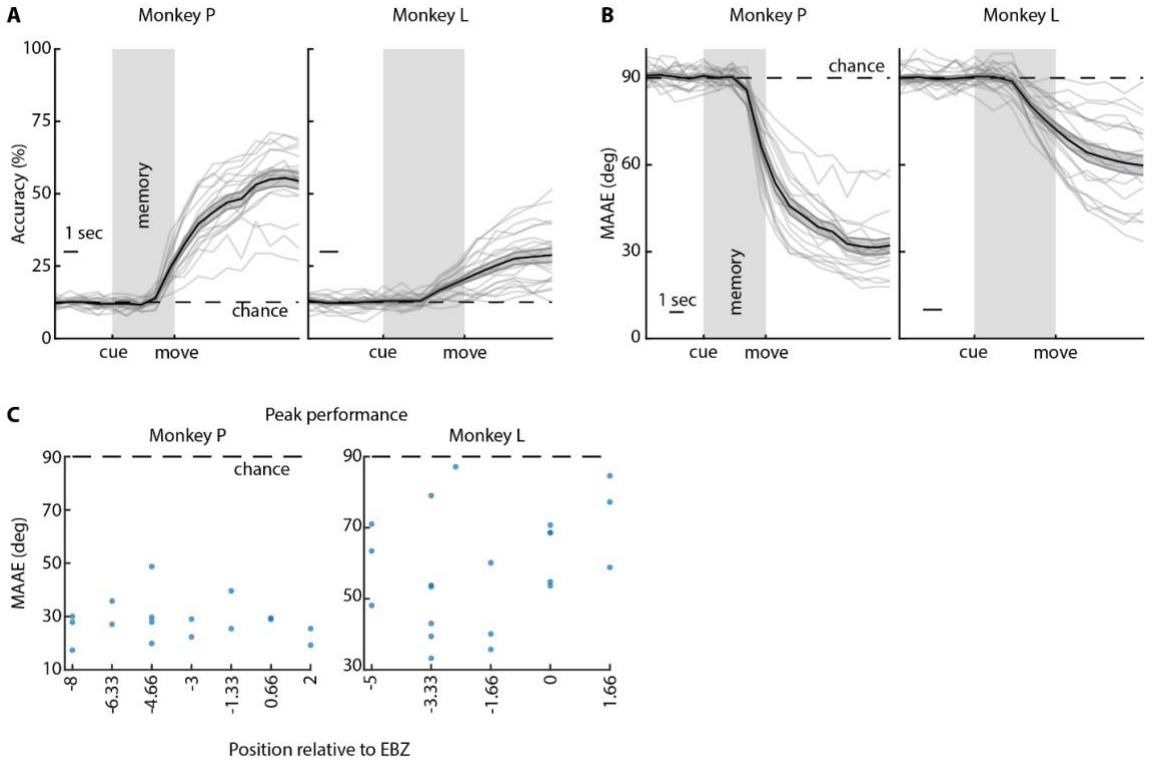

Supplemental Figure 3.3 Linear decoders can decode intended movement direction from most fUSI sessions, regardless of PPC plane.
(A) Percent correct for each session. Solid black line with gray envelope show mean ± SEM. Each gray line shows performance on single session. Dashed line shows chance level. (B) Mean absolute angular error (MAAE) for each session. Same format as in (A). (C) MAAE as function of coronal plane.

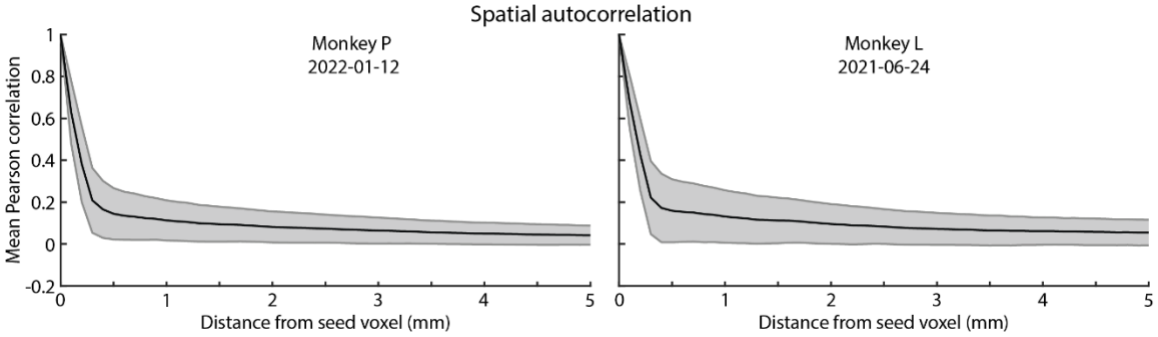

Supplemental Figure 3.4 Power Doppler data displays spatial autocorrelation.
Mean Pearson spatial autocorrelation across entire fUSI field. Voxel radius – Distance of voxels from center seed voxel. Shaded area – Standard deviation

3.6.2 Supplemental movies

Supplemental Movie 3.1 Anatomy in Monkey P
3D reconstruction of vascular anatomy in Monkey P.

Supplemental Movie 3.2 Anatomy in Monkey L
3D reconstruction of vascular anatomy in Monkey L.

4 Decoding of non-directional signals from PPC

4.1 Background

To develop an effective brain-machine interface (BMI), it is crucial to decode not only **what** a subject wants to do, but also **when** they want to execute the action. The posterior parietal cortex (PPC) is a good candidate brain region for decoding both the when and the what of intended actions, because PPC contains not only information about the spatial aspects of planned actions, but also the temporal sequence of those actions. Most experiments aimed at elucidating the neurophysiology behind movement planning and execution use trial-based tasks with distinct temporal states. These temporal states frequently include a fixation or baseline period, a cue period that tells the subject the desired action, a memory period to temporally separate the visual and motor components, a movement period where the cued movement is performed, and an intertrial interval where the subject can perform freely paced behavior before the next trial begins. At the microscopic level, electrode-based BMIs implanted in PPC can be used to decode current task state (Pesaran et al., 2002; Shenoy et al., 2003; Bokil et al., 2006; Hudson and Burdick, 2007; Hwang and Andersen, 2009; Campos et al., 2010; Diomedi et al., 2021). At the macroscopic level, fMRI studies have identified regions of the parietal cortex that contain macroscopic information about task timing (Bode and Haynes, 2009) and task strategy (Braver et al., 2003; Crone et al., 2006; Rowe et al., 2008). This suggests that that we may be able to decode which task state the monkey is currently experiencing from mesoscopic PPC using fUSI.

In addition to movement direction and action timing, LIP is modulated by multiple decision variables of upcoming movements, including expected reward (Platt and Glimcher, 1999; Dorris and Glimcher, 2004; Musallam et al., 2004; Sugrue, 2004; Sugrue et al., 2005; Iyer et al., 2010; Ghazizadeh et al., 2018), cue salience (Leathers and Olson, 2012), reward uncertainty (Foley et al., 2017; Horan et al., 2019; Li et al., 2022), stimulus category (Freedman and Assad, 2006), and task context (Zhang et al., 2017). LIP is thought to encode the relative desirability of actions by integrating information from multiple sources (Dorris and Glimcher, 2004; Sugrue et al., 2005; Gottlieb and Snyder, 2010; Christopoulos et al., 2015). These prior findings suggest that LIP and other PPC regions may encode other variables related to action desirability, including physical effort of a movement and object novelty.

Previous researchers have examined whether LIP is modulated by object novelty. At the microscopic level (single-unit), novelty enhances the neural response slightly (Foley et al., 2014) while at the macroscopic level (fMRI), LIP does not appear to be modulated by novelty (Ghazizadeh et al., 2020). Using fUSI to examine the responses within mesoscopic PPC populations can help resolve this apparent discrepancy between the microscopic and macroscopic levels.

Despite ample evidence at the microscopic (single neuron) and macroscopic (fMRI) level of reward modulation within LIP, much remains unknown about how reward and other desirability variables are encoded within PPC. First, are these desirability variables encoded at the mesoscopic level within LIP and PPC? Second, are there PPC regions modulated by effort? Third, are the regions encoding these different variables overlapping or separate?

Here, we investigated where and how these non-directional variables are represented across PPC regions at the mesoscopic population level. This will help inform us about possible control signals that we can decode from the PPC using fUSI. As discussed in more depth later (**Chapter 5.3.6**, **Chapter 7.2.1**), ultrasonic BMIs have a number of features that would make them a good platform for neuropsychiatric BMIs. Being able to decode reward, effort, novelty, and other "cognitive" variables are related to many neuropsychiatric illnesses and suggest that we could track biomarkers relevant to depression, anxiety, or other mental health issues. Investigating where and how these non-directional variables are represented across PPC will also inform us about possible sources of variability in other signals we want to decode from PPC. For example, if we are only interested in direction of the movement, then we want to be aware of and compensate for the effect of different rewards or outcomes associated with different movement directions.

4.2 Results

4.2.1 Decoding of task state

To test whether PPC contains mesoscopic information related to task timing, we used the data previously collected for **Chapter 3** where Monkey P and Monkey L performed memory-guided saccades. This memory-guided movement task had seven discrete task states (**Figure 4.1A**): fixation period, cue, memory period, saccade, target hold, reward delivery, and intertrial interval (ITI). To get an intuition for the task-related information contained with mesoscopic PPC, we examined the trial averaged activity across our imaging plane (**Figure 4.1B** and **Supplemental Movie 4.1**). Different regions of the image had different activity with a few shared patterns. In an example session, region

of interest (ROI) 1, within the dorsal LIP, was activated during both the memory period and start of the ITI; ROI 2, within a large blood vessel supplying the intraparietal sulcus, showed modest activation during the memory activity with the most activity at the start of the ITI; ROI 3, within the ventral MIP, had sustained activity from the end of the memory period through the reward delivery; and ROI 4, within white matter adjacent to the ventral MIP, had little activity to any task state. All of the ROIs displayed increased activity at the start of the trial that decreased before the cue onset. These different patterns of activity suggested that PPC contained mesoscopic populations tuned to different aspects of the task and that we might be able to use these distributed spatiotemporal patterns to decode the current task state.

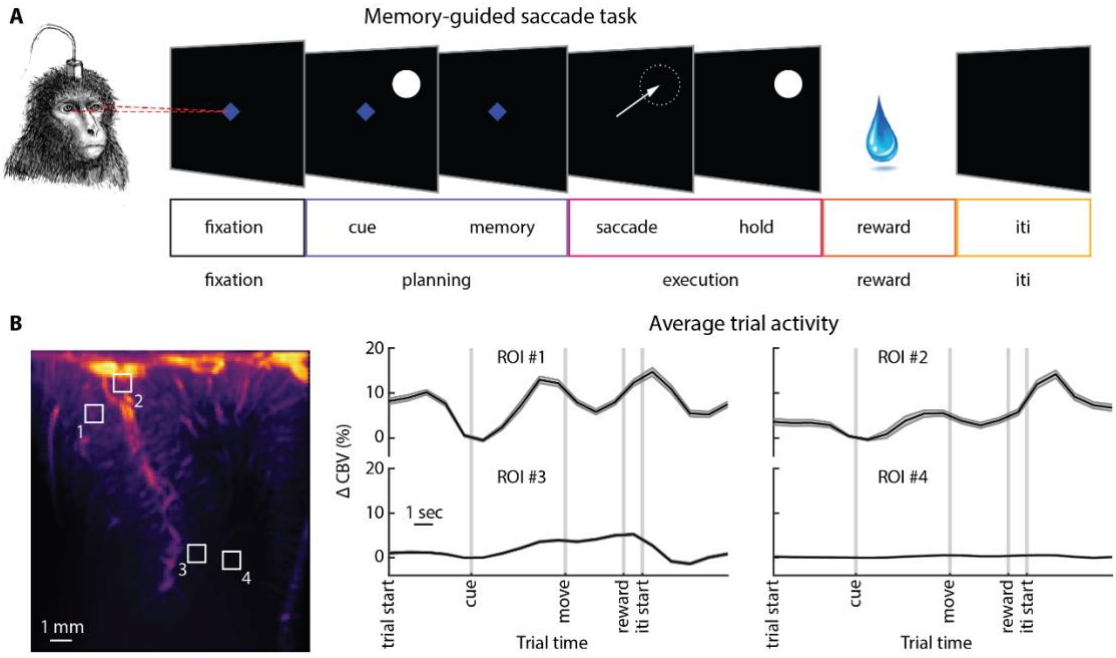

Figure 4.1 Complex spatiotemporal patterns across PPC during saccade task states.
(A) Task design. We combined the seven discrete states into 5 meta-states: fixation, movement planning, movement execution, reward, and intertrial interval (iti). (B) Example trial activity for different ROIs. (C) Histogram of raw task labels, unbalanced meta-labels, and balanced meta-labels. (D) Transition graph between the five meta-states showing probability of transitioning to same or different state on subsequent fUSI frame. (E) Example task decoding of three sequential trials. (F) Confusion matrix showing decoding performance. Rows sum to 100%. (G) Searchlight analysis showing 10% most significant voxels.

Unlike the analysis discussed in **Chapter 3.2.2** where we used multiple timepoints to decode the intended movement direction, here we tried to identify the current task state based upon a single fUSI timepoint. In other words, can we identify what task state an arbitrary fUS image is from? Since our fUSI acquisition systems recorded hemodynamic data at 1-2 Hz, we could not temporally resolve

some of the shorter task states (e.g., saccade from target hold). To handle this, we grouped the task states into five meta-states relevant to movement decoding: initial fixation, movement planning, movement execution, reward delivery, and ITI. These task meta-states were different lengths such that certain meta-states had more fUSI frames (**Figure 4.2A**). To prevent any bias in our trained model towards the most common classes, we balanced our dataset by randomly selecting N fUSI frames from each meta-state, where N is the number of fUSI frames in the smallest meta-state. In the example session shown, there was ~400 fUSI frames per meta-state. We successfully decoded the current task state on 60.6% of samples, well above the chance level of 20% (1434/2365 samples; p<1e-15; 1-sided binomial test). Example decoding during three sequential trials showed the decoder predicted the overall task flow fairly well, but temporally adjacent states were frequently confused (**Figure 4.2C**). The confusion matrix agreed with this temporal confusion. Neighboring meta-states (e.g., planning and execution) were more commonly confused than meta-states that were temporally separated (e.g., fixation and execution) (**Figure 4.2D**).

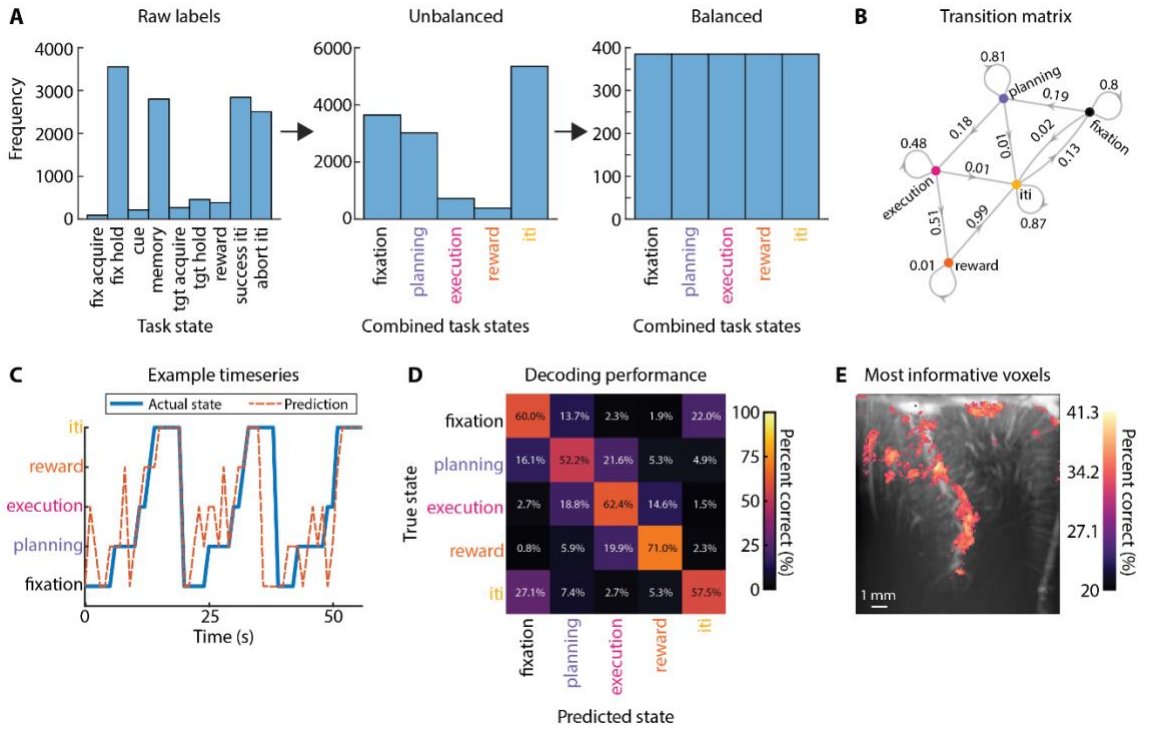

Figure 4.2 High decoding accuracy for individual task states using single Power Doppler images.
(A) Histogram of raw task labels, unbalanced meta-labels, and balanced meta-labels. (B) Transition graph between the five meta-states showing probability of transitioning to same or different state on subsequent fUSI frame. (C) Example task decoding of three sequential trials. (D) Confusion matrix showing decoding performance. Rows sum to 100%. (E) Searchlight analysis showing 10% most significant voxels.

To better understand what portions of the image contained the most information about task timing, we performed a searchlight analysis (**Figure 4.2E**). The 10% most informative voxels were distributed throughout the image, including within Area 5, Area 7a, dorsal LIP, MIP, and the main blood vessel(s) running within the intraparietal sulcus. This suggests that information about task timing is distributed across multiple PPC regions, consistent with each of these PPC regions being involved in different types or phases of movement planning.

As a stronger test of this task decoding, we tested our decoder's performance on a hold-out session. Similar to **Chapter 3.2.3**, we trained the decoder on all the balanced data from a training session and tested its ability to decode on a separate session collected 28 days later. The decoder predicted 39.8% of the task states correctly (972/2445; $p<1e-15$), a substantial drop in performance but still well above chance level. This shows that the identified task-related spatiotemporal patterns are consistent across sessions and that an ultrasonic BMI would require minimal, if any, retraining to be able to decode task state on subsequent days, an ideal trait for a BMI.

4.2.2 Behavioral evidence of learning object outcome associations

Having demonstrated that we could successfully decode task timing information from PPC, we next examined the encoding of non-motor variables. We trained two monkeys (Monkey L and Monkey H) on a modified memory-guided saccade task where the cue stimulus indicated different outcomes (**Figure 4.3**) We paired complex abstract visual stimuli ('fractals') with specific outcomes consistently so that each monkey learned the paired outcome via operant conditioning (Miyashita et al., 1991; Yamamoto et al., 2012).

We first varied the amount of reward associated with different visual objects. We divided sets of eight or nine fractal objects into equal groups, each with a different level of reward. For example, in two-level reward sets, four objects were associated with a small reward (0.25 mL) and four objects were associated with a large reward (0.75 mL) (**Figure 4.3B**). We trained two monkeys (Monkey L and H) on the reward task. After four days of training on the task and a 2-fractal set (one high reward and one low reward), both monkeys chose the high-reward fractal significantly above chance (binomial test: Monkey L: 114/152 High/Total (75%) $p<0.0001$; Monkey H: 50/72 (69%) $p<0.0001$). This shows they understand the task and learned the rewards associated with the fractals despite minimal training. We additionally trained Monkey L on object sets with 3+ reward levels. Monkey L learned these multi-level reward sets rapidly. On his first day learning an object set with three reward levels (9 objects: 0.25, 0.75, or 2.25 mL reward), he chose the higher reward 82% of the time (56/68; $p<1e-$

15; 1-sided binomial test). After six days of training on a different object set with three reward levels, he chose the highest reward 94% of the time (68/72; p<1e-15; 1-sided binomial test). This further demonstrated that the monkeys robustly and easily learned the object-outcome associations, even for more complicated reward magnitude image sets.

We next tried to vary the amount of physical effort associated with different visual objects. For these eight object fractal sets, objects were paired with different target hold times (900 or 2700 ms). The longer hold times required more physical effort from the monkey to maintain their eye position at the eccentric location. Monkey L did not display a preference for objects with a shorter hold time. He chose the shorter hold 53% of the time (2 options: 900 or 2700 ms) (p=0.38, 23/43 choice task). We did not train Monkey H on this task type because we did not observe any behavioral difference in Monkey L for this task type.

We finally varied the novelty or familiarity of the experienced visual objects. Half of the objects were familiar objects seen on previous days and half of the objects were novel objects never seen before that day. All the objects in the novel-familiar sets received the same amount of reward. Previous literature has found that novel objects are more salient than familiar objects (Johnston et al., 1990; Park et al., 2010) with faster reaction time, increased number of saccades, and length of gaze to novel objects (Ghazizadeh et al., 2016). We tested Monkey L on multiple novel-familiar sets. We did not observe any difference in saccadic reaction time between novel and familiar objects (α=0.1; 2 sample t-test) across 4 sessions. We did not train Monkey H on this task type because we did not observe any behavioral difference in Monkey L for this task type.

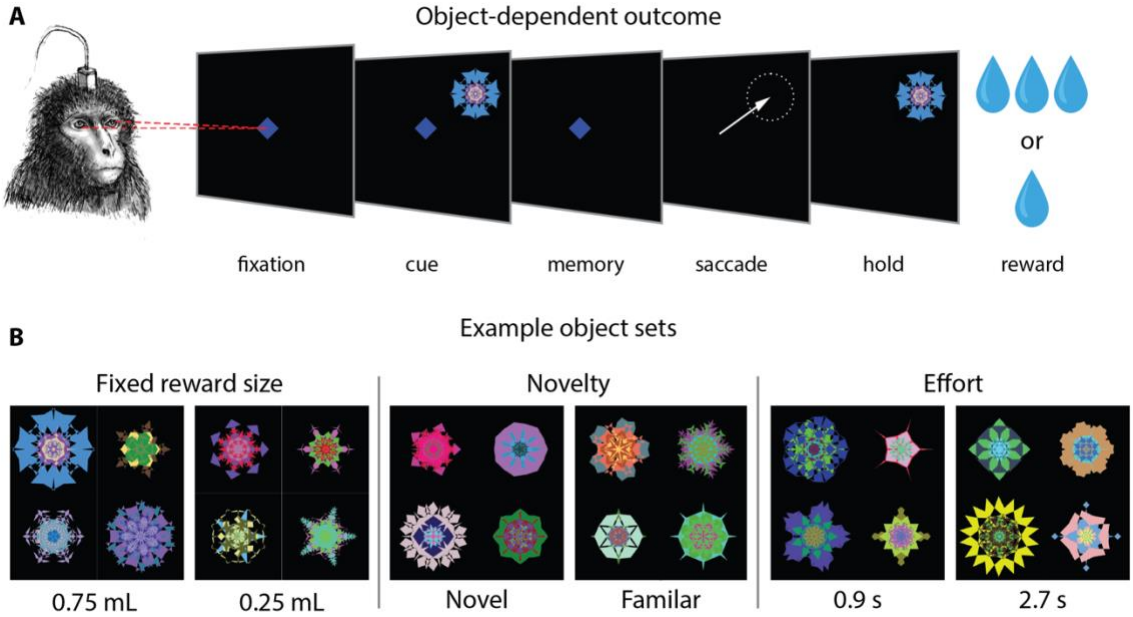

Figure 4.3 Memory-guided saccade task variant with complex visual cues.
(A) Variant of the memory-guided saccade task. A fractal cue was displayed in the periphery and indicated different outcomes, such as different reward amounts or target hold times. (B) Example object sets for reward size, novelty, and effort.

4.2.3 Reward magnitude

After confirming that the monkeys learned the different rewards associated with the fractal objects, we collected 1 Hz fUSI data while the monkeys made instructed saccades to the different fractals. We used a general linear model (GLM) to assess which voxels showed statistically significant modulation by reward value (**Figure 4.4A**). For the example session, we observed discrete mesoscopic populations within dorsal LIP that were modulated by the reward value of the instructed saccade target. These areas had increased hemodynamic activity for high reward objects (**Figure 4.4B**). We observed no such modulation within ventral LIP. Consistent with our previous results, specific portions of LIP displayed directional modulation with increased activity for contralateral saccadic targets (**Figure 4.4B – ROI 2**).

To assess the consistency of this reward modulation from trial to trial, we used a decoding analysis to predict the expected reward size from the recorded fUSI data. As in **Chapter 3.2.2**, we tested the decoding ability across the entire trial. In an example session, decoding performance for reward size reached significance at the end of the memory period and continued to improve through the movement phase (**Figure 4.4C**) to 85.2% correct. The confusion matrix showed that both classes had

similar accuracies (**Figure 4.4D**). To understand which parts of PPC contained the most information about reward size, we performed a searchlight analysis with a 200 μm radius. The 10% most significant voxels were in LIP, Areas 1/2, and superficial layers of Area 5 (**Figure 4.4E**).

The GLM analysis revealed that some areas were modulated by both direction and reward size. To understand the consistency of these modulations, we performed another decoding analysis where we simultaneously decoded reward size and movement direction (**Figure 4.4F**). The decoder performance was more variable but reached significance at the end of the memory period and improved through the movement phase to 64.7% correct. The confusion matrix showed that certain classes were decoded better (**Figure 4.4G**). As expected from **Chapter 3**, the decoder performed well for direction classification (contralateral vs ipsilateral). The decoder had high accuracy at classifying reward size for contralateral movements but had higher confusion for ipsilateral movements. There was also modest confusion between contralateral and ipsilateral high rewards. To identify the PPC areas containing information about both reward size and movement direction, we used a searchlight analysis with a 200 μm radius (**Figure 4.4H**). The 10% most informative voxels were within the same areas as identified by the reward-only searchlight, but noisier. Additionally, many informative voxels were within the central sulcus.

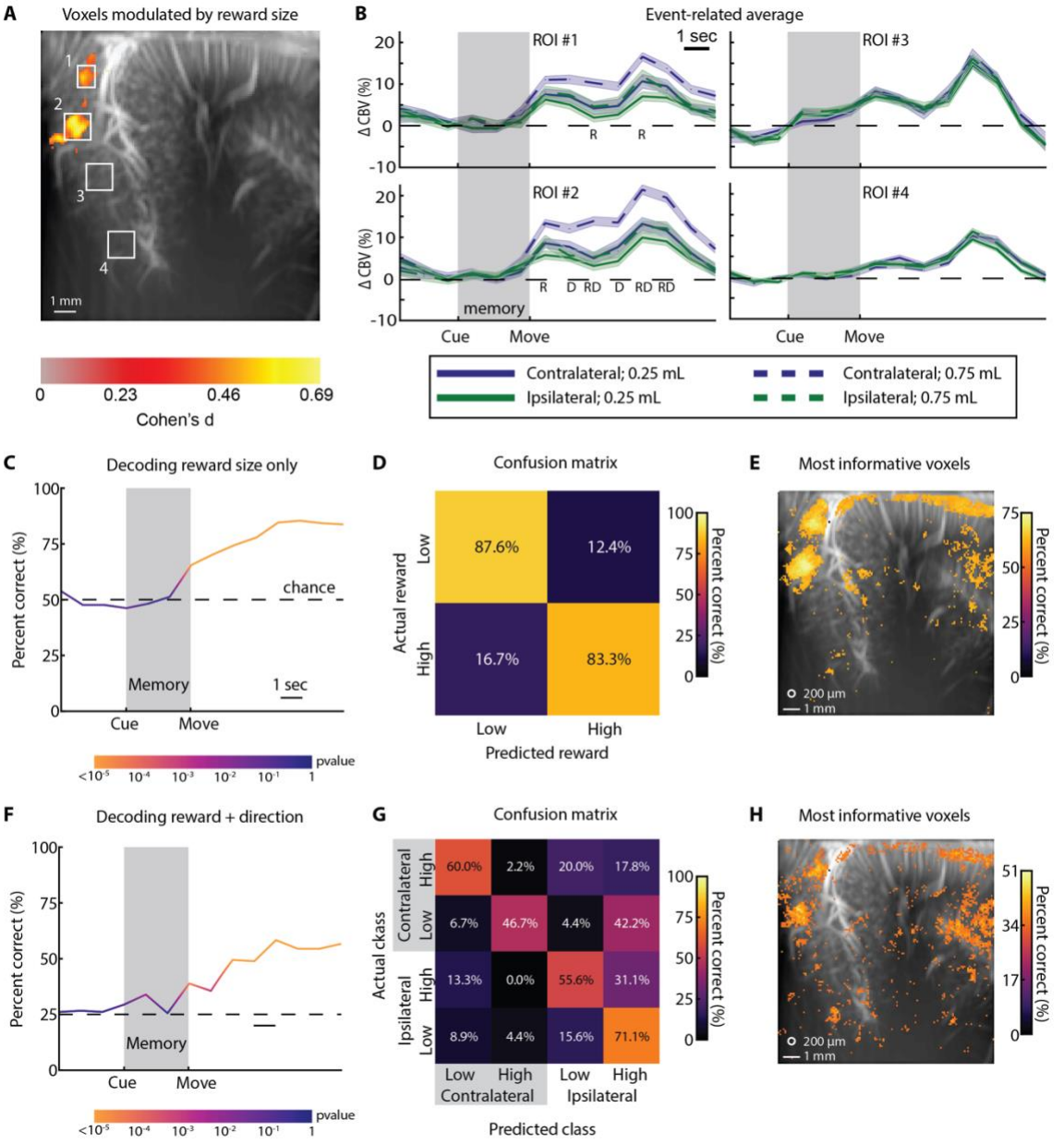

Figure 4.4 Distinct mesoscopic PPC populations encode for reward magnitude.
(A) Statistical parametric map showing the regions with a statistically different activity during the memory period for low-reward and high-reward objects. Voxel threshold determined by GLM t-contrast where q<0.05 (FDR-corrected). White scale bar – 1 mm. (B) Event-related average of activity within each ROI. Each line represents one condition (direction X reward level). Letters represent significant 2-way ANOVA results (p<0.05 with Bonferroni correction for number of timepoints). R = significant effect of reward; D = significant effect of direction; x = significant interaction term. (C) Decoding performance (percent correct) as a function of trial time. Dashed line shows chance performance. Color of line represents statistical significance (1-sided binomial test). (D) Confusion matrix of decoding represented as percentage (rows adds to 100%). (E) Searchlight analysis showing 10% most significant voxels. White circle – 200 µm searchlight radius. White line – 1 mm scalebar. (F-H) Same format as C-E for decoding reward + direction simultaneously.

4.3 Discussion

Here, we demonstrated that not only can we decode the intended movement direction from PPC (**Chapter 3**) but can also decode the task state and other non-motor variables. This prepares for future work on using ultrasound as a high-performance BMI for a variety of applications.

4.3.1 Decoding task state

Our fUSI linear decoder could decode the major task states (fixation, movement planning, movement execution, reward delivery, and intertrial interval) at well above chance level using just single fUSI frames (**Figure 4.2D**). This builds off our prior work where we demonstrated we could robustly decode memory from non-memory states (**Figure 2.6**) (Norman et al., 2021). Detecting movement initiation is an important first step for a motor BMI to decode free behavior (as opposed to task structured behavior) but decoding multiple task states enables a richer repertoire of actions possible with a BMI.

The decoder performance in the example session reached 60% with the most confusion for temporally adjacent task states. This temporal confusion is expected because movement preparation follows spatiotemporally precise patterns, especially in repetitive task-confined settings (Churchland and Shenoy, 2007; Churchland et al., 2010, 2012). The monkey knows the task structure very well and will be anticipating the next state before it occurs. This means that the fUSI data at the end of one task state and start of the next state will be very similar. This likely leads to decreased performance in our single timepoint task decoder.

4.3.1.1 Previous literature

Previous literature has examined the encoding of task states and timing within PPC at the microscopic, mesoscopic, and macroscopic levels. At the microscopic level, several studies have used single units and LFP activity within PPC for BMI applications. Changes in different LFP power bands of the parietal reach region (PRR) could be used as a robust indicator of movement onset and researchers trained a monkey to control a go/no-go BMI task using these PRR LFPs (Hwang and Andersen, 2009). Previous work found that LFP and/or single-unit activity from LIP could be used to decode two task states (movement planning and execution) (Pesaran et al., 2002) and time of saccadic initiation (Bokil et al., 2006). Later work found that spiking activity from multi-electrode arrays recording populations of LIP neurons could decode temporal intervals (9 states of saccade task) above chance level using a k-nearest neighbor decoder (Campos et al., 2010). However, this work

interestingly found temporal information could be substantially better decoded from Supplemental Eye Field (SEF) rather than LIP (Campos et al., 2010). Building off these simpler decoder models, researchers have also used spiking activity from PRR neurons paired with a finite state machine or Hidden Markov Model (HMM) to offline decode neural activity associated with different task states and movement directions (Shenoy et al., 2003; Hudson and Burdick, 2007; Diomedi et al., 2021, 2022).

At the mesoscopic level, we showed that fUSI can decode go/no-go signals from the PPC (Norman et al., 2021). At the macroscopic level, researchers used human fMRI to show that PPC could be used to decode the current task set (Bode and Haynes, 2009). The results we showed here agree with this previous literature and show that mesoscopic PPC recordings are capable of more than just decoding go/no-go and can differentiate between many different task states.

Outside of PPC, fUSI has been used to decode different temporal states from single fUSI frames at above chance level in rodents (Berthon et al., 2023). They used a three-layer fully-connected artificial neural network (ANN) to successfully decode between two movement states at 98±1% accuracy and between four wake/sleep states at 87±4%. However, as they note, their model suffered from a temporal data leak introduced by using temporally autocorrelated data in both their train and test sets. In the results we reported here, we prevented a similar temporal data leak by defining the cross-validation folds at the level of individual trials rather than individual timepoints. This ensured that there was never training and testing data from the same trial and that no temporal autocorrelation could drive our significant decoding. This difference in cross-validation schemes makes it difficult to directly compare the decoding performance of our linear decoder and their ANN, but most likely their ANN exceeded the performance we obtained by 10-20%. The reason for this performance difference is unknown and warrants investigation in future studies, including testing their ANN architecture on our current dataset.

4.3.1.2 Future improvements

The peak performance we obtained for decoding between multiple task states was only 60.6% so there is still much room for future development of the task state decoding. We have several ideas of how to boost the performance.

First, one of the simplest ways to boost the performance may be to increase the fUSI framerate. As we discussed above, we had high confusion for temporally adjacent task states. Additionally, we

combined task states together into meta-states because some task states were substantially shorter than 500-1000 ms, preventing us from reliably collecting fUSI frames during specific states, such as during the target acquire state (the time between the end of the memory state and the end of the saccade to the remembered target location). Faster framerate (6-10 Hz) fUSI is already possible (although it comes with reduced sensitivity to changes in CBV) (Dizeux et al., 2019; Brunner et al., 2020, 2021). Faster framerate fUSI will not overcome the challenges of distinguishing temporally adjacent states, especially if the temporally adjacent states evoke similar neural states. However, it may help in at least two ways. First, faster sampling rate would allow more precise estimates of state transitions. Second, faster framerates may increase confidence in the prediction of certain task states by averaging multiple adjacent temporal predictions together. Additional research would be needed to find the balance between increasing the framerate and maintaining a sufficient signal-to-noise ratio.

A second way to boost the performance may be to use multiple timepoints to form each prediction. In the current analyses, we took arbitrary shuffled timepoints and tried to classify them. In a real-world application, the test data would be contiguous in time. This continuity could be leveraged in several ways.

1) Multiple sequential timepoints can be fed into the decoder instead of solitary timepoints. Although this would increase the decoder latency, it would help reduce the noise between adjacent timepoints and may identify spatiotemporal patterns not possible with the current decoder architecture. This approach will also become more practical as the framerate of fUSI increases in the future, thus reducing the decoder latency even when using multiple timepoints. A similar approach has been used by electrode-based BMIs (Achtman et al., 2007).
2) With contiguous data, the decoder algorithm could be adjusted to only allow valid state transitions, such as via a finite state machine (Shenoy et al., 2003). For example, in the memory-guided task, it is impossible for the task to go from fixation to movement execution (**Figure 4.2B**). The current model does not prevent such impossible state transitions. An improved model would use its knowledge (or prediction) of the current state to predict future valid states rather than impossible states. In a laboratory setting, it is possible to identify and label relevant task states. In real-world applications, it can be very difficult and time-consuming to label behavioral data, although various methods have been

developed to help overcome this challenge (Mathis et al., 2018, 2020; Berger et al., 2020; Lauer et al., 2022).

3) A Hidden Markov Model (HMM), Long Short Term Memory network (LSTM; type of recurrent neural network), transformer neural network, or other stochastic model could be used to better model and predict the task states. Since certain state transitions are much less likely or even impossible (**Figure 4.2B**), the decoder can use the probability of each transition to weight its training and develop a temporal model. In the context of a BMI for neuropsychiatric applications, an example would be that it is highly unlikely to rapidly transition from happy to depressed, anxious to not anxious, or other opposite mood states. Rather, it would be expected for there to be no transition or a slow transition through intermediate mood states. An effective neuropsychiatric BMI should incorporate this information such that it does not intervene (e.g., stimulate) when unnecessary or stop intervening when necessary. Supervised HMMs (and variants) have already been used for several BMI applications (Hudson and Burdick, 2007; Kemere et al., 2008; Bollimunta et al., 2012; Kao et al., 2017a; Diomedi et al., 2022). Unsupervised HMMs may also be useful for finding latent neurovascular states that are behaviorally relevant but difficult to label, such as for fUSI data collected during free behavior. More recently, LSTM networks have become popular and can exceed the performance of HMMs with sufficient training data (Anumanchipalli et al., 2019; Makin et al., 2020; Tadayon and Pottie, 2020; Moses et al., 2021; Willett et al., 2021).

A third way to boost performance may be to record from a different brain region. Here, we recorded from PPC, but there are other regions known to be important for preparation and initiation of action sequences, including the basal ganglia (Klaus et al., 2019) and motor cortex (Ebbesen and Brecht, 2017; Svoboda and Li, 2018). Since the basal ganglia and motor cortex are downstream of the PPC and involved in gating movement execution, the signals from these areas may allow more precise estimates of action initiation. Recording from the subthalamic nucleus would additionally be useful in detecting movement stop signals (Aron and Poldrack, 2006). Such a signal would be critical for users to decide if they wanted to abort a decoded action sequence.

We expect that these lines of research, or closely related ones, will be useful in boosting the performance of future task state decoding from fUSI data.

4.3.2 Encoding of reward magnitude within PPC

We demonstrated that we could decode the expected reward magnitude paired with different visual stimuli (**Figure 4.4C-E**) and could also simultaneously decode expected reward magnitude and movement direction (**Figure 4.4F-H**). The observed change in CBV for different reward levels depended upon the movement direction (contra/ipsi) and was weaker than that observed for encoding of only movement direction (<5% CBV change instead of 20+%). With the GLM analysis, we only observed reward modulation within the dorsal LIP.

4.3.2.1 Previous literature

There has been extensive previous literature on the encoding of reward magnitude by individual LIP neurons (Platt and Glimcher, 1999; Musallam et al., 2004; Sugrue et al., 2005; Louie et al., 2011) although there has been some recent disagreement about whether LIP is encoding economic utility or the information gain from reducing uncertainty about action outcomes (Horan et al., 2019; Li et al., 2022). All of these papers used single-neuron recordings of LIPs and found that in saccade tasks, receptive field stimuli paired with larger rewards were associated with increased firing rates. Our observed results match this literature where we saw that discrete patches of dorsal LIP had increased activity for stimuli and saccades associated with higher rewards (**Figure 4.4A-B**).

At the macroscopic level, previous fMRI work has found that dorsal LIP had increased hemodynamic response to stimuli paired with large rewards (Ghazizadeh et al., 2018, 2020). They used a block related design where the monkey fixated on a center point and passively viewed fractals flashed in one visual hemifield's periphery. The passively shown fractals had been previously associated with either a large or small reward. They found a stronger contralateral response for reward magnitude. Our fUSI results match these fMRI results where we saw stronger responses to high reward objects both for contralateral and ipsilateral targets, but the strongest response to contralateral high-reward targets (**Figure 4.4A-B**).

4.3.2.2 Future work

Having demonstrated that there are mesoscopic populations tuned to reward magnitude, we want to better understand how these signals scale with reward magnitude in the mesoscopic populations we identified. Previous literature has shown that at the single neuron level, the response magnitude depends on the full choice set and is scaled according to divisive normalization (Louie et al., 2011). Our current fUSI dataset contains sessions with instructed saccades to objects drawn from image sets with 2, 3, or 5 levels of rewards. Each session also typically has images drawn from multiple different

sets, allowing us to compare the scaling of the hemodynamic response not only within an image set, but between image sets. Combining this rich dataset with new analyses and additional experiments will be useful for exploring whether a divisive normalization model best explains the observed reward modulation at the mesoscopic scale.

4.3.3 Novelty

We failed to find any behavioral difference between novel and familiar stimuli during our memory-guided saccade task for instructed or choice trials. Previous work has demonstrated robust novelty effects in a variety of species (Jaegle et al., 2019), including humans (Johnston et al., 1990; Park et al., 2010; Wang and Mitchell, 2011) and monkeys (Butler, 1953; Ghazizadeh et al., 2016; Ogasawara et al., 2022). We do not know why we did not observe a novel-familiar difference in our monkey. One possible explanation is that we used a memory-guided saccade task while most previous monkey studies used a free-viewing paradigm where the monkeys were free to look at any stimuli on the screen without their saccades influencing their reward. This difference in task may have obscured the monkey's preference for novel objects if the monkey just wanted to advance the trial as rapidly as possible and realized his choice between objects did not influence his reward level. Additional training and/or revised experiments will be needed to better examine whether novelty is encoded within mesoscopic PPC.

4.3.4 Effort

We failed to find any behavioral difference between stimuli or actions paired with different physical efforts. We hypothesize this might be due to eye movements being almost effortless. Humans make ~3 saccades/second (Ibbotson and Krekelberg, 2011), and we do not consciously think of these movements, except for very eccentric eye movements. Our task design used long hold times to try to increase the effort of eye movements, but it is likely that the movement was still effortless for the monkey. Additionally, long hold times are mildly aversive because it delays the reward delivery and decreases down the maximum amount of reward the monkey can receive per unit time. If the monkey understood the task, we would expect the monkey to choose the object with the shorter hold time to maximize their reward rate, i.e., become skillful at completing the task as fast as possible (Hikosaka et al., 2013). This suggests that the monkey did not understand the object-associated outcomes or did not care about the different hold times.

Using a different effector, such as a force joystick, in place of the eye tracking may help better explore the encoding of movement effort. A force joystick would allow the researcher to explicitly set

different amounts of force that the monkey needs to exert to move the joystick or complete the task. This would allow a more conventional exploration of effort rather than trying to make effortless eye movements into unnatural effortful eye movements.

4.3.5 Future work

We have already highlighted several questions about how task timing, reward magnitude, novelty, and effort are each separately encoded within PPC. Additional work is also needed to explore how different combinations of these variables are encoded and how they influence the encoding of direction we characterized in **Chapter 3**. Previous work has proposed schemas about how desirability of different actions might be computed within PPC and used to decide upon the optimal action (Christopoulos et al., 2015). fUSI's ability to record from entire PPC planes and monitor multiple brain regions may offer novel insight into how the desirability of different actions with single or multiple effectors is computed.

4.3.6 Conclusion

In this chapter, we explored how non-directional signals were represented within PPC, including task timing and reward magnitude. We found that PPC contained distributed spatiotemporal patterns that allowed us to identify the major states of our task, including initial fixation, movement planning, movement execution, reward delivery, and intertrial interval. This supports future work on developing an ultrasonic BMI that can decode not only the user's intended actions but also the timing of those actions.

We found that reward magnitude led to increased activity within the dorsal LIP and that we could use a linear decoder to simultaneously decode direction (contra/ipsi) and reward magnitude (high/low). This supports future work on developing an ultrasonic BMI that can detect non-motor signals for neuropsychiatric applications, such as detecting and correcting aberrant mood states.

4.4 Materials and Methods

These methods closely follow those described in **Chapter 3**.

4.4.1 Experimental model and subject details

All training, recording, surgical, and animal care procedures were approved by the California Institute of Technology Institutional Animal Care and Use Committee and complied with the Public Health Service Policy on the Humane Care and Use of Laboratory Animals. We worked with three rhesus macaque monkeys (*Mucaca mulatta*; 14-years old, male, 14-17 kg). Monkey L participated in all experiments. Monkey H participated in the object-dependent outcome experiments. Monkey P participated in the task state decoding experiments.

4.4.2 General

4.4.2.1 Animal preparation and implant

We implanted a titanium headpost and custom square recording chamber on each monkey's skull under general anesthesia and sterile surgical conditions. We printed or machined each 24 x 24 mm (inner dimension) chamber using Onyx filament (Markforged), PEEK, or Ultem. We placed the recording chamber over a craniectomy centered above the left intraparietal sulcus.

4.4.2.2 Behavioral setup and task

Each monkey sat head-fixed in custom-designed primate chairs facing an LCD screen ~30 cm away. We used a custom Python 2.7 software based upon PsychoPy (Peirce, 2007) to control the behavioral task and visual stimuli. We tracked their left eye position using an infrared eyetracker at 500 Hz (EyeLink 1000, Ottawa, Canada). Eye position was recorded simultaneously with stimulus information for offline analysis.

Monkeys performed a memory-guided saccade task (**Figure 4.3A**) where they fixated on a center dot (fixation state), maintained fixation while a peripheral cue was flashed for 400 ms in one of eight locations (20d eccentricity, equally spaced around circle), continued to maintain fixation on center dot (memory state), and finally made a saccade to the remembered cue location (movement state). If they correctly made a saccade to the cued location, then the peripheral cue was redisplayed and the monkey had to maintain fixation on the peripheral target until the liquid reward was delivered. The target cue was an abstract visual object paired with different outcomes. We used a Latin square pseudo-randomization scheme to avoid any consistent patterns of sequential object presentations.

To assess any preference for specific objects, we used choice trials where two fractal objects were diametrically presented (e.g., upward left and downward right) during the cue state. During the movement state, the monkey made an eye movement to one of the remembered eye positions and received the outcome associated with the fractal in that target location. Similar to the instructed saccade task, both fractals appeared once the monkey made a saccade to either remembered location.

4.4.2.3 Modifying action reward

To modify the reward magnitude, we replaced the peripheral cue with complex visual objects ('fractals') consistently associated with a large or small juice reward (**Figure 4.2B**). These visual objects were organized into sets of eight, nine, or ten objects. The sets of eight objects had four objects with low reward and four objects with high reward. The sets of nine objects had three objects with low reward, three objects with medium reward, and three objects with high reward. The sets of ten objects had five pairs of fractals, each associated with a different reward level. On each training day, each object in an object set was experienced the same number of times to avoid differences in perceptual exposure.

For the choice trials, we included all comparisons, including fractals with the same reward level.

4.4.2.4 Modifying action effort

To modify the physical effort, we varied the duration of the target hold. As with the reward magnitude sets, fractal objects were consistently associated with different target hold times (**Figure 4.3B)**. As with the reward task, we included choice trials where the monkey chose between two fractals with equal or different effort levels to allow us to test whether PPC regions encodes relative and/or absolute movement effort.

For the choice trials, we included all comparisons, including fractals with the same effort level.

4.4.2.5 Novel and familiar object sets

To explore the effect of novelty on PPC, we developed novel-familiar sets of eight objects. Four objects were novel objects never seen before that day. Four objects were familiar objects previously experienced on multiple days. All objects received the same reward size (0.25 mL).

4.4.3 Functional ultrasound imaging

We used a programmable high-framerate ultrasound scanner (Vantage 256; Verasonics, Kirkland, WA) to drive the ultrasound transducer and collect pulse echo radiofrequency data. We used a custom plane-wave imaging sequence to acquire the 1 Hz Power Doppler images. We used a pulse repetition

frequency of 7500 Hz with 5 evenly spaced tilted angles (-6° to 6°) with 3 accumulations to create one high-contrast compounded ultrasound image. We acquired the high-contrast compound images at 500 Hz and saved the images for offline construction of Power Doppler images. We constructed each Power Doppler image using 250 compound images acquired over 0.5 seconds. To separate the blood echoes from background tissue motion, we used a SVD clutter filter (Demené et al., 2015). For more details on the functional ultrasound imaging sequence and Power Doppler image formation, please see (Macé et al., 2013; Norman et al., 2021).

We used a 15.6 MHz ultrasound transducer (128-element miniaturized linear array probe, 100 μm pitch, Vermon, France). This transducer and imaging sequenced provided us with a 12.8 mm (width) and 13-20 mm (height) field of view. The in-plane resolution was approximately 100 μm x 100 μm with a plane thickness of ~400 μm. During each recording session, we placed the ultrasound transducer on the dura with sterile ultrasound gel. We held the transducer using a 3D-printed slotted chamber plug that minimized motion of the transducer relative to the brain. The slots were spaced 1.66 mm apart. This slotted chamber plug allowed us to acquire specific imaging planes across sessions. To help with later offline data concatenation, we acquired vascular maps using a single Power Doppler image and adjusted the transducer until the acquired vascular map closely matched a previously-acquired vascular image for that chamber slot.

4.4.4 Across session alignment and concatenation

We concatenated data across multiple sessions for each imaging plane. We first performed a semi-automated intensity-based rigid-body registration to align the vascular anatomy between sessions. As described above, during the acquisition, we minimized out-of-plane movement between sessions by matching each session's imaging plane to a previously acquired template image for each chamber slot. See (Griggs et al., 2022) for more details.

4.4.5 Quantification and statistical analysis

Unless reported otherwise, summary statistics reported as XX ± XX are mean ± SEM.

4.4.5.1 General linear model (GLM)

We applied several pre-processing steps before creating the GLM to explain the data. We first applied a Gaussian spatial filter (FWHM – 100 μm). We then applied a pixelwise high-pass temporal filter (1/128 Hz) to remove low-frequency drift. We finally used grand mean scaling to scale each voxel's intensity to a common scale (Penny et al., 2006; Ashby, 2019). To build the GLM, we convolved the

regressors of interest with a hemodynamic response function (HRF). We used a single gamma function with a time constant (τ) of 1 second, a pure delay (δ) of 1 second, and a phase delay (n) of 3 seconds based upon a previous monkey event-related fMRI study (Kagan et al., 2010). The regressors of interest were fixation period, memory period, movement period, reward delivery, intertrial interval, and regressors for each reward level. For the memory and movement periods, we used separate regressors for contralateral and ipsilateral. For the reward level regressors, we modeled them as lasting the length of the memory period. We then fit the GLM model using the convolved regressors and scaled fUSI data. We used a T-contrast or F-contrast to identify voxels that had a statistically significant difference to the different reward levels.

4.4.5.2 Multiple comparison correction

For all voxel-wise p-values used and reported, we used false-discovery rate correction (FDR) to correct for the simultaneous multiple comparisons. This was implemented using MATLAB's `mafdr` function.

4.4.6 Within-session decoding analysis

Decoding the movement and decision variables on a single trial basis had five steps: 1) aligning the fUSI data and behavioral data, 2) preprocessing, 3) selecting data to analyze, 4) dimensionality reduction and class separation, and 5) cross-validation. First, we created the behavioral labels by temporally aligning the fUS data with the behavioral data. We could then label each fUSI timepoint with its corresponding task state, movement direction, and decision variable states.

Second, we preprocessed the data by applying several operations. The first operation was motion correction. We used NoRMCorre to perform rigid registration between all the Power Doppler images in a session (Pnevmatikakis and Giovannucci, 2017). We then applied temporal detrending (50 timepoints) and a pillbox spatial filter (2-voxel radius) to each Power Doppler image.

Third, we would then select what spatial and temporal portions of the data to use in the decoder model. We always used the entire image where each pixel is a single feature. For the decoding of direction and reward level, we used a dynamic time window. At each timepoint before the cue, we used all timepoints since the start of the trial. For example, to test our ability to decode at 3 seconds after the trial start, we used the fUS images at 0, 1, 2, and 3 seconds. At each timepoint after the cue, we used all previous timepoints after the cue in the trial. For example, to test our ability to decode at 2 seconds after cue onset, we concatenated the data from 0, 1, and 2 seconds after the cue. We treated these

timepoints as additional features in the decoder model. In other words, the input to our decoder model had N*T features, where N is the number of pixels in a single Power Doppler image and T is the number of timepoints.

For the task state decoding, we always used a single timepoint of data. To avoid biases in the learned model, we balanced class labels by randomly taking N samples from each state, where N is the number of samples in the smallest class.

Fourth, we split the data into train and test folds according to a K-fold cross-validation scheme. For the reward magnitude and direction decoding, we used ten folds. For the task state decoding, we used five folds. For the test sets, we stripped the behavioral labels. We then scaled the train and test splits by applying a z-score operation fit to the train data. We used the entire image as our features, i.e., each voxel's activity was a single feature. To train the linear decoder on the training data, we used principal component analysis (PCA) for dimensionality reduction and linear discriminant analysis (LDA) for class separation. For the PCA, we kept 95% of the variance. For the LDA, we used MATLAB's `fitcdiscr` function with default parameters. We then calculated the percent correct for each sample in the test data.

Fifth, we then repeated the model training and testing for each consecutive fold of data. We finally found the mean accuracy metrics across all the folds, i.e., mean accuracy. To correct for testing the performance at every trial timepoint, we used a Bonferroni correction.

We used a 1-sided binomial test to calculate the p-values associated with the percent correct results.

4.4.7 Searchlight analysis

We defined a circular region of interest (ROI) and, using only the pixels within the ROI, we performed the within-session decoding analysis using 10-fold cross-validation. We assigned that ROI's percent correct metrics to the center voxel. We then repeated this across the entire image, such that each image pixel is the center of one ROI. To visualize the results, we overlaid the performance metric (percent correct) onto a vascular map and kept up to the 10% most significant voxels. As part of this searchlight analysis, we ignored activity within the sulcal fold or activity on the other side of the sulcal fold. To do this, we defined the boundaries of the sulcal folds using a custom GUI in MATLAB and only used voxels on the same side of the sulcal fold as the searchlight center. This is similar in principle to the cortical surface-based searchlight decoding developed for fMRI (Chen et al., 2011).

4.5 Extended Data

4.5.1 Supplemental movies

Supplemental Movie 4.1 Example trial averaged activity
Average activity across imaging plane for example session in Monkey P. Time relative to cue onset.

5 Decoding Motor Plans Using a Closed-Loop Ultrasonic Brain-Machine Interface

The following chapter's contents are taken and adapted from Griggs and Norman et al. 2022, with modifications done to fit the dissertation format.

Griggs, WS and Norman, SL et al. 2022. Decoding motor plans using a closed-loop ultrasonic brain-machine interface. bioRxiv. https://doi.org/10.1101/2022.11.10.515371.

5.1 Background

Brain-machine interfaces (BMIs) translate complex brain signals into computer commands and are a promising method to restore the capabilities of human patients with paralysis (Wolpaw et al., 2020). State-of-the-art BMIs have already made this future a reality in limited clinical trials (Hochberg et al., 2006; Collinger et al., 2013; Aflalo et al., 2015; Moses et al., 2021; Willett et al., 2021). However, these BMIs require invasive electrode arrays inserted into the brain. Device degradation limits the BMI's longevity to typically around 5 years (Bullard et al., 2020; Sponheim et al., 2021). The implants only sample from small regions of superficial cortex. These are some of the factors limiting BMI technology's adoption to a broader patient population.

Functional ultrasound (fUS) imaging is a recently developed technique that is poised to enable longer lasting, less invasive BMIs that can scale to sense activity from large regions of the brain. fUS neuroimaging uses ultrafast pulse-echo imaging to sense changes in cerebral blood volume (CBV)(Macé et al., 2011). It has a high sensitivity to slow blood flow (~1mm/s velocity) and balances good spatiotemporal resolution (100 μm; <1 sec) with a large and deep field of view (~2 centimeters). Previously, we demonstrated that fUS neuroimaging possesses the sensitivity and field of view to decode movement intention on a single-trial basis simultaneously for two directions (left/right), two effectors (hand/eye), and task state (go/no-go) (Norman et al., 2021). However, we performed this post hoc (off-line) analysis using pre-recorded data. In this study, we demonstrate the first online, closed-loop, functional ultrasound BMI (fUS-BMI). In addition, we present key advances that build on previous fUS neuroimaging studies. These include decoding eight movement directions and designing decoders stable across more than 40 days.

5.2 Results

We used a miniaturized 15.6-MHz, 128-channel, linear ultrasound transducer array paired with a real-time ultrafast ultrasound acquisition system to stream 2 Hz fUS images from monkeys as they performed memory-guided eye movements (**Figure 5.1**). We positioned the transducer surface normal to the brain above the dura mater and recorded from coronal planes of the left posterior parietal cortex (PPC), a sensorimotor association area that uses multisensory information to guide movements and attention (Colby and Goldberg, 1999; Andersen and Buneo, 2002; Andersen and Cui, 2009). This technique achieved a large field of view (12.8 mm width, 16 mm depth, 400 μm plane thickness) while maintaining high spatial resolution (100 μm x 100 μm in-plane). This allowed us to stream high-resolution hemodynamic changes across multiple PPC regions simultaneously, including the lateral (LIP) and medial (MIP) intraparietal cortex (**Figure 5.1A**). Previous research has shown that the LIP and MIP are involved in planning eye and reach movements, respectively (Gnadt and Andersen, 1988; Snyder et al., 1997, 2000). This makes PPC a good region from which to record effector-specific movement signals.

We streamed the real-time 2 Hz fUS images into a BMI decoder that used principal component (PCA) and linear discriminant analysis (LDA) to predict planned movement directions. We used the BMI output to directly control the behavioral task (**Figure 5.1C**). To build the initial training set for the decoder, each of two monkeys initially performed instructed eye movements to a randomized set of two or eight peripheral targets. We used the fUS activity during the delay period preceding successful eye movements to train the decoder. After 100 successful training trials, we switched to closed-loop BMI mode where the movement came from the fUS-BMI (**Figure 5.1E**). During this closed-loop BMI mode, the monkey continued to fixate on the center cue until after the delivery of the liquid reward. During the interval between a successful trial and the subsequent trial, we rapidly retrained the decoder, continuously updating the decoder model as each monkey used the fUS-BMI.

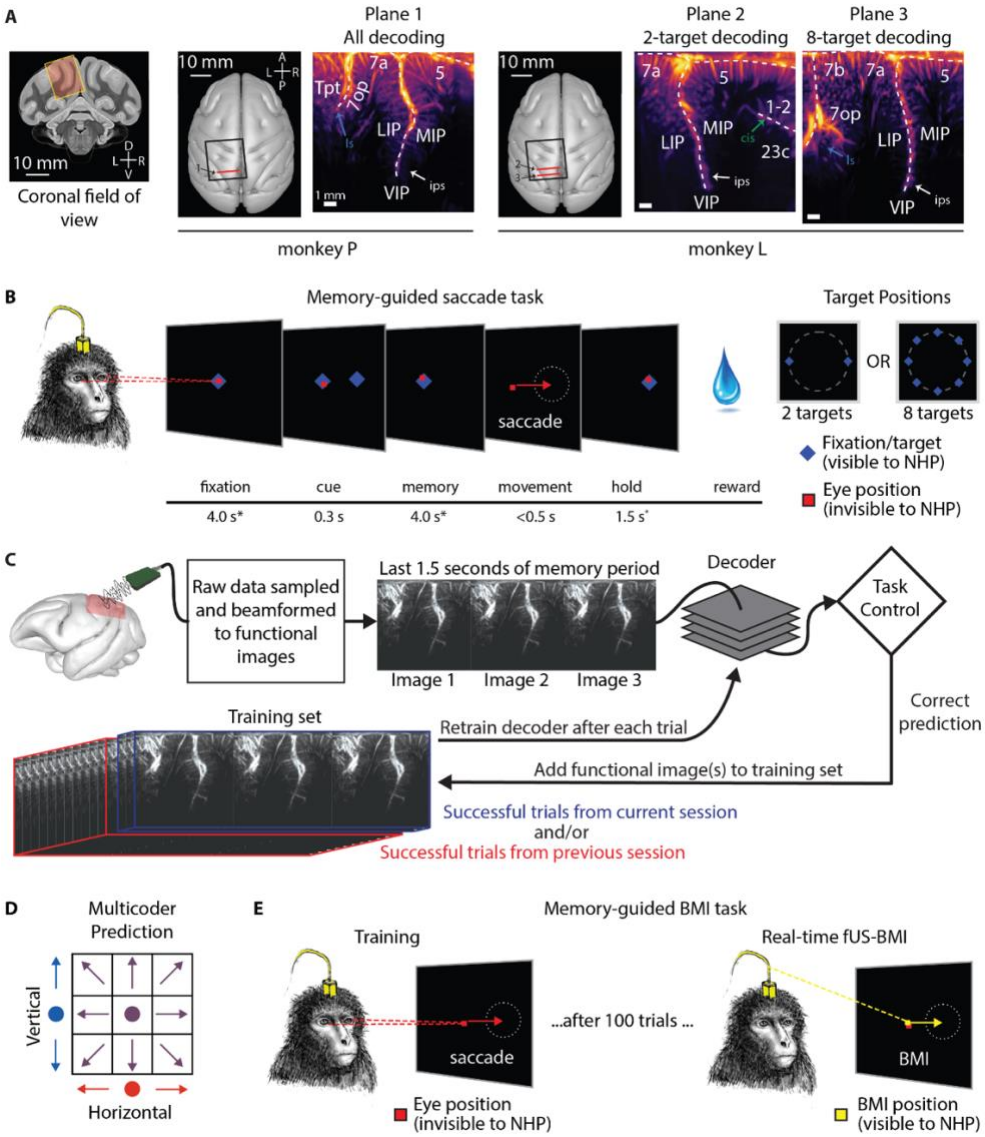

Figure 5.1 Anatomical recording planes and behavioral tasks.
(A) Coronal fUS imaging planes used for monkey P and monkey L. A coronal slice from an MRI atlas shows the approximate field of view for the fUS imaging plane. Black square - Recording chamber. Red line – Position of ultrasound transducer. The vascular maps show the mean Power Doppler image from a single imaging session. Anatomical labels based upon (Saleem, 2012). (B) Memory-guided saccade task. monkey – Nonhuman primate, i.e., monkey. (C) fUS-BMI algorithm. Real-time 2 Hz functional images were streamed to a linear decoder that controlled the behavioral task. The decoder used the last 3 fUS images (1.5 seconds) of the memory period to make its prediction. If the prediction was correct, the data from that prediction was added to the training set. The decoder was retrained after every successful trial. The training set consisted of trials from the current session and/or from a previous fUS-BMI session. (D) Multicoder algorithm. For predicting eight movement directions, the vertical component (blue; up, middle, or down) and the horizontal component (red; left, middle, or right) were separately predicted and then combined to form each fUS-BMI prediction (purple). (E) Memory-guided BMI task. The BMI task is the same as (B) except that the movement period is controlled by the brain activity (via fUS-BMI) rather than eye movements. After 100 successful eye-movement trials, the fUS-BMI controlled the movement prediction (closed-loop control). During the closed-loop mode, the monkey had to maintain fixation on the center fixation cue until reward delivery. The red square represents the monkey's eye position and is not visible to the monkey. Yellow square represents the BMI-controlled cursor position and is visible to the monkey.

5.2.1 Online decoding of two eye movement directions

To demonstrate the feasibility of a fUS-BMI, we first performed online, closed-loop decoding of two movement directions (**Figure 5.2**). After building a preliminary training set of 20 trials, we began testing the decoder's accuracy on each new trial in a training mode not visible to the monkey (blue line, **Figure 5.2A**). After 100 trials, we switched the BMI from training to closed-loop decoding where the monkey now controlled the task direction using his movement intention, i.e., the brain activity detected by the fUS-BMI in the last 3 fUS images of the memory period (**Figure 5.1C**, **E**, **Figure 5.2A**-yellow line). At the conclusion of each trial, the monkey received visual feedback of the fUS-BMI prediction. In our second closed-loop 2-direction session, the decoder reached significant accuracy ($p<0.01$; 1-sided binomial test) after 55 training trials and improved in accuracy until peaking at 82% accuracy at trial 114 (**Figure 5.2A**). The decoder predicted both directions well above chance level but displayed better performance for rightward movements (**Figure 5.2B**). To understand which brain regions were most important for the decoder performance, we performed a searchlight analysis with a 200 μm, i.e., 2 voxel, radius (**Figure 5.2C**). Dorsal LIP and Area 7a contained the voxels most informative for decoding intended movement direction.

An ideal BMI needs very little training data and no retraining between sessions. Electrode-based BMIs typically require calibration or re-training for each subsequent session, due to difficulty in recording from the same neurons across multiple days (Downey et al., 2018).Thanks to its wide field of view, fUS neuroimaging can image from the same brain regions over time, and therefore may be an ideal technique for stable decoding across many sessions. To test this hypothesis, we pretrained the fUS-BMI using a previously recorded session's data and then tested the decoder in an online, closed-loop experiment. To perform this pretraining, we first aligned the data from the previous session's imaging plane to the current session's imaging plane (**Supplemental Figure 5.1**). We used semi-automated rigid body registration to find the transform between the previous and current imaging plane, applied this 2D image transform to each frame of the previous session, and saved the aligned data. This semi-automated pre-registration process took less than 1 minute. To pretrain the model, the fUS-BMI automatically loaded this aligned dataset and trained the initial decoder. The fUS-BMI reached significant performance substantially faster (**Figure 5.2D**) when we used this pretraining approach. The fUS-BMI achieved significant accuracy at Trial 7, approximately 15 minutes faster than the example session without pretraining.

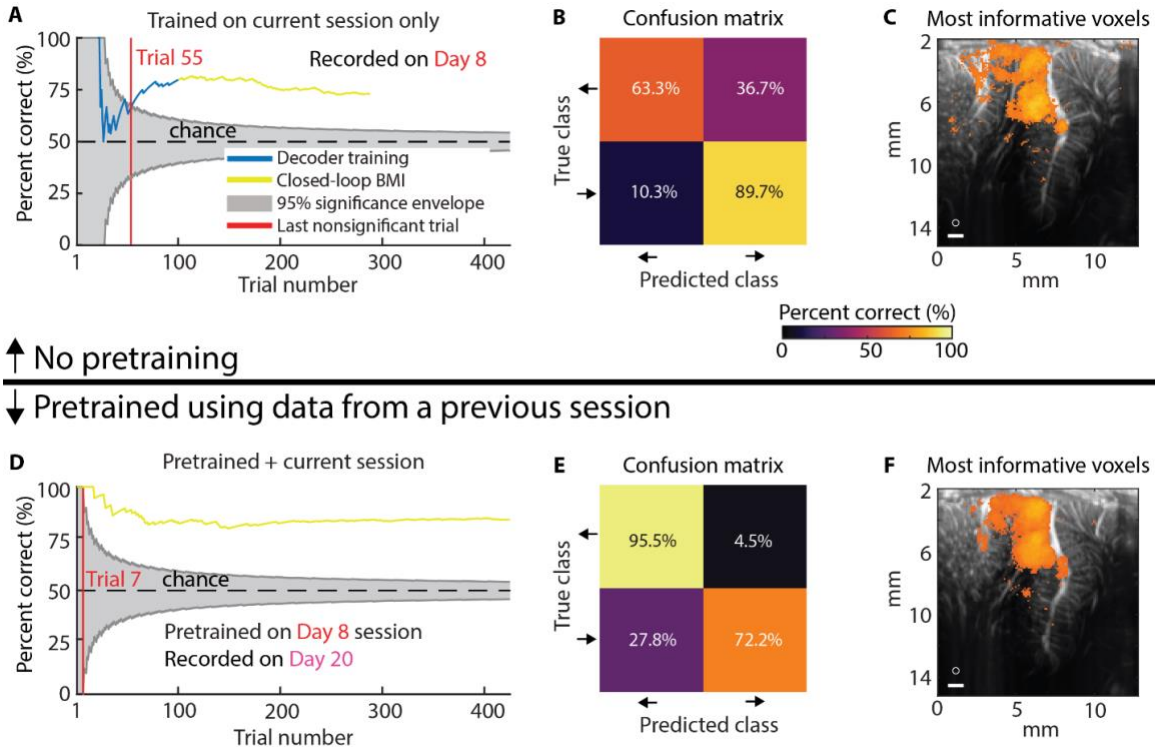

Figure 5.2 Example sessions decoding two saccade directions.
(A) Mean decoding accuracy as a function of trial number. Blue represents fUS-BMI training where the monkey controlled the task using overt eye movements. The BMI performance shown in blue was generated post hoc with no impact on the real-time behavior. Yellow represents trials under fUS-BMI control where the monkey maintained fixation on the center cue and the task direction was controlled by the fUS-BMI. Grey chance envelope – 95% binomial distribution. Red line – last nonsignificant trial. (B) Confusion matrix of decoding accuracy across entire session represented as percentage (rows add to 100%). (C) Searchlight analysis represents the 10% voxels with the highest decoding accuracy (threshold is q<=1.66e-6). White circle – 200 μm radius searchlight used. White bar – 1 mm scale bar. (D-F) Same format as in (A-C). fUS-BMI was pretrained using data collected from a previous session. Top 10% of voxels in searchlight analysis corresponds to a threshold of q<=2.07e-13. Text color for the day labels matches the day label colors in **Figure 5.3**.

To quantify the benefits of pretraining upon fUS-BMI training time and performance, we compared fUS-BMI performance across all sessions when (a) using only data from the current session versus (b) pretraining with data from a previous session (**Figure 5.3**). For all real-time sessions that used pretraining, we also created a post hoc (offline) simulation of the fUS-BMI results without using pretraining. For each simulated session, we passed the recorded data through the same classification algorithm used for the real-time fUS-BMI but did not use any data from a previous session.

Using only data from the current session: The mean decoding accuracy reached significance ($p<0.01$; 1-sided binomial test) at the end of each online, closed-loop recording session (2/2 sessions monkey P, 1/1 session monkey L) and most offline, simulated recording sessions (3/3 sessions monkey P, 3/4

sessions monkey L) (**Figure 5.3**). For monkey P, decoder accuracies reached 75.43 ± 2.56% correct (mean ± SEM) and took 40.20 ± 2.76 trials to reach significance. For monkey L, decoder accuracies reached 62.30 ± 2.32% correct and took 103.40 ± 23.63 trials to reach significance.

Pretraining with data from a previous session: The mean decoding accuracy reached significance at the end of each online, closed-loop recording session (3/3 sessions monkey P, 4/4 sessions monkey L) (**Figure 5.2C**). Using previous data reduced the time to achieve significant performance (100% of sessions reached significance sooner, monkey P – 36-43 trials faster; monkey L – 15-118 trials faster). The performance at the end of the session was not statistically different from performance in the same sessions without pretraining (paired t-test, $p<0.05$). For monkey P, accuracies reached 80.21 ± 5.61% correct and took 9.00 ± 1 trials to reach significance. For monkey L, accuracies reached 66.78 ± 2.79% correct and took 71.00 ± 28.93 trials to reach significance. Assuming no missed trials, pre-training decoders shortened training by 10-45 minutes. We also simulated the effects of not using any training data from the current session, i.e., using only the pretrained model (**Supplemental Figure 5.2A**). We did not observe a statistically significant difference between the performance (accuracy or number of trials to significant performance) for either monkey whether current session training data was included or not.

These results demonstrate online decoding of fUS signals into two directions of movement intention, monkeys learning to control the task using the fUS-BMI, and that pretraining using a previous session's data greatly reduced, or even eliminated, the amount of new training data required in a new session.

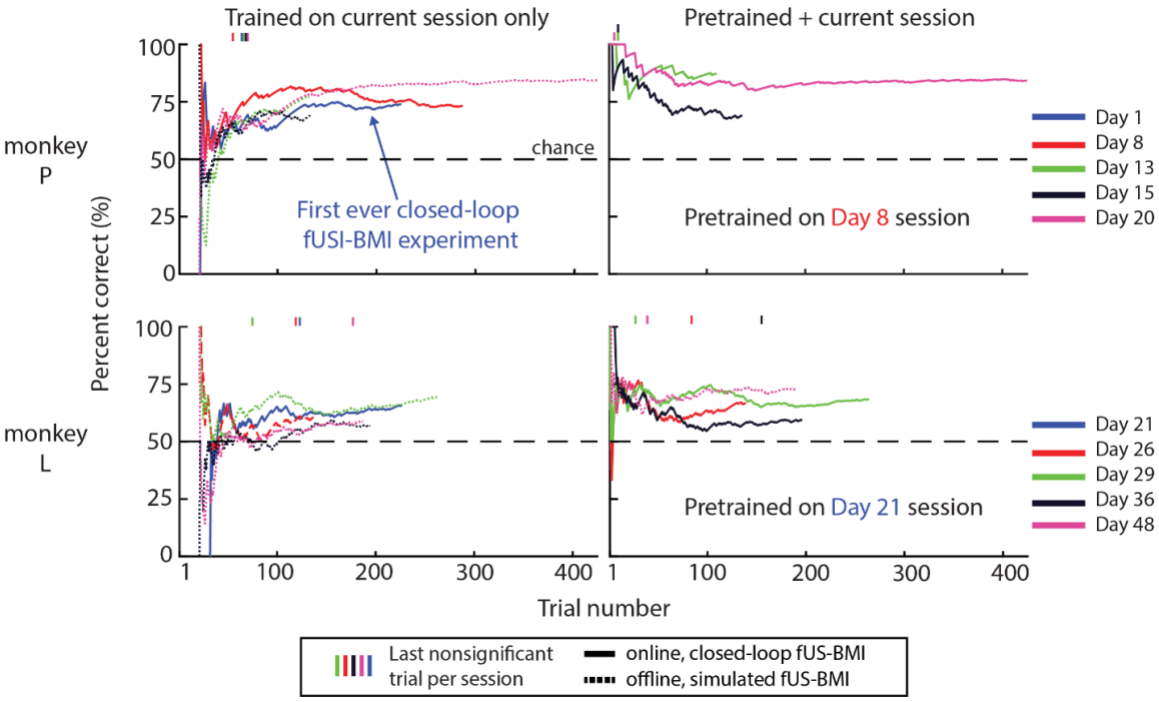

Figure 5.3 Performance across sessions for decoding two saccade directions.
Mean decoder accuracy during each session for monkey P and L. Solid lines are real-time results while fine-dashed lines are simulated sessions from post hoc analysis of real-time fUS imaging data. Vertical marks above each plot represent the last nonsignificant trial for each session. Day number is relative to the first fUS-BMI experiment. Coarse-dashed horizontal black line represents chance performance.

5.2.2 Online decoding of eight eye movement directions

Having demonstrated that we could achieve similar, but online and closed-loop, performance to our previous offline decoding paper(Norman et al., 2021), we extended the capabilities of fUS-BMI by decoding eight movement directions in real time (**Figure 5.4**). We used a "multicoder" architecture where we predicted the vertical (up, middle, or down) and horizontal (left, middle, or right) components of intended movement separately and then combined those independent predictions to form a final prediction (e.g., up and to the right) (**Figure 5.1D**). In the first 8-direction experiment, the decoder reached significant accuracy ($p<0.01$; 1-sided binomial test) after 86 training trials and improved until plateauing at 34-37% accuracy (**Figure 5.4A** – upper plot), compared to 12.5% chance level, with most errors indicating directions neighboring the cued direction (**Figure 5.4B**). To capture this extra information about proximity of each prediction to the true direction, we examined the mean absolute angular error. The fUS-BMI reached significance at 55 trials and steadily decreased its mean absolute angular error to 45° by the end of the session (**Figure 5.4A** – bottom plot). Compared to the

most informative voxels for the 2-target eye decoder, a larger portion of LIP, including ventral LIP, contained the most informative voxels for decoding eight directions of movement (**Figure 5.4C**).

We next tested whether pretraining would aid the 8-target decoding similarly to the 2-target decoding. As before, pretraining improved the number of trials required to reach significant decoding (**Figure 5.4D**). The fUS-BMI reached significant accuracy at Trial 13, approximately 25 minutes earlier than using only data from the current session. The mean decoder accuracy reached 45% correct with a final mean absolute angular error of 34°, which was better than the performance achieved in the example session without pretraining. The searchlight analysis indicated the same regions within LIP provided the most informative voxels for decoding (**Figure 5.4F**) for both the example sessions with and without pretraining. Notably, we pretrained the fUS-BMI on data from 42 days before the current session. This demonstrates that fUS-BMI can remain stable over at least 42 days. It further demonstrates that we can consistently locate the same imaging plane and that mesoscopic PPC populations consistently encode for the same directions on the time span of >1 month.

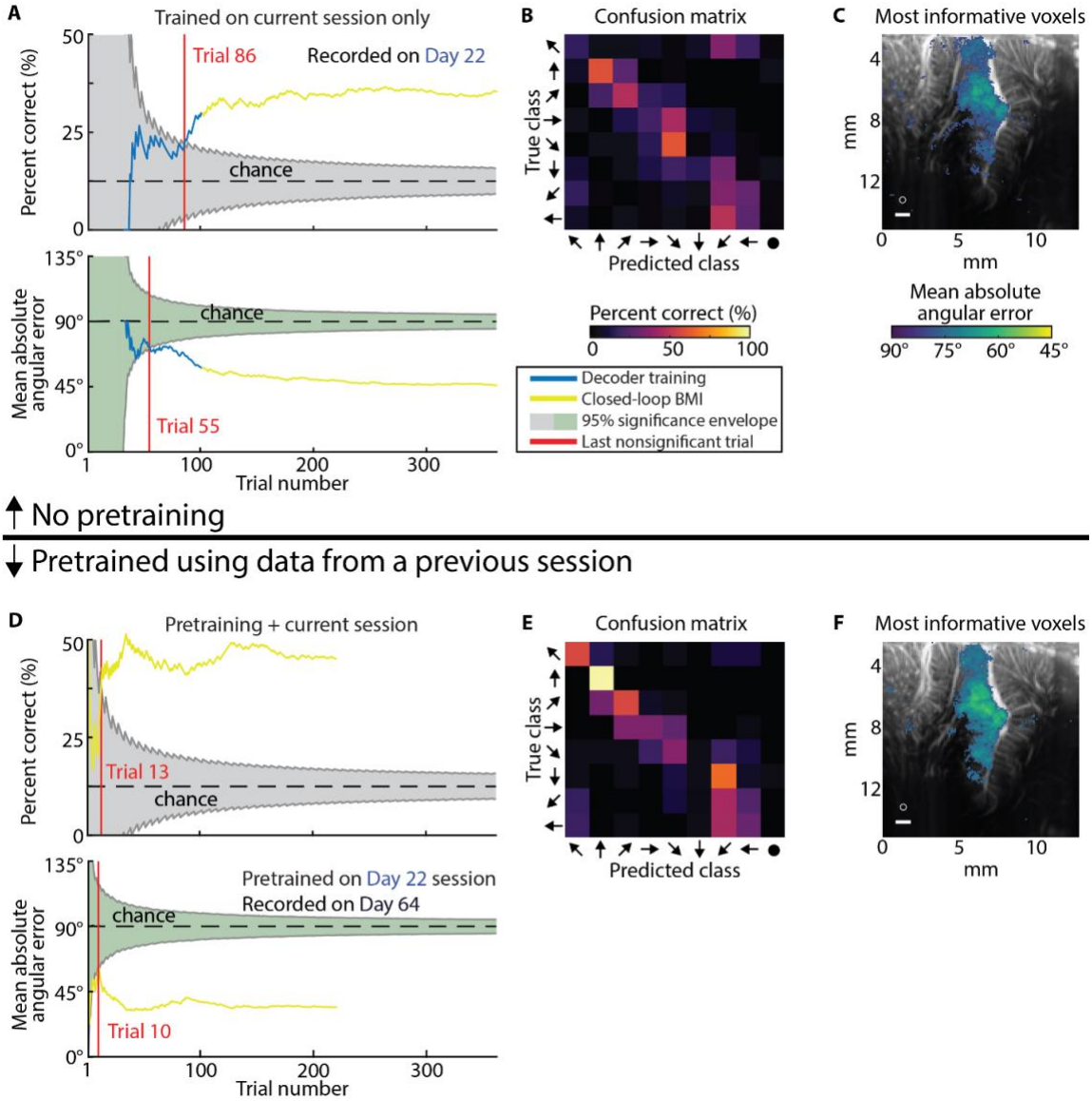

Figure 5.4 Example sessions decoding eight saccade directions.
(A) Mean decoding accuracy and mean absolute angular error as a function of trial number. Blue represents fUS-BMI training where the monkey controlled the task using overt eye movements. The BMI performance shown here was generated post hoc tested on each new trial with no impact on the real-time behavior. Yellow represents trials under fUS-BMI control where the monkey maintained fixation on the center cue and the movement task direction was controlled by the fUS-BMI. Grey chance envelope – 95% binomial distribution. Green chance envelope – 95% permutation test distribution. Red line – last nonsignificant trial. (B) Confusion matrix of decoding accuracy across entire session represented as percentage (rows add to 100%). The horizontal axis plots the predicted movement (predicted class) and the vertical axis the matching directional cue (true class). (C) Searchlight analysis represents the 10% of voxels with the lowest mean absolute angular error (threshold is q≤2.98e-3). White circle – 200 μm searchlight radius used. White bar – 1 mm scale bar. (D-F) Same format as in (A-C). fUS-BMI was pretrained on data from Day 22 and updated after each successful trial. Top 10% of voxels in searchlight analysis corresponds to a threshold of q≤8e-5. Text color for the day labels matches the day label colors in **Figure 5.5**.

Using only data from the current session (**Figure 5.5**-left): The mean decoder accuracy reached significance by the end of all real-time (2/2) and simulated sessions (8/8). The mean absolute angular error for monkey P reached 45.26 ± 3.44° and the fUS-BMI took 30.75 ± 12.11 trials to reach significance. The mean absolute angular error for monkey L reached 75.06 ± 1.15° and the fUS-BMI took 132.33 ± 20.33 trials to reach significance.

Pretraining with data from a previous session (**Figure 5.5**-right): The mean decoder accuracy reached significance by the end of all real-time (6/6) and simulated sessions (2/2). The fUS-BMI reached significant decoding earlier for most sessions compared to simulated post hoc data; 5/5 faster monkey L; 2/3 faster monkey P (third session reached significance equally fast). For monkey P, the pretrained decoders reached significance 0-51 trials faster and for monkey L, the pretrained decoders reached significance 66-132 trials faster. For most sessions, this would shorten training by up to 45 minutes. The performance at the end of each session was not statistically different from performance in the same session without pretraining (paired t-test, $p<0.05$). The mean absolute angular error for monkey P reached 37.82° ± 2.86° and the fUS-BMI took 10.67 ± 1.76 trials to reach significance. The mean absolute angular error for monkey L reached 71.04° ± 2.29° and the fUS-BMI took 42.80 ± 17.05 trials to reach significance. We also simulated the effects of not using any training data from the current session, i.e., using only the pretrained model (**Supplemental Figure 5.2B**). We did not observe a statistically significant difference between the performance (accuracy, mean absolute angular error, or number of trials to significant performance) for either monkey whether current session training data was included or not.

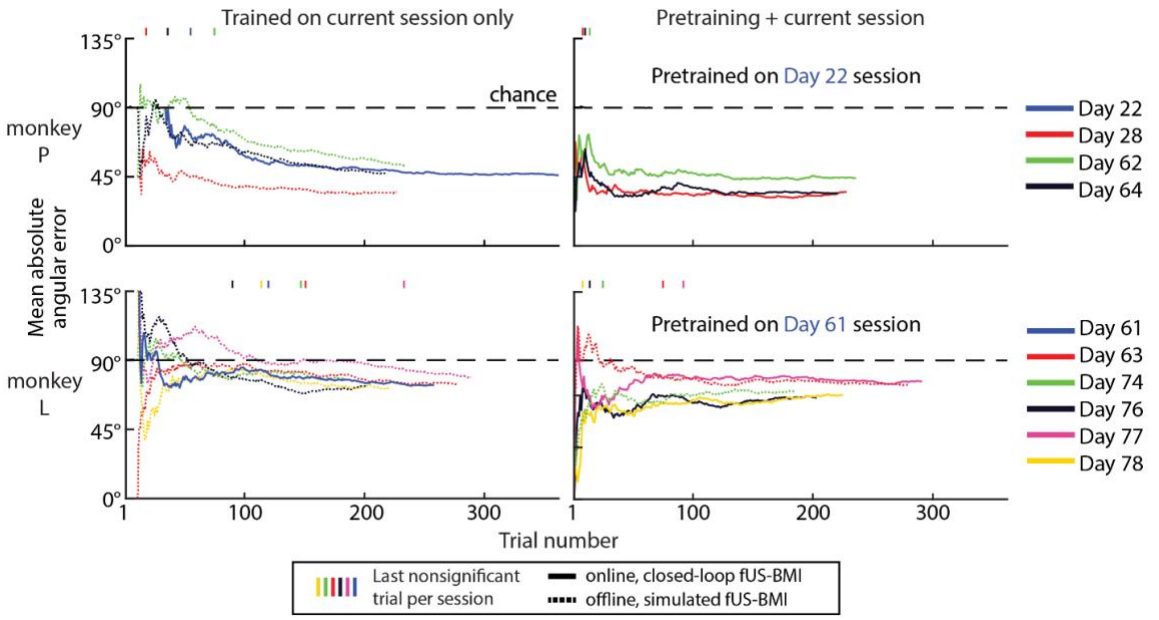

Figure 5.5 Performance across sessions for decoding eight saccade directions.
Mean absolute angular error during each session for monkey P and L. Solid lines are real-time results while fine-dashed lines are simulated sessions from post hoc analyses of real-time fUS data. Vertical marks represent the last nonsignificant trial for each session. Day number is relative to the first fUS-BMI experiment. Coarse-dashed horizontal black line—chance performance.

These results demonstrate online decoding of fUS signals into eight directions of movement intention, a significant advance over decoding only contra- and ipsilateral movements. They also show that the directional encoding within PPC mesoscopic populations is stable across at least one month, thus allowing us to reduce, or even eliminate, the need for new training data.

5.2.3 Online decoding of two hand movement directions

Another strength of fUS neuroimaging is its wide field of view capable of sensing activity from multiple functionally diverse brain regions, including those that encode different movement effectors, e.g., hand and eye. To test this, we decoded intended hand movements to two target directions (reaches to the Left/Right for monkey P) in addition to our previous results decoding eye movements (**Figure 5.6**). The monkey performed a similar task wherein he had to maintain touch on a center dot and touch the peripheral targets during the training (**Figure 5.6A**). In this scenario, we no longer constrained the monkey's eye position, instead recording hand movements to train the fUS-BMI. After the training period, the monkey controlled the task using the fUS-BMI while keeping his hand on the center fixation cue. Notably, we used the same imaging plane used for eye movement decoding, which contained both LIP (important for eye movements) and MIP (important for reach movements).

In an example session using only data from the current session (**Figure 5.6B**), it took 70 trials to reach significance and achieved a mean decoder accuracy of 61.3%. The decoder predominately guessed left (**Figure 5.6C**). Two foci within the dorsal LIP and scattered voxels throughout Area 7a and the temporo-parietal junction (Area Tpt) contained the most informative voxels for decoding the two movement directions (**Figure 5.6D**).

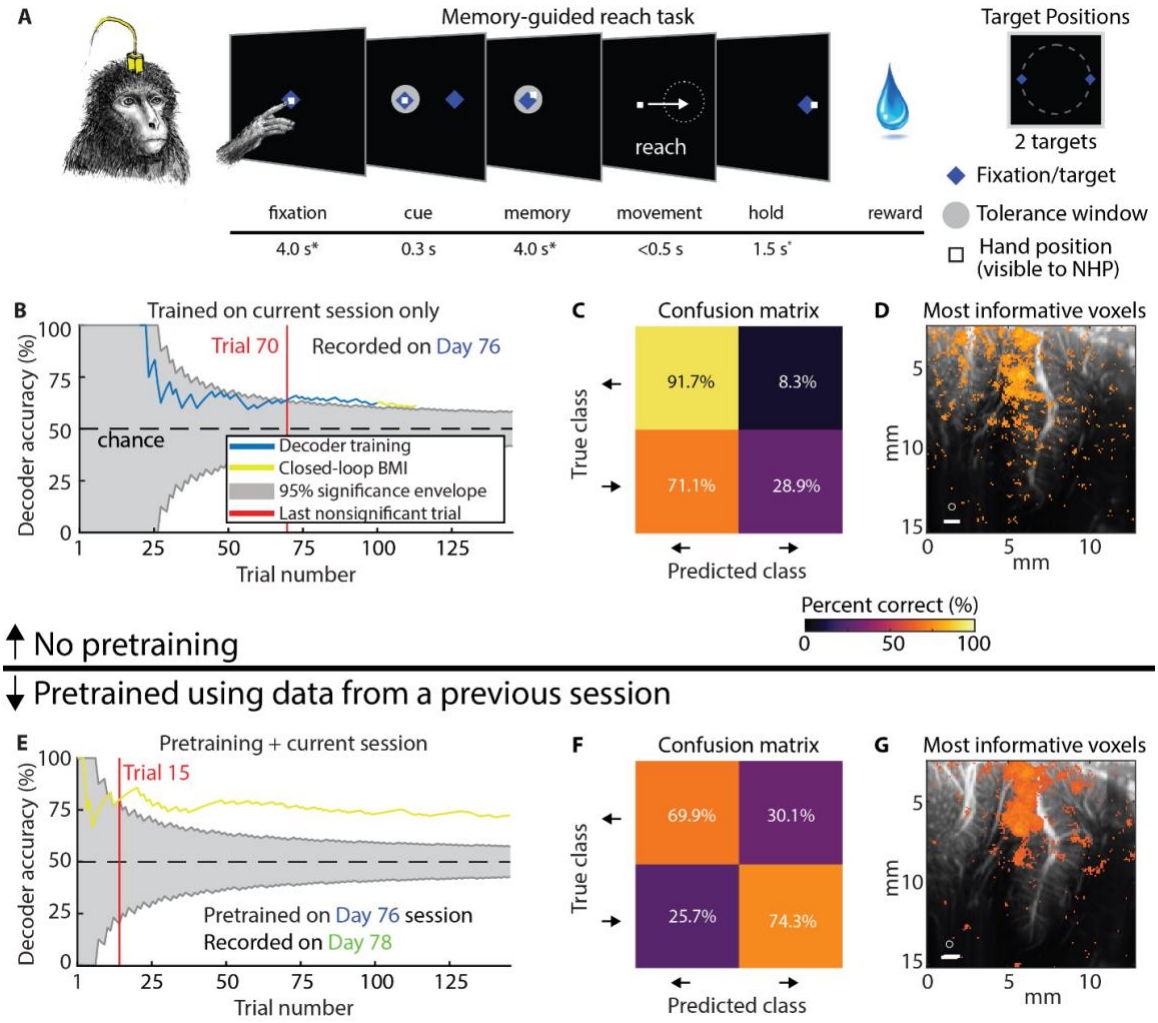

Figure 5.6 Example sessions decoding two reach directions.
(A) Memory-guided reach task for Monkey P. Identical to memory-guided saccade task in **Figure 5.1**B with all fixation or eye movements being replaced by maintaining touch on the screen and reach movements, respectively. Peripheral cue was chosen from one of two peripheral targets. The white square represents the monkey's hand position and is visible to the monkey. (B-D) Example results from session trained on data from the current session only. Same format as **Figure 5.2**A-C. Threshold for searchlight analysis is q≤3.05e-3. (E-G) Example results from the Day 78 session pretrained on data from Day 76 and retrained after each successful trial. Same format as **Figure 5.2**D-F. Threshold for searchlight analysis is q≤6.47e-3. Text color for the day labels matches the day label colors in **Figure 5.7**.

To assess the benefits of pretraining on reach decoder performance and training time, we evaluated the effect of pretraining the fUS-BMI on an example session (**Figure 5.6E-G**). As with the saccade decoders, pretraining significantly shortened training time. In some cases, pretraining rescued a "bad" model. For example, the example session using only current data (**Figure 5.6C**) displayed a heavy bias towards the left. When we used this same example session to pretrain the fUS-BMI a few days later, the new model made balanced predictions (**Figure 5.6F**). The searchlight analysis for this example session revealed that the same dorsal LIP region from the example session without pretraining contained the majority of the most informative voxels (**Figure 5.6G**). MIP and Area 5 also contained a few patches of highly informative voxels.

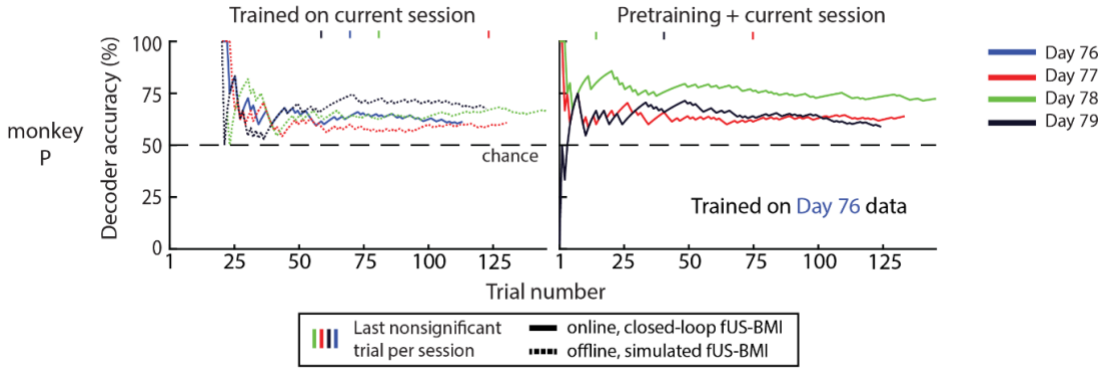

Figure 5.7 Performance across sessions for decoding two reach directions.
Performance across sessions for monkey P. Same format as **Figure 5.3**A.

Using only data from the current session (**Figure 5.7**-left): The mean decoder accuracy reached significance by the end of each session (1 real-time and 3 simulated). The performance reached 65 ± 2% correct and took 67.67 ± 18.77 trials to reach significance.

Pretraining with data from a previous session (**Figure 5.7**-right): The mean decoder accuracy reached significance by the end of each session (3 real-time). Monkey P's performance reached 65 ± 4% correct and took 43.67 ± 17.37 trials to reach significance. For two of the three real-time sessions, the number of trials needed to reach significance decreased with pretraining (-2 – 46 trials faster; 0-16 minutes faster). There was no statistical difference in performance between the sessions with and without pretraining (paired t-test, $p<0.05$). We also simulated the effects of not using any training data from the current session, i.e., using only the pretrained model (**Supplemental Figure 5.2C**). We did not observe a statistically significant difference between the performance (accuracy or number of trials to significant performance) whether current session training data was included or not.

These results are consistent with our previous study's results (Norman et al., 2021) that we can decode not only eye movements, but also reach movements. As with the eye movement decoders, we could pretrain the fUS-BMI using a previous session's data and reduce, or even eliminate, the need for new training data.

5.3 Discussion

This work demonstrates, for the first time, a closed-loop, online, ultrasonic BMI and makes two other key advances that prepare for future work on the next generation of minimally-invasive ultrasonic BMIs: decoding more movement directions and stabilizing decoders across more than a month.

5.3.1 Decoding more movement directions

We successfully decoded eight movement directions in real-time, an advance on previous work that decoded two saccade directions and two reach directions using pre-recorded data (Norman et al., 2021). Specifically, we replicated the two direction results using real-time online data (**Figure 5.2**,**Figure** 5.3,**Figure** 5.6) and then extended the decoder to work for eight movement directions (**Figure 5.4Figure 5.5**).

5.3.2 Stabilizing decoder across time

Electrode-based BMIs are particularly adept at sensing fast changing (~10s of ms) neural activity from spatially localized regions (<1 cm) during behavior or stimulation that is correlated to activity in such spatially specific regions, e.g., M1 for motor and V1 for vision. Electrodes, struggle to track individual neurons over longer periods of time, e.g., between subsequent recording sessions. Consequently, decoders are typically retrained every day (Downey et al., 2018). In this paper, we demonstrated a novel alignment method that stabilizes image-based BMIs across more than a month and decode from the same neural populations with minimal, if any, retraining. This is a critical development that enables easy alignment of previous days' models to a new day's data and begin decoding while acquiring minimal to no new training data. Much effort has focused on reducing or eliminating re-training in electrode-based BMIs (Sussillo et al., 2016; Dyer et al., 2017; Kao et al., 2017b; Pandarinath et al., 2018; Degenhart et al., 2020; Wimalasena et al., 2020). These methods require identification of manifolds and/or latent dynamical parameters and collecting new data to align to these manifolds/parameters. Furthermore, some of the algorithms are computationally expensive and/or difficult to implement in online use. Our novel decoder alignment algorithm leverages the intrinsic spatial resolution and field of view provided by fUS neuroimaging to simplify this process in a way that is intuitive, repeatable, and performant.

5.3.3 Improving performance

An ideal fUS-BMI would have performance that is better than the 45% correct at decoding eight movement directions found in this study. We have several ideas about how to improve the fUS-BMI performance.

First, realigning the recording chamber and ultrasound transducer along the intraparietal sulcus axis would allow sampling from a larger portion of LIP and MIP. In this paper, we placed the chamber and probe in a coronal orientation to aid anatomical interpretability. However, most of our imaging plane is not contributing to the decoder performance (**Figure 5.2C**, **Figure 5.3F**, **Figure 5.4C**, **Figure 5.4F**, **Figure 5.6D**, **Figure 5.6G**). Previous papers have found that receptive fields are anatomically organized along anterior-posterior and dorsal-ventral gradients within LIP (Patel et al., 2014). By realigning the recording chamber orthogonal to the intraparietal sulcus in future studies, we could sample from a larger anterior-posterior portion of LIP with diverse range of directional tunings.

Second, we were limited to 2D planar imaging. The advent of 3D ultrafast volumetric imaging based on matrix or row-column array technologies will be capable of sensing changes in CBV from blood vessels that are currently orthogonal to the imaging plane. Additionally, 3D volumetric imaging can fully capture entire functional regions and sense multiple functional regions simultaneously. There are many regions which could fit inside a single 3D probe's field of view and contribute to a motor BMI, for example: PPC, primary motor cortex (M1), dorsal premotor cortex (PMd), and supplementary motor area (SMA). These areas encode different aspects of movements including goals, sequences, and expected value of actions (Platt and Glimcher, 1999; Taylor et al., 2002; Ohbayashi et al., 2016; Côté et al., 2020). This is just one example of myriad advanced BMI decoding strategies that will be made possible by synchronous data across brain regions. Currently, high-quality, low-latency real-time 3D fUS imaging is not possible due to bandwidth, memory, and compute limitations. However, ongoing advances in hardware and algorithms will likely soon enable 3D fUS-BMI.

Third, another route for improved performance would be using more advanced decoder models. Convolutional neural networks are tailor-made for identifying image characteristics and are robust to spatial perturbation common in fUS images. Recurrent neural networks and transformers use "memory" processes that may be particularly adept at characterizing the temporal structure of fUS time series data. A potential downside of artificial neural networks (ANNs) like these is that they require significantly more training data. However, the methods presented here for across-session

image alignment allow for pre-recorded data to be aggregated and organized into a large data corpus. Such a data corpus should be sufficient for training many ANNs. The amount of training data required could be further reduced by decreasing the feature count of the ANNs themselves. For example, one could reduce the input layer dimensions by restricting the data to features collected only from the task-relevant areas, such as LIP and MIP, instead of the entire image. ANNs additionally take longer to train (~minutes instead of seconds) and would require different strategies for online retraining than used in this paper. In this paper, we leveraged the ability to rapidly retrain linear models on every trial without stopping the task. Although online training and inference using ANNs are beyond the scope of this paper, this is an active area of investigation for fUS-BMIs. For example, an ANN has recently been used to offline decode different movement and sleep states using rodent fUSI data (Berthon et al., 2023).

5.3.4 Advantages of fUS neuroimaging

fUS neuroimaging has several advantages compared to existing BMI technologies. The large and deep field of view allows us to reliably record from multiple cortical and subcortical regions simultaneously – and to record from the same populations in a stable manner over long periods of time. fUS neuroimaging is epidural, i.e., does not require penetration of the dura mater, substantially decreasing surgical risk, infection risk, and tissue reactions while enabling chronic imaging over long periods of time (potentially many years) with minimal, if any degradation, in signal quality. In our monkey studies, fUS neuroimaging has been able to image through the dura, including the granulation tissue that forms above the dura (several ~mm) with minimal loss in sensitivity.

In this paper, we demonstrated a new benefit of fUS: decoders that are stable across multiple days or even months. Using conventional image registration methods, we can align our decoder across different recording sessions and achieve excellent performance without collecting additional training data. A weakness of this current fUS-BMI compared to current electrophysiology BMIs is poorer temporal resolution. Electrophysiological BMIs have temporal resolutions in the 10s of milliseconds (e.g., binned spike counts). fUS can reach a similar temporal resolution (up to 500 Hz in this work) but is limited by the time constant of mesoscopic neurovascular coupling (~seconds). Despite this neurovascular response acting as a low pass filter on each voxel's signal, faster fUS acquisition rates can measure temporal variation across voxels down to <100 ms resolution. Earlier researchers already exploited this to track dynamic propagation of local hemodynamic changes through cortical layers and between functional regions within a single plane of view in monkeys (Dizeux et al., 2019). As

the temporal resolution and latency of real-time fUS imaging improves with enhanced hardware and software, tracking the propagation of these rapid hemodynamic signals may enable improved BMI performance and response time. Additionally, for the current study, and for many BMI applications, the goals of an action can be extracted despite the slow mesoscopic hemodynamic response and do not require the short latency required for extracting faster signals such as the trajectories of intended movements. Beyond movement, many other signals in the brain may be better suited to the spatial and temporal strengths of fUS, for example, monitoring biomarkers of neuropsychiatric disorders (discussed in detail below).

5.3.5 Decoding hand, eye, or both?

Dorsal and ventral LIP contained the most informative voxels when decoding eye movements (**Figure 5.2C**, **F**, **Figure 5.4C**, **F**). This is consistent with previous literature that LIP is important for spatially specific oculomotor intention and attention (Gnadt and Andersen, 1988; Barash et al., 1991 p.199; Colby et al., 1995). Dorsal LIP, MIP, Area 5, and Area 7 contained the most informative voxels during reach movements (**Figure 5.6D, G**). The voxels within the LIP closely match with the most informative voxels from the 2-direction saccade decoding, suggesting that our fUS-BMI may be using eye movement plans to build its model of movement direction. The patches of highly informative voxels within MIP and Area 5 suggest the fUS-BMI may also be using reach-specific information (Lacquaniti et al., 1995; Snyder et al., 1997; Chang et al., 2009; Li and Cui, 2013; Mackenzie et al., 2016 p.20). Future experiments will be critical for disentangling the mesoscopic contributions of LIP, MIP, Area 5, and other PPC regions for accurate effector predictions with a fUS-BMI. One such experiment would be recording and ultimately decoding fUS signals from the PPC as monkeys perform dissociated eye and reach movements (Snyder et al., 1997). As this fUS-BMI is translated into human applications, these effector-specific signals can also be more cleanly studied by instructing subjects to perform dissociated effector tasks.

5.3.6 Moving beyond a motor BMI

The vast majority of BMIs have focused on motor applications, e.g. restoring lost motor function in people with paralysis (Wolpaw et al., 2020). Recently there has been interest in developing closed-loop BMIs to restore function to other demographics, such as patients disabled from neuropsychiatric disorders (Shanechi, 2019). Depression, the most common neuropsychiatric disorder, affects an estimated 3.8% of people (280 million) worldwide (Institute of Health Metrics and Evaluation, 2019). In this paper, we demonstrated the utility of the fUS-BMI for motor applications to allow easier

comparison with existing BMI technologies. fUS-BMIs seem to be an ideal platform for applications that require monitoring neural activity over large regions of the brain and long timescales, from hours to months. As demonstrated here, fUS neuroimaging captures neurovascular changes on the order of a second and is also stable over more than 1 month. Combined with neuromodulation techniques such as focused ultrasound, it may be possible to not only record from these distributed corticolimbic populations but also precisely modulate specific mesoscopic populations (Darmani et al., 2022; Singh et al., 2022).

The contributions presented here demonstrate the first online, closed-loop fUS-BMI. It prepares for the next generation of BMIs that are less invasive, high-resolution, stable across time, and scalable to sense activity from large regions of the brain. These advances are a step toward fUS-BMI for a broader range of applications, including restoring function to patients suffering from debilitating neuropsychiatric disorders.

5.4 Materials and Methods

5.4.1 Experimental model and subject details

We implanted two healthy 14-year-old male rhesus macaque monkeys (Macaca mulatta) weighing 14-17 kg. All training, recording, surgical, and animal care procedures were approved by the California Institute of Technology Institutional Animal Care and Use Committee and complied with the Public Health Service Policy on the Humane Care and Use of Laboratory Animals.

5.4.2 General

We used NeuroScan Live software (ART INSERM U1273 & Iconeus, Paris, France) interfaced with MATLAB 2019b (MathWorks, Natick, MA, USA) for the real-time fUS-BMI and MATLAB 2021a for all other analyses.

5.4.3 Animal preparation and implant

For each monkey, we placed a cranial implant containing a titanium head post and a craniotomy positioned over the posterior parietal cortex. The dura underneath the craniotomy was left intact. The craniotomy was covered by a 24 X 24 mm (inner dimension) chamber. For each recording session, we used a custom 3D-printed polyetherimide slotted chamber plug that held the ultrasound transducer. This allowed the same anatomical planes to be consistently acquired on different days.

5.4.4 Behavioral setup

Monkeys sat in a primate chair facing a monitor or touchscreen. The LCD monitor was positioned ~30 cm in front of the monkey. The touchscreen was positioned on each day so that the monkey could reach all the targets on the screen with his fingers but could not rest his palm on the screen. This was ~20 cm in front of the monkey. Eye position was tracked at 500 Hz using an infrared eye tracker (EyeLink 1000, Ottawa, Canada). Touch was tracked using a touchscreen (Elo IntelliTouch, Milpitas, California). Visual stimuli were presented using custom Python 2.7 software based on PsychoPy (Peirce, 2007). Eye and hand position was recorded simultaneously with the stimulus and timing information and stored for offline analysis.

5.4.5 Behavioral tasks

Monkeys performed several different memory-guided movement tasks. In the memory-guided saccade task, monkeys fixated on a center cue for 5 ± 1 seconds. A peripheral cue appeared for 400 ms in a peripheral location (either chosen from 2 or 8 possible target locations) at 20° eccentricity. The monkey kept fixation on the center cue through a memory period (5 ± 1 s) where the peripheral

cue was not visible. The monkey then executed a saccade to the remembered location once the fixation cue was extinguished. If the monkey's eye position was within a 7° radius of the peripheral target, the target was re-illuminated and stayed on for the duration of the hold period (1.5 ± 0.5 s). The monkey received a liquid reward of 1000 ms (0.75 mL) for successful task completion. There was an 8 ± 2 second intertrial interval before the next trial began. Fixation, memory, and hold periods were subject to timing jitter sampled from a uniform distribution to prevent the monkey from anticipating task state changes.

The memory-guided reach task was similar, but instead of fixation, the monkey used his fingers on a touchscreen. Due to space constraints, eye tracking was not used concurrently with the touchscreen, i.e., only hand or eye position was tracked, not both.

For the memory-guided BMI task, the monkey performed the same fixation steps using his eye or hand position, but the movement phase was controlled by the fUS-BMI. Critically, the monkey was trained to not make an eye or hand movements from the center cue until at least the reward was delivered. For this task variant, the monkey received a liquid reward of 1000 ms (0.75 mL) for successfully maintaining fixation/touch and correct fUS-BMI predictions. The monkey received a 100 ms (0.03 mL) reward for successfully maintaining fixation/touch during incorrect fUS-BMI predictions. This was done to maintain monkey motivation.

5.4.6 fUS-BMI

5.4.6.1 Functional ultrasound sequence and recording

During each fUS-BMI session, we placed the ultrasound transducer (128-element miniaturized linear array probe, 15.6 MHz center frequency, 0.1 mm pitch, Vermon, France) on the dura with ultrasound gel as a coupling agent. We consistently positioned the ultrasound transducer across recording sessions using a slotted chamber plug. The imaging field of view was 12.8 mm (width) by 13-20 mm (height) and allowed the simultaneous imaging of multiple cortical regions, including lateral intraparietal area (LIP), medial intraparietal area (MIP), ventral intraparietal area (VIP), Area 7, and Area 5.

We used a programmable high-framerate ultrasound scanner (Vantage 256; Verasonics, Kirkland, WA) to drive the ultrasound transducer and collect pulse echo radiofrequency data. We used different plane-wave imaging sequences for real-time and anatomical fUS neuroimaging.

5.4.6.2 Real-time low-latency fUS neuroimaging

We used a custom-built computer running NeuroScan Live (ART INSERM U1273 & Iconeus, Paris, France) attached to the 256-channel Verasonics Vantage ultrasound scanner. This software implemented a custom plane-wave imaging sequence optimized to deliver Power Doppler images in real-time at 2 Hz with minimal latency between ultrasound pulses and Power Doppler image formation. The sequence used a pulse-repetition frequency of 5500 Hz and transmitted plane waves at 11 tilted angles equally spaced from -6° to 6°. These tilted plane waves were compounded at 500 Hz. Power Doppler images were formed from 200 compounded B-mode images (400 ms). To form the Power Doppler images, the software used an ultrafast Power Doppler sequence with an SVD clutter filter (Demené et al., 2015) that discarded the first 30% of components. The resulting Power Doppler images were transferred to a MATLAB instance in real-time and used for the fUS-BMI. The prototype 2 Hz real-time fUS system had approximately an 800 ms latency from the end of the ultrasound pulse sequence to arrival of the beamformed fUS image in MATLAB. Each fUS image and associated timing information were saved for post hoc analyses.

5.4.6.3 Anatomical Doppler neuroimaging

At the start of each recording session, we used a custom plane-wave imaging sequence to acquire an anatomical image of the vasculature. We used a pulse repetition frequency of 7500 Hz and transmitted plane waves at 5 angles ([-6°, -3°, 0°, 3°, 6°]) with 3 accumulations. We coherently compounded these 5 angles from 3 accumulations (15 images) to create one high-contrast ultrasound image. Each high-contrast image was formed in 2 ms, i.e., at a 500 Hz framerate. We formed a Power Doppler image of the monkey brain using 250 compounded B-mode images collected over 500 ms. We used singular value decomposition to implement a tissue clutter filter and separate blood cell motion from tissue motion (Demené et al., 2015).

5.4.6.4 fUS-BMI Overview

There were three components to decoding movement intention in real-time: 1) apply preprocessing to a rolling data buffer, 2) train the classifier, and 3) decode movement intention in real-time using the trained classifier. As described previously (10), the time for preprocessing, training, and decoding was dependent upon several factors, including the number of trials in the training set, CPU load from other applications, the field of view, and classifier algorithm (PCA+LDA vs cPCA+LDA). In the worst cases during offline testing, the preprocessing, training, and decoder, respectively, took

approximately 10, 500 ms, and 60 ms. See (Norman et al., 2021) for more description of the amount of time needed for preprocessing, training, and prediction with different sized training sets.

5.4.6.5 Data preprocessing

Before streaming the Power Doppler images into the classification algorithm, we applied two preprocessing operations to a rolling 60-frame (30 seconds) buffer. We first performed a rolling voxel-wise z-score over the previous 60 frames (30 seconds) and then applied a pillbox spatial filter with a radius of 2 pixels to each of the 60 frames in the buffer.

5.4.6.6 Real-time classification

The fUS-BMI made a prediction at the end of the memory period using the preceding 1.5 seconds of data (3 frames) and passed this prediction to the behavioral control system via a TCP-based server (**Supplemental Figure 5.3**). We used different classification algorithms for fUS-BMI in the 2-direction and 8-direction tasks. For decoding two directions of eye or hand movements, we used class-wise principal component analysis (cPCA) and linear discriminant analysis (LDA), a method well suited to classification problems with high dimensional features and low numbers of samples. This method is mathematically identical to that used previously for offline decoding of movement intention (Norman et al., 2021) but has been optimized for online training and decoding. Briefly, we used cPCA to dimensionally reduce the data while keeping 95% variance of the data. We then used LDA to improve the class separability of the cPCA-transformed data. For more details on the method and implementation, see (Das et al., 2007; Das and Nenadic, 2009; Norman et al., 2021).

For decoding eight directions of eye movements, we used a multicoder approach where the horizontal (left, center, or right) and vertical components (down, center, or up) were separately predicted and combined to form the final prediction. As a result of this separate decoding of horizontal and vertical movement components, “center” predictions are possible (horizontal—center and vertical—center) despite this not being one of the eight possible peripheral target locations. To perform the predictions, we used principal component analysis (PCA) and LDA. We used the PCA to reduce the dimensionality of the data while keeping 95% of the variance in the data. We then used LDA to predict the most likely direction. We opted for the PCA+LDA method over the cPCA+LDA for 8-direction decoding because we found in offline analyses that the PCA+LDA multicoder outperformed cPCA+LDA for decoding eight movement directions with a limited number of training trials.

5.4.6.7 Real-time training of model

We retrained the fUS-BMI classifier during the intertrial interval (without stopping the experiment) every time the training set was updated. For the real-time experiments, the data recorded during a successful trial was automatically added to the training set. During the initial training phase, successful trials were defined as the monkey performing the movement to the correct target and receiving his juice reward. Once in BMI mode, successful trials were defined as a correct prediction plus the monkey maintaining fixation until juice delivery.

For experiments that used a model trained on data from a previous session, we used data from all valid trials from the previous session upon initialization of the fUS-BMI. A valid trial was defined as any trial that reached the prediction phase, regardless of whether the correct class was predicted. The classifier then retrained after the addition of each successful trial to the training set during the current session.

5.4.6.8 Post hoc experiments

These experiments analyzed the effect of using only data from a single session on decoder performance. We simulated an online scenario where we trained and/or decoded on each attempted trial in order. We considered all trials where the monkey received a reward as successful and retrained after each trial.

*5.4.6.9 Connection with the behavioral system – **(Supplemental Figure 5.3)***

We designed a threaded TCP server in Python 2.7 to receive, parse, and send information between the computer running the PsychoPy behavior software and the real-time fUS-BMI computer. Upon queries from the fUS-BMI computer, this server transferred task information, including task timing and actual movement direction, to the real-time ultrasound system. The client-server architecture was specifically designed to prevent data leaks: the actual movement direction was never transmitted to the fUS-BMI until after a successful trial had ended. The TCP server also received the fUS-BMI prediction and passed it to the PsychoPy software when queried. The average server write-read-parse time was 31 +/- 1 (mean ± STD) ms during offline testing between two desktop computers (Windows) on a local area network.

5.4.7 Across-session alignment

At the beginning of each experimental session, we acquired an anatomical image showing the vasculature within the imaging field of view. For sessions where we used previous data as the initial

training set for the fUS-BMI, we then performed a semi-automated intensity-based rigid-body registration between the new anatomical image and the anatomical image acquired in a previous session. We used the MATLAB `imregtform` function with the mean square error metric and a regular step gradient descent optimizer to generate an initial automated alignment of the previous anatomical image to the new anatomical image. If the automated alignment had misaligned the two images, the software prompted the proctor to manually shift and rotate the previous session's anatomical image using a custom MATLAB GUI. We then applied the final rigid body transform to the training data from the previous session, thus aligning the previous session with the new session.

5.4.8 Quantification and statistical analysis

Unless reported otherwise, summary statistics reported as XX ± XX are mean ± SEM.

5.4.8.1 Post hoc simulated session

We used the recorded real-time fUS images to simulate the effects of different parameters on fUS-BMI performance, such as using only current session data without pretraining. To do this, we streamed pre-recorded fUS images and behavioral data, frame by frame, to the same fUS-BMI function used for closed-loop, online fUS-BMI. To dynamically build the training set, we added all trials reaching the end of the memory phase regardless of whether the offline fUS-BMI predicted the correct movement direction. This was done because the high possible error rate from bad predictions meant that building the training set from only correctly predicted trials could lead to imbalanced samples across conditions (directions) and possibly contain insufficient trials to train the model; zero correct predictions for certain directions could prevent the model from ever predicting that direction.

5.4.8.2 Searchlight analysis

We defined a circular region of interest (ROI; 200 μm radius) and moved it sequentially across all voxels (left to right then top to bottom) in the imaging field of view. For each ROI, we performed offline decoding with 10-fold cross-validation using either the cPCA+LDA (2-directions) or PCA+LDA (8-directions) algorithm where we only used the voxels fully contained with each ROI. We assigned the mean performance across the cross-validation folds to the center voxel of the ROI. To visualize the results, we overlaid the performance (mean absolute angular error or accuracy) of the 10% most significant voxels on the anatomical vascular map from the session.

5.5 Extended Data

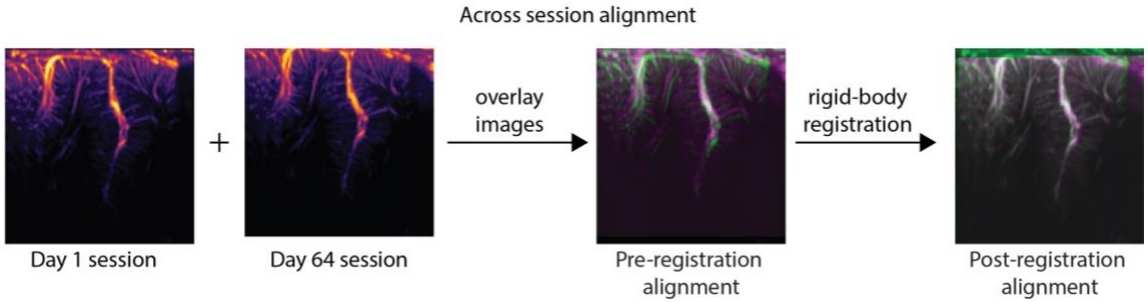

Supplemental Figure 5.1 Across session alignment algorithm.
Supplement to **Figure 5.1.**
We used semi-automated intensity-based rigid-body registration to find the transform from the previous session to the new imaging plane. The registration error is shown in the overlay where green represents the old session (Day 1) and magenta represents the new session (Day 64).

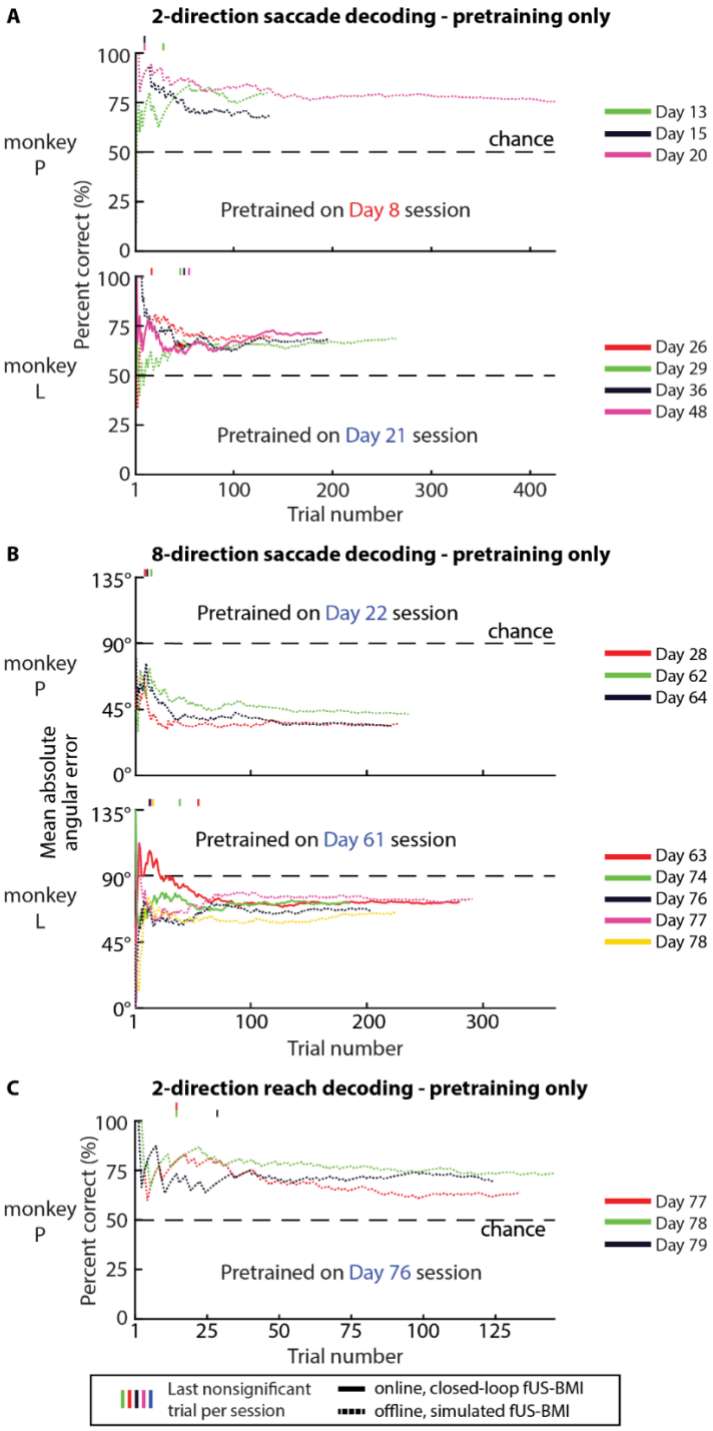

Supplemental Figure 5.2 Closed-loop, real-time decoding of movement directions using pretrained model only. Supplement to **Figures 4.3**, **4.5**, and **4.7.**
(A) Performance for 2-direction saccade decoding using only the pretrained model. (B) Performance for 8-direction saccade decoding using only the pretrained model. (C) Performance for 2-direction reach decoding using only the pretrained model.

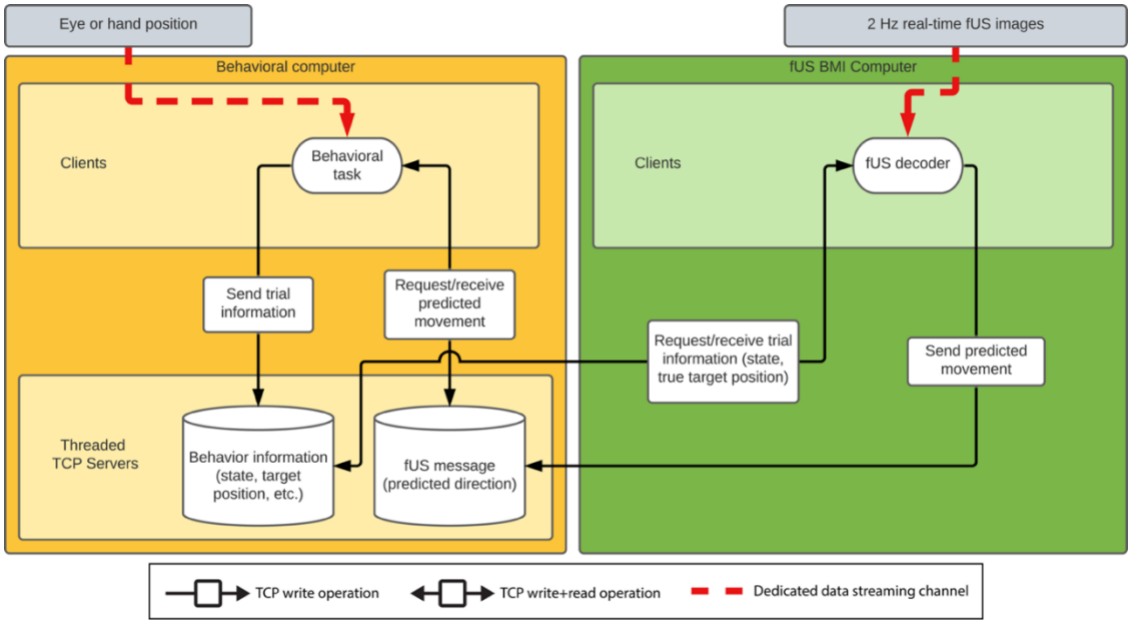

Supplemental Figure 5.3 TCP Communication Architecture for real-time fUS-BMI.
We designed a threaded TCP server in Python 2.7 to receive, parse, and send information between the computer running the PsychoPy behavior software and the real-time fUS-BMI computer. Upon queries from the fUS-BMI computer ("fUS decoder"), this server transferred task information, including task timing and actual movement direction, to a real-time ultrasound system. The client-server architecture was specifically designed to prevent data leaks, i.e., the actual movement direction was never transmitted to the fUS-BMI until after a successful trial had ended. The TCP server also received the fUS-BMI prediction and passed it to the PsychoPy software when queried. The average server write-read-parse time was 31 +/- 1 (mean ± STD) ms during offline testing between two Windows computers on a local area network.

6 Window to the Brain: Ultrasound Imaging of Human Neural Activity Through a Cranial Implant

6.1 Background

Measuring brain function in adult humans holds the key to neuroscience research, precision diagnostics, disease monitoring, and therapeutics for neurological injury and disease. However, our understanding of human brain function is largely limited by the technology we use to access it. We are faced with tradeoffs between sensitivity, coverage, invasiveness, and the ability to record freely moving participants.

There are several techniques available today that monitor brain function in awake humans (**Figure 6.1C**). Functional MRI (fMRI) is capable of measuring function throughout the whole human brain but suffers from limited sensitivity and spatiotemporal resolution. It additionally requires the patient to lie in a confined space and minimize movements, restricting the type of tasks possible (**Figure 6.1D-top**). Other non-invasive methods, such as scalp electroencephalography (EEG) and functional near infrared spectroscopy (fNIRS), are affordable and portable. However, the resulting signals are limited by volume conduction or scattering effects, resulting in poor signal to noise and limited ability to measure function in deep brain regions. Intracranial electroencephalography (iEEG) and electrocorticography (ECoG) have good temporal resolution and better spatial resolution but are highly invasive and require epidural or subdural implantation. Implanted microelectrode arrays set the gold standard in sensitivity and precision by recording the activity of individual neurons and local field potentials. However, these devices are also highly invasive, requiring insertion into the brain (**Figure 6.1D-bottom**). Moreover, they are difficult to scale across many brain regions and have a limited functional lifespan due to tissue rejection. To date, only severely impaired patients whom the benefits outweigh the risk have used invasive recording technologies. There is a clear and distinct need for neurotechnologies that optimally balance the tradeoffs between invasiveness and performance.

Functional ultrasound imaging (fUSI) is an emerging neuroimaging technique that spans the gap between invasive and non-invasive methods. It represents a new platform with excellent sensitivity and brain coverage, enabling a host of new pre-clinical and clinical applications (Deffieux et al., 2018; Rabut et al., 2020). fUSI measures changes in cerebral blood volume (CBV) by detecting the

backscattered echoes from red blood cells moving within its field of view (several cm) (**Figure 6.1E**). It is spatially precise down to ~100 μm with a framerate up to 10 Hz, allowing it to sense the function of small populations of neurons (Montaldo et al., 2022). fUSI is minimally-invasive and requires only removal or replacement of a small skull area in large organisms. fUSI does not intrude on brain tissue but instead sits outside the brain's protective dura mater and does not require the use of contrast agents. fUSI is non-radiative, portable, and proven across multiple animal models (rodents, ferrets, birds, non-human primates, and humans) (Macé et al., 2011). In recent work, we decoded the intentions and goals of non-human primates from fUSI data (Norman et al., 2021) and subsequently, used fUSI as the basis for the first ultrasonic BMI (Griggs et al., 2022).

An important direction of this research is the translation of fUSI-based neuroimaging and BMI for human participants. However, the skull bone attenuates and aberrates acoustic waves at high frequencies, substantially reducing signal sensitivity. As a result, most pre-clinical applications require a craniotomy (Brunner et al., 2021), and the human fUSI studies have required the skull to be removed or absent. These include intra-operative imaging during neurosurgery (Imbault et al., 2017; Soloukey et al., 2020) and recording through the anterior fontanelle window of newborns (Demene et al., 2017). The next challenge for fUSI is to record brain activity in awake adults outside of an operating room.

In this study, we demonstrate fUSI in an awake adult participant equipped with an ultrasound-transparent "acoustic window" installed as part of a cranioplasty (skull replacement procedure) following a decompressive hemicraniectomy (partial skull removal). Hemicraniectomies are commonly performed to reduce pathologically high intracranial pressures, including from traumatic brain injuries (TBIs), strokes, and subarachnoid hemorrhages (Güresir et al., 2009; Alvis-Miranda et al., 2013; Pallesen et al., 2019). After the craniectomy, the scalp is replaced to prevent infection and the patient is left to heal for periods that range from weeks up to a year. After this period, a cranioplasty is performed to replace the missing skull with one of an assortment of cranioplastic reconstruction materials. These include autologous bone, titanium mesh, and polymethyl methacrylate (PMMA). Recently, customized cranial implants (CCIs) have grown in popularity thanks to their sterility, strength, and cosmetic appeal (Iaccarino et al., 2020). One CCI material, PMMA, is also purported to be transparent to ultrasound, or "sonolucent" (Shay et al., 2020). This opened the possibility of using fUSI in a non-invasive setting for low-cost monitoring and diagnostics after implantation of the cranial window. To test this possibility, we evaluated the performance of

fUSI in a patient undergoing a craniectomy (a) before reconstruction, i.e., in the absence of skull, and (b) after CCI reconstruction, i.e., through the scalp and PMMA material.

Before conducting the experiment in the human participant, we examined the imaging characteristics of two FDA- approved materials (PMMA and titanium mesh) for functional (fUSI) ultrasound imaging. We first characterized these materials with an *in vitro* cerebrovascular phantom. We then compared their signal and contrast properties in an *in vivo* rodent model. Finally, we present results demonstrating the detection of functional brain signals while a human subject with a PMMA cranial implant (**Figure 6.1A**) performed visuomotor tasks (**Figure 6.1B**).

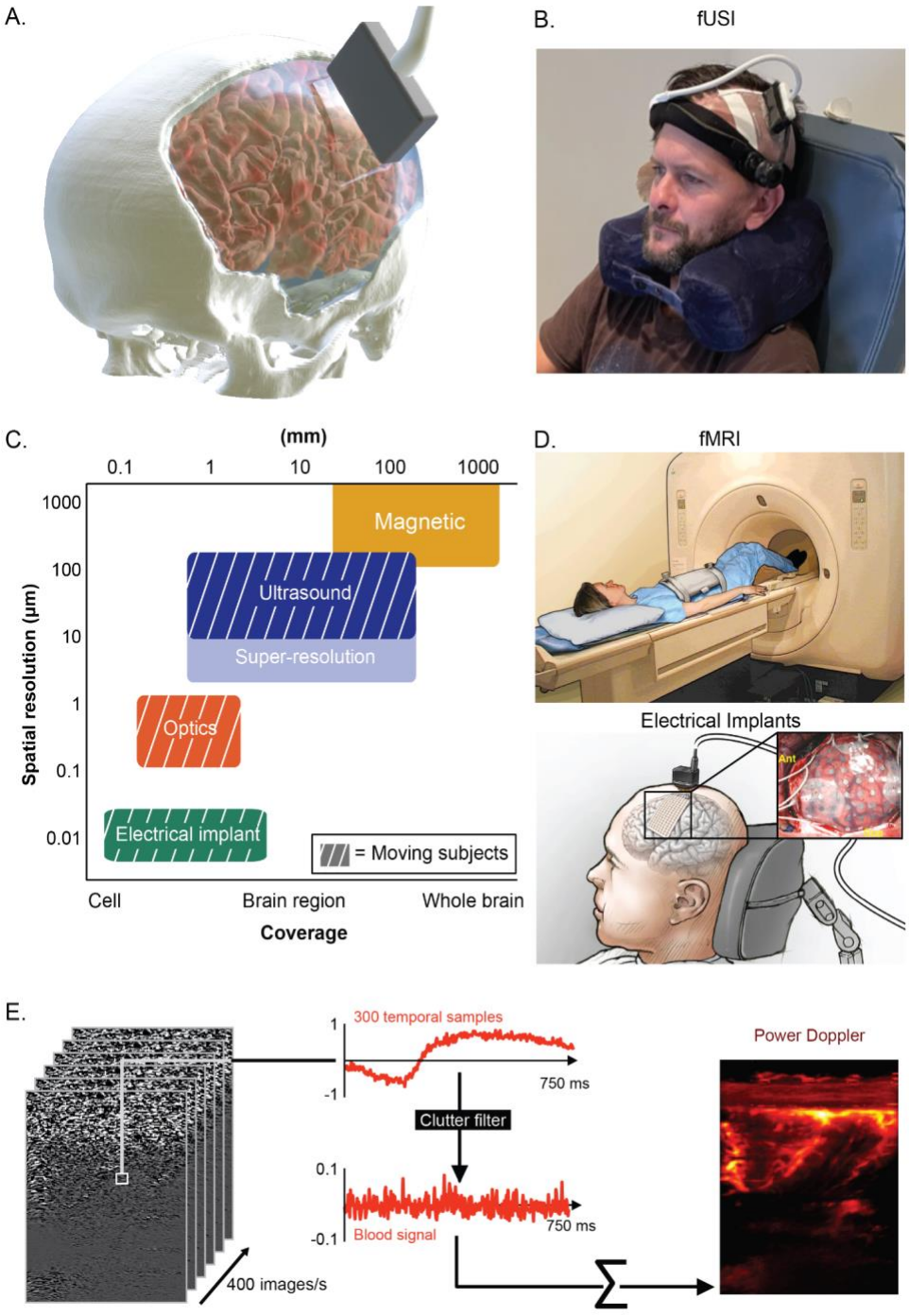

Figure 6.1 Functional ultrasound enables brain imaging in freely behaving subjects with high spatiotemporal resolution and large coverage.

(A) 3D rendering of fUSI recording through the patient's PMMA cranial implant. **(B)** Experimental setup used for fUSI recordings **(C)** Common functional recording modalities on a chart comparing their spatial resolution, coverage, and ability to record moving subjects. or electrical implants. (**D)** Example experimental setups for functional recording in humans using fMRI or electrical implants (**E)** The ultrafast acquisition of ultrasound images allows a fast temporal sampling of the brain signal. We then applied a clutter filter to exclude tissue motion while keeping blood motion for sensitive measurements of CBV variations**.**

6.2 Results

6.2.1 In vitro performance comparison

fUSI is performed by acquiring a series of sequential power Doppler images and observing spatiotemporal changes in the signal. To determine if power Doppler signals can be detected through PMMA material, we first designed and built a Doppler ultrasound phantom with flow channels mimicking human cerebrovasculature (**Figure 6.2A**). This allowed us to measure power Doppler in a controlled environment. We compared five different imaging scenarios: (1) no implant, (2) 1 mm thick PMMA implant, (3) 2 mm thick PMMA implant, (4) 3 mm thick PMMA implant, and (5) titanium mesh implant (**Figure 6.2B, C**). We passed synthetic red blood cells through a 280-μm diameter tubing at three lateral (5, 15, 25 mm) and four axial positions (14, 24, 34, 44 mm) at a constant velocity of ~27 mm/s, and recorded fUSI signals to estimate SNR and resolution loss in each imaging scenario (**Figure 6.2D**). We found that power Doppler intensity decreased with the increase in PMMA implant thickness and also decreased through the titanium mesh (**Figure 6.2E**). SNR decreased with depth and was inversely proportional to the thickness of the intervening PMMA material (**Figure 6.2F**).

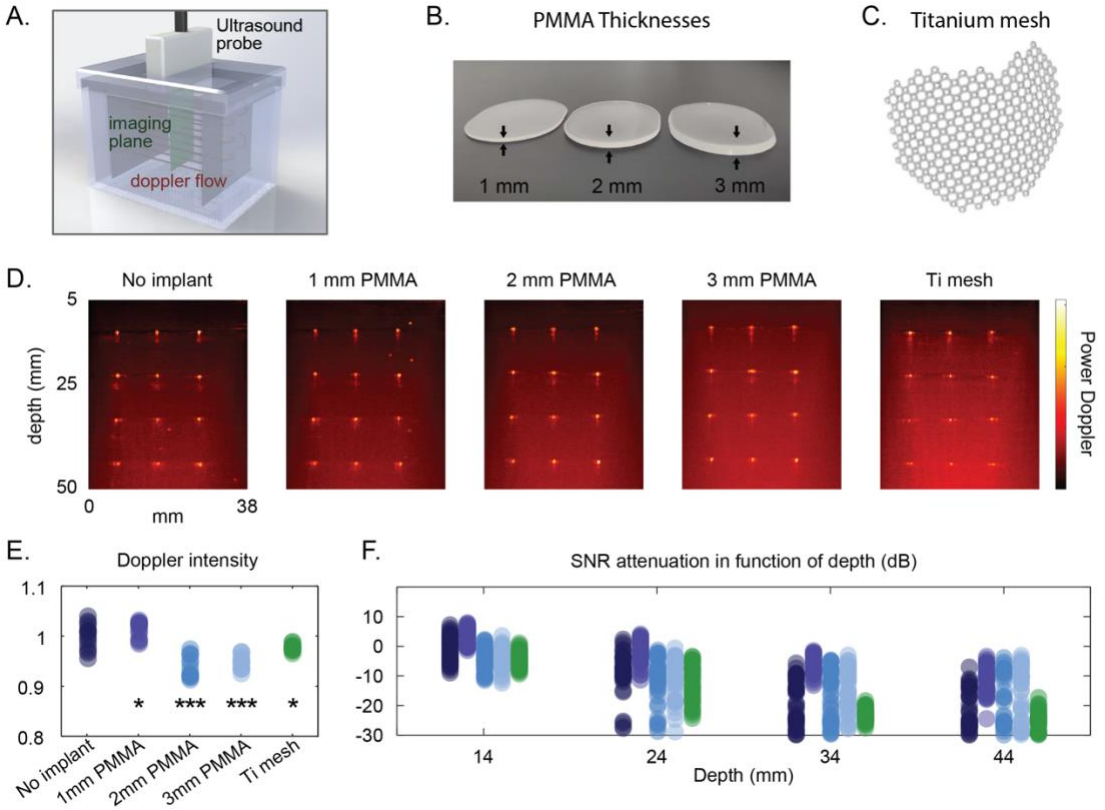

Figure 6.2 Polymeric skull replacement materials enable power Doppler imaging with minimal SNR loss in an in vitro blood flow phantom.
(A) 3D rendering of the *in vitro* Doppler phantom **(B)** Photo of three thicknesses of the PMMA skull-implant material used to evaluate the performance of the *in vitro* Doppler recording through the implants. **(C)** Photo of titanium mesh (commonly used in cranial reconstruction) **(D)** Power Doppler images (see A. for imaging plane) of the Doppler phantom in different implant scenarios. (**E)** Doppler intensity for each implant scenario over N=15 acquisitions. Stars indicate statistical differences (paired sampled t-test) between each scenario compared to the *No implant* scenario (*: $p<0.05$, **: $p<0.01$, ***: $p<0.001$) **(F)** SNR attenuation for each implant scenario as function of the depth (N=15 acquisitions).

6.2.2 Functional activity comparison in rodent model

To test whether we could detect functional signals through the different cranial implant materials *in vivo*, we performed fUSI in four rats for each of the five implant types, (**Figure 6.3A**). The total intensity of the power Doppler signal from the whole brain decreased by 30% from the no-implant scenario to the 1 mm implant scenario (**Figure 6.3B**). The power Doppler intensity dropped a further ~15% per mm implant thickness for the 2 mm and 3 mm materials. The power Doppler intensity decreased by 60% for the titanium mesh compared to no-implant. The SNR loss also decreased as the PMMA implant thickness increased but with a smaller decrease than observed for power Doppler signal intensity. In the cortex, the SNR decreased slightly with the mesh (-1dB) and as the PMMA

implant thickened (~ -1dB/mm). The deep structures within the image showed a similar trend in SNR across the different implant materials.

As we recorded the fUSI signals, we used a visual task where the rat experienced subsequent blocks of darkness (30 frames) and light exposure (10 frames). We modeled the response of each voxel to the visual task using a general linear model (GLM). which allowed us to quantify which voxels showed significant task modulation ($p<1e-5$). Briefly, we convolved our block design ("rest" or "light") with the hemodynamic response function and fit the linear model mapping of the convolved task regressors to each fUSI voxel's signal. This allowed us to assess the statistical significance between the hemodynamic response and task structure for each voxel. In all five implant conditions, we identified voxels within the lateral geniculate nucleus (LGN) activated during the optical stimulation. Using fUSI through the thicker implants and the titanium mesh resulted in fewer task-modulated voxels within the LGN (**Figure 6.3D**). Additionally, we observed less signal change for the thicker vs. thinner implants and titanium mesh vs. any of the PMMA implants ($p<1e-3$, 1-way ANOVA with *post hoc* hsd, **Figure 6.3E**).

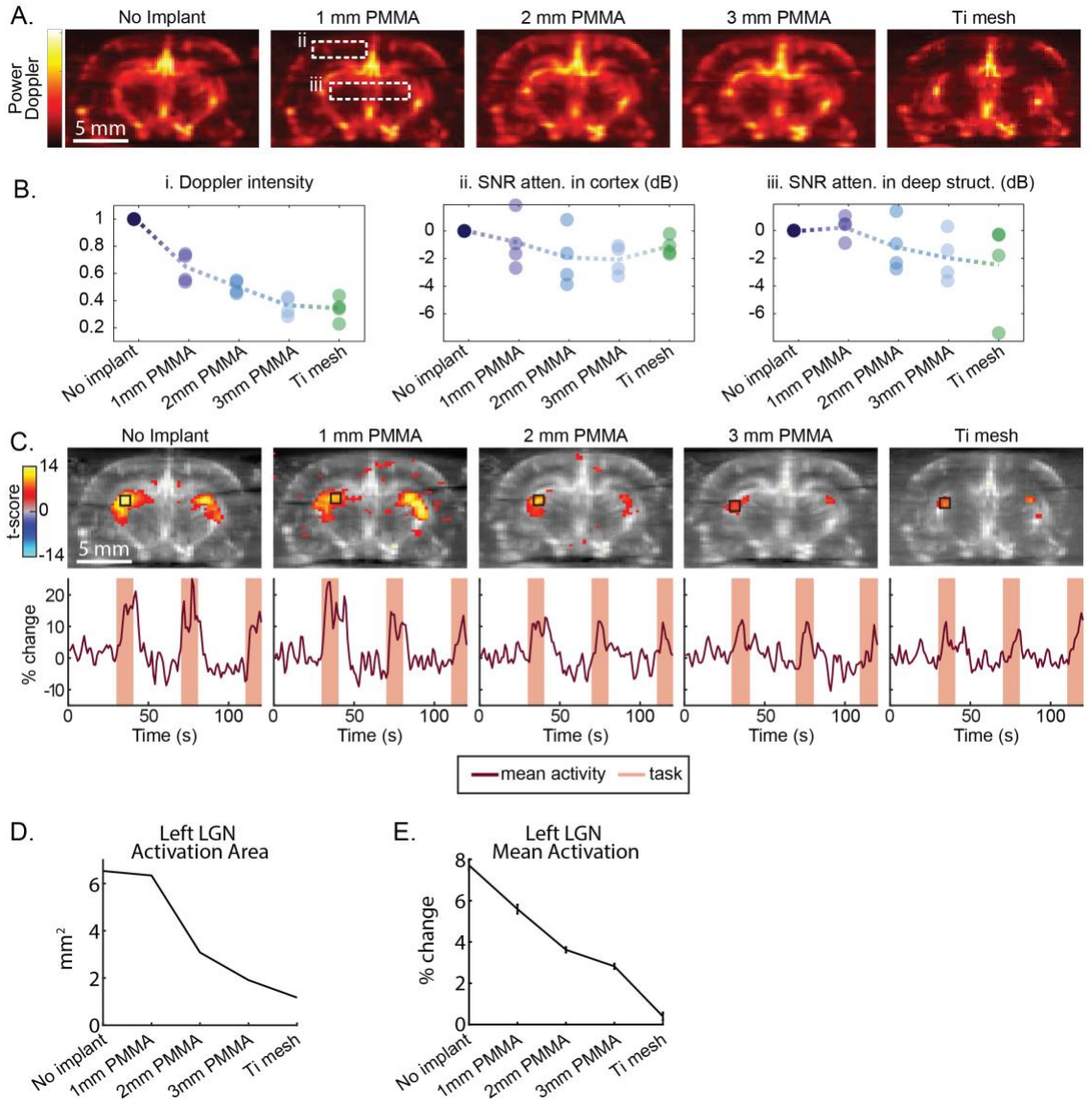

Figure 6.3 Acoustic window materials enable sensitive *in vivo* rodent fUSI imaging.
(A) Power Doppler images of the same rat brain with different skull implant materials. (**B)** Standardized Doppler intensity, standardized SNR in cortex (see dotted box ii of panel (**A)** for cortex region), and standardized SNR in subcortical structures (see dotted box iii of panel (**A)** for subcortical structures region) for each skull implant scenario. (**C)** Light-modulated areas and example time courses. Top row - Statistical parametric map of voxels modulated by visual task (p(corrected)<1e-5) from GLM. Black box shows LGN region used to calculate mean fUSI time course. Bottom row - Time course from LGN region for each skull implant condition. Maroon line - Mean percent change. Orange shading - Light-on condition. **(D)** Area of left LGN activated during light-on condition for each implant material in example session. **(E)** Mean activation during light-on condition for each implant material in example session.

6.2.3 fUSI through decompressive craniectomy window

Having evaluated our ability to detect functional signals through the different implant materials *in vitro* and in an *in vivo* rodent model, we next hypothesized that it would be possible to detect functional brain signals in a human participant with a custom PMMA implant by measuring fUSI while a patient with a CCI performed a visuomotor task.

Approximately 30 months prior to CCI installation, Patient J suffered a traumatic brain injury and underwent a left decompressive hemicraniectomy of approximately 16 cm length by 10 cm height (**Figure 6.1A**). We used anatomical and functional MRI scans acquired after the craniectomy to identify the brain structures and functional cortical regions within the craniectomy borders (**Figure 6.4A-B**).

In the period between the craniectomy and the cranioplasty, we imaged Patient J's brain using ultrasound through his cranial opening at 10.5 months post-craniectomy (**Figure 6.4C**). During this period, we observed large brain vessels following the curve of sulci folds and smaller vessels irrigating the sulci, typical of fUSI images (**Figure 6.4D**). Due to the lack of intracranial pressure, and the dramatic brain motion that results from this condition, we were unable to collect functional data or co-register ultrasound images to anatomical MRI. However, the ability to collect high quality vascular maps provided evidence that fUSI was possible through an intact human scalp.

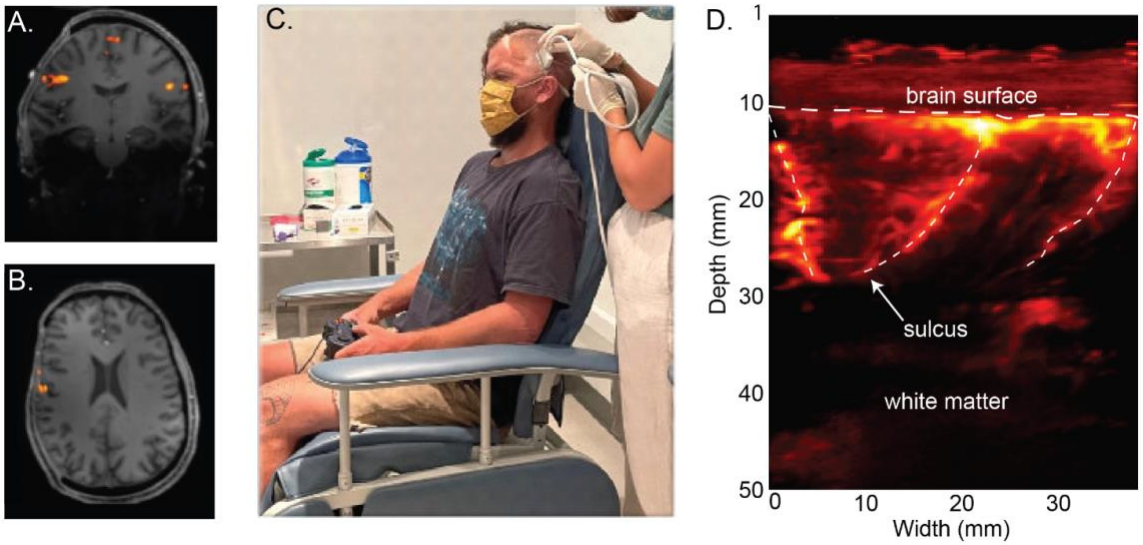

Figure 6.4 Ultrasound enables vascular imaging through intact scalp after craniectomy.
(A) Coronal plane from Patient J's fMRI after their decompressive hemicraniectomy. Orange overlay shows regions activated during finger tapping task (**B)** Transverse plane showing finger-tapping regions. ($p<0.05$ FWE-corrected) **(C)** Patient J during functional ultrasound imaging session with craniectomy (D) Power Doppler image of Patient J's brain through the cranial window.

6.2.4 Cranial implant design for Patient J

To successfully detect functional signal through patient J's CCI, we collaborated with patient J's attending physician (author CL) and the CCI manufacturer to design an appropriate acoustic window. In a separate fMRI study, we identified cortical response fields to a simple finger tapping task (**Fig. 5A)**. Based on this mapping, Longeviti LLC designed and manufactured a PMMA CCI implant for patient J with a 2mm thick 34 x 50 mm parallelogram-shaped sonolucent "window to the brain" placed above the finger-tapping response field (**Figure 6.5B, C**). The outer surface of the implant was matched to the contralateral skull CT for excellent cosmetics and the borders of the implant were matched to the thickness of the bordering skull.

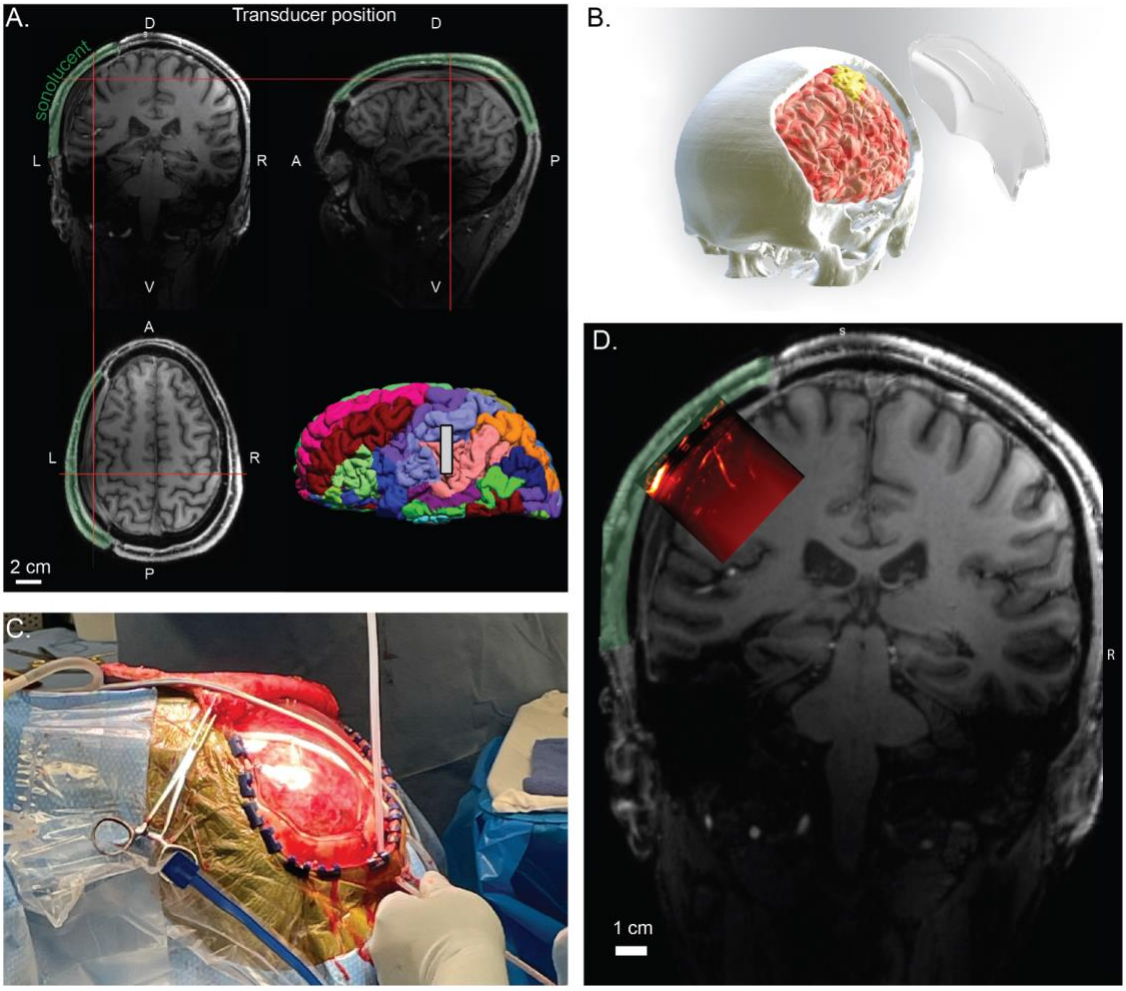

Figure 6.5 Patient J was reconstructed with a custom-designed acoustic window.
(A) MRI scan of Patient J after reconstruction. The red crosses indicate the middle of the transducer during the example fUSI session. Green shading - sonolucent portion of head, including scalp, CCI, and meninges above brain. (**B)** 4mm thick sonolucent cranial implant with the 2 mm thick parallelogram-shaped "window" placed above the finger-tapping task cortical area (yellow region) (**C)** Reconstruction surgery of Patient J with the PMMA CCI. (**D)** Co-registration of the fUSI imaging plane with an anatomical MR image.

6.2.5 First non-invasive fUSI activity recording in human through cranial implant

We imaged Patient J's brain through hist acoustic "window" following cranioplastic reconstruction (**Figure 6.5D)**. To better locate the purported finger-tapping responsive brain regions, we first located the boundaries of the thinned window using real-time anatomical B-mode ultrasound imaging. Once we located the boundaries of the "window", we positioned the ultrasound transducer above the purported functional regions by measuring the relative difference between the window edges and

those regions, as previously measured using the MRI & fMRI scans. We immediately observed the cortical vasculature, including vessels following the curves of sulcal folds and smaller vessels irrigating the adjacent cortex (**Figure 6.5D**).

Based upon a prior fUSI recording session and the location of the thinned window, we estimated we were above the hand region of left primary sensory cortex (S1) and the left supramarginal gyrus (SMG). Among its functions are reports that it plays a role in grasping and tool use (Gallivan et al., 2013; Orban and Caruana, 2014; Vingerhoets, 2014; Buchwald et al., 2018; McDowell et al., 2018; Garcea and Buxbaum, 2019; Potok et al., 2019; Wandelt et al., 2022b). Thus, in an attempt to detect functional brain signals, we instructed Patient J to perform two visuomotor tasks while sitting in a comfortable chair with a screen in front of him (**Figure 6.6A**). In the first task, we used a block design with 60 second "rest" blocks and 30 second "task" blocks. During the rest blocks, we instructed the patient to close their eyes and relax. During the task blocks, the patient used a video game controller joystick. He was instructed to complete "connect-the-dots" puzzles on the computer monitor (**Figure 6.6B**). He used their right thumb to control the game controller's thumbstick (cursor location) and their left index finger to control the left shoulder button (mouse click). We repeated the same tasks across multiple runs (N=3). Finally, we concatenated the data from two runs and used a GLM analysis to identify voxels with functional activation. The GLM revealed several regions that were task modulated (**Figure 6.6D**). The activity within these regions displayed positive modulation by the task, i.e., increased activity during the drawing blocks and decreased activity during the rest blocks (ROI 2, **Figure 6.6D**). For example, ROI 2 had an average of 3.68% difference between the drawing and rest blocks (p value <1e-10, two-sided t-test). Outside of these activated regions (i.e., ROI 1, **Figure 6.6D**), the signal remained stable throughout the run with no significant increase nor decrease during the task periods. For example, ROI 1 had an average difference of -0.034% between the drawing and rest blocks, (p value = 0.67, two-sided t-test). As a step towards translating nonhuman animal results into human applications, we tested the ability to decode task state (rest vs. connect-the-dot) from the fUSI data using a linear decoder. We successfully decoded the task state with 67.8% accuracy (p<1e-5, 1-sided binomial test).

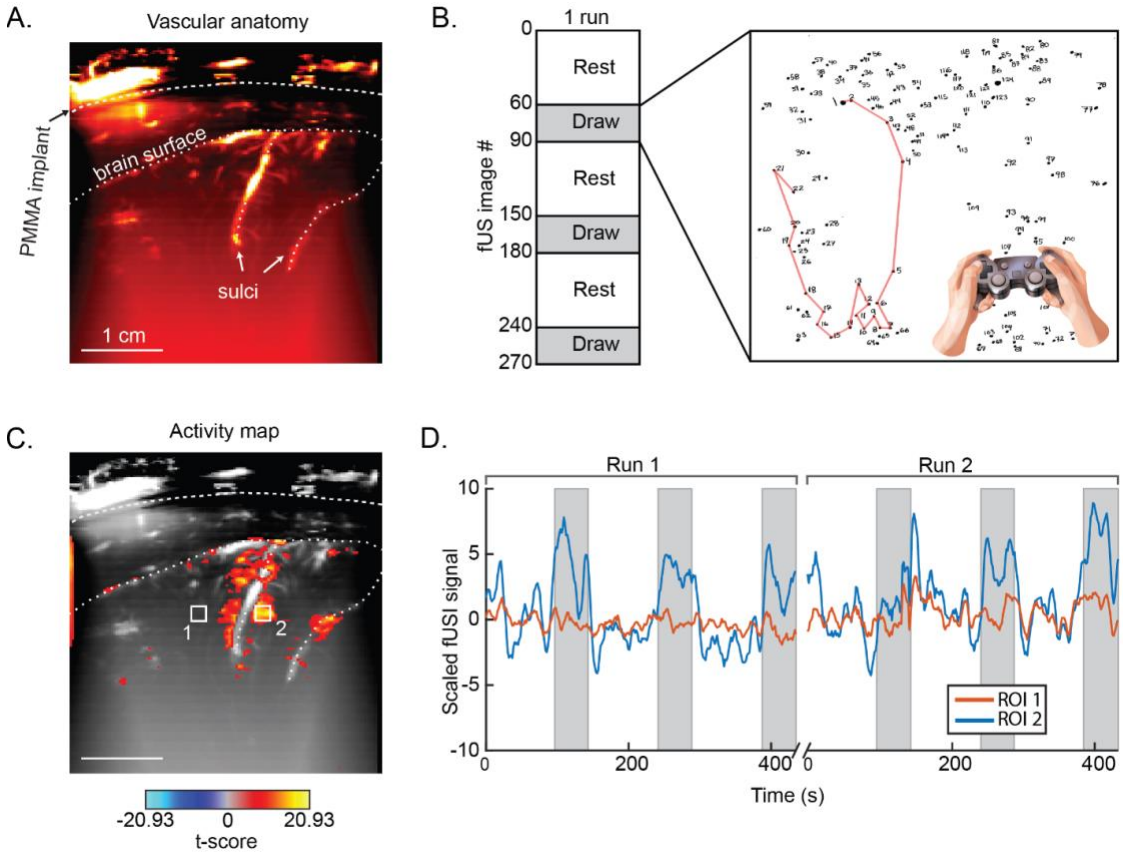

Figure 6.6 Permanent acoustic window allows non-invasive fUSI.
(A) Vascular anatomy of the imaging plane. Dashed lines highlight specific anatomic features, including PMMA implant surface, brain surface, and sulcal vessels. **(B)** Connect-the-dot task. In the rest blocks, the patient relaxed and tried to keep their mind clear. In the task blocks, the patient used a game controller to draw lines in a "connect-the-dots" task. **(C)** Task-modulated areas across two concatenated runs. T-score statistical parametric map threshold at p(corrected) < 1e-10. White boxes shows ROIs used in part D. **(D)** Mean scaled fUSI signal from ROIs. White regions are rest blocks; grey regions are task blocks.

In the second task, we asked Patient J to play guitar while we recorded fUSI data. During the rest blocks, we instructed him to minimize finger/hand movements, close his eyes, and relax. During the task blocks, the patient played improvised or memorized music on a guitar with his right hand strumming and his left fingers moving on the fretboard. We identified several regions that were task-activated, including several that were similar in location to those activated by the connect-the-dots task (**Figure 6.7A, B**).

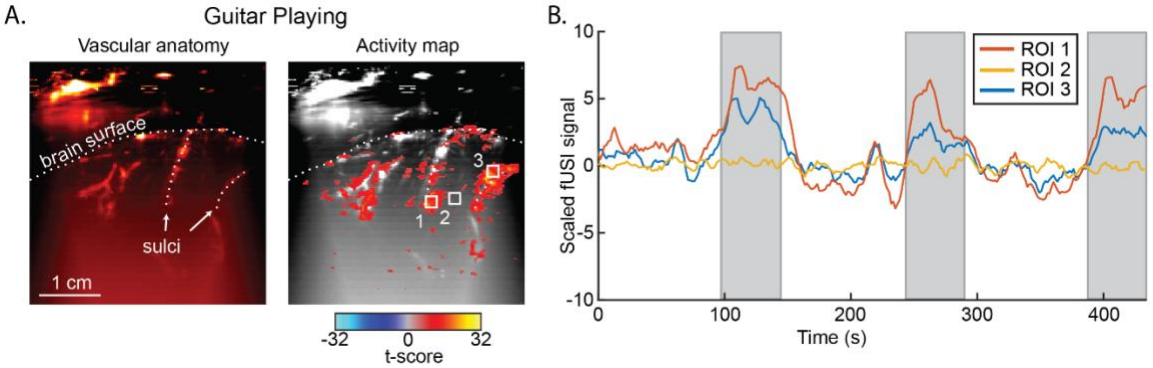

Figure 6.7 Permanent acoustic window allows fUSI detection of guitar playing.
(A) Functional activity evoked by guitar playing task. T-score statistical parametric map threshold at p(corrected) < 1e-10. White boxes shows ROIs used in part B. (**B)** Mean scaled fUSI signal from ROIs. White regions are rest blocks; grey regions are task blocks.

6.3 Discussion

fUSI presents a host of benefits (e.g., increased sensitivity, resolution, and portability) over comparable techniques such as fMRI. However, fUSI cannot penetrate human skull bone while maintaining sufficient sensitivity. In this study, we established the feasibility of awake human fUSI imaging in a non-surgical setting through a polymeric acoustic window. Before testing this approach in humans, we first characterized the acoustic performance of the reconstruction material in *in vitro* and *in vivo* (rodent) settings. This allowed us to determine feasibility of non-invasive imaging through a CCI and optimize the fUSI sequence for maximum sensitivity. We subsequently acquired, for the first time, functional activity of the brain using fUSI in an awake behaving adult patient outside of a surgery.

6.3.1 Diagnostics & monitoring after skull reconstruction (clinical use)

It is currently difficult and expensive to monitor anatomical and functional brain recovery following a cranioplasty. Behavioral assessments, such as Cognitive Status Examination, Mini-Mental State Examination, or Functional Independence Measure are commonly used to assess neuropsychological recovery following traumatic brain injuries (Smith-Knapp et al., 1996; Nabors et al., 1997; de Guise et al., 2011), but cannot identify specific sites of damage or track recovery at these anatomical locations. Less commonly, CT and/or MRI are used to assess anatomical and functional recovery (Scheibel, 2017). However, these methods possess low sensitivity/specificity for assessing brain recovery, are expensive (CT + MRI), and can add risk to the patient (CT). Limited studies have attempted to use 1D transcranial Doppler (TCD) through the temporal window to predict 6-month

clinical outcomes in patients with severe head injuries (Moreno et al., 2000). In this paper, we describe how to use fUSI through a CCI. In the future, sonolucent CCIs may enable routine monitoring during the postoperative period for both anatomical and functional recovery. We can monitor the recovery of individual brain regions and their function, and do so at reduced cost and complexity. Depending on the damaged brain regions beneath the cranial implant, specific tasks can be designed to isolate and test specific brain circuits for recovery.

Some TBI patients will develop Syndrome of the Trephined (SoT), a syndrome where they develop neurological deterioration following a large craniectomy (Ashayeri et al., 2016). Recording from these patients with TBI sequelae or SoT may provide novel insight into the pathophysiology of their disease processes and subsequent recovery.

6.3.2 BMI & neuroscience (research use)

The ability to measure fUSI signals from adult humans with an acoustic window opens tremendous opportunities for BMI and neuroscience research. Approximately 1.7 million people suffer from a severe traumatic brain injury each year in the United-States (Georges and M Das, 2023). If only a small fraction of these patients receive a sonolucent cranial implant as part of their standard of care, it would provide a major opportunity to measure mesoscopic neural activity with excellent spatiotemporal resolution and high sensitivity in humans. In those patients with minimal long-term neurological damage, it will also enable new investigations into advanced neuroimaging techniques and BMIs. As we demonstrated in this paper, fUSI possesses high sensitivity even through the cranial implant.

6.3.3 Future work

This study demonstrates that functional ultrasound signals can be monitored with high sensitivity through a PMMA implant. Future work will be critical for translating this finding into impactful clinical applications. As one example, previous researchers have found that transcranial Doppler (TCD) can be used to monitor intracranial pressure (ICP) and cerebral perfusion pressure (CPP), two important clinical measures for assessing acute and chronic neurological injuries and diseases (Rosenberg et al., 2011). fUSI with its high sensitivity and large field of view may be able to measure ICP and CPP with higher accuracy and precision than TCD.

Furthermore, this work may serve as a basis for research and clinical neuroprosthetics, and BMIs. As these technologies gain popularity and user base, the need for novel sensing techniques is growing.

Current state-of-the-art BMIs use highly invasive electrodes that limits their use to narrow patient populations (e.g. quadriplegia), and typically last less than 5 years. Minimally-invasive techniques that maintain high sensitivity and spatiotemporal resolution hold great promise for accelerating the field. fUSI through a sonolucent cranial window could be a much safer and less invasive recording modality, especially for patient populations already undergoing this procedure. This research platform could expand the span of BMI use cases. For example, approximately 280 million people suffer from depression worldwide (Institute of Health Metrics and Evaluation, 2019). Although the risk-benefit tradeoff of an invasive BMI is currently difficult to justify for these patients, a small sonolucent cranial window may provide a more viable solution. This minimally-invasive surgery would enable the investigation of ultrasonic "mood" BMIs (Shanechi, 2019).

6.4 Conclusion

Recording high-quality, spatiotemporally precise brain signals in humans will be critical to developing new evidence-based treatment for neurological and psychiatric injuries and diseases. To date, these methods were either highly invasive with high signal quality or non-invasive with low spatiotemporal resolution and signal quality. Here, we introduced an intermediate solution: In a patient with a polymeric acoustic window, we recorded spatially precise (200 μm) and highly sensitive measures of brain function. In certain patient populations, this minimally-invasive cranial replacement paired with non-invasive fUSI may be justified to track recovery from neurological injuries, monitor neurodegeneration in terminal conditions, and even provide novel therapies (ultrasound neurofeedback or neuromodulation). This would not only help researchers to better understand the neural circuits affected by brain injuries and disorders, but has clear pathways toward clinical translation that could one day benefit patients directly.

6.5 Materials and Methods

6.5.1 General

All analysis was completed in MATLAB 2021a.

6.5.2 Implant materials

We tested two different types of cranioplasty materials: polymethyl methacrylate (PMMA) and titanium mesh. We used 1-, 2-, and 3-mm thick PMMA disks provided by Longeviti to test the effects of different implant thicknesses of signal quality and strength. See details below for more details on

the custom PMMA cranial implant designed for Patient J (**Chapter 6.5.8**). We used 0.6 mm thick titanium mesh that had a honeycomb pattern alternating between small and large circles (1.5 mm and 3 mm diameter; KLS Martin).

6.5.3 Functional ultrasound imaging

Functional ultrasound imaging (fUSI) visualizes neural activity by mapping local changes in cerebral blood volume (CBV). CBV variations are tightly linked to neuronal activity through the neurovascular coupling (Iadecola, 2017) and are evaluated by calculating power Doppler variations in the brain (Mace et al., 2013). We used a 7.5 MHz ultrasonic probe (128 elements, 0.300 mm pitch, Vermon, Tours, France) connected to a 256-channel Vantage ultrasound system (Verasonics Inc., Redmond, WA, USA) controlled by custom MATLAB B-mode and fUSI acquisition scripts. Each Power Doppler image was obtained from the accumulation of 300 compounded frames acquired at 400 Hz frame rate. Each compounded frame was created using 2 accumulations of 5 tilted plane waves (-6°, -3°, 0°, 3°, 6°). We used a pulse repetition frequency (PRF) of 4000 Hz. Power Doppler images were repeated every ~1.5 seconds. Each block of 300 images was processed using a SVD clutter filter (Demené et al., 2015) to separate tissue signal from blood signal to obtain a final Power Doppler image exhibiting artificial (for in vitro experiment) or cerebral blood volume (CBV) in the whole imaging plane (Fig. 1C).

6.5.4 In vitro tissue anatomical and doppler phantoms

We routed 280 µm inner diameter polyethylene tubing through a hollow, box-shaped, 3D-printed, nylon cast at three lateral positions and five axial positions (15 grid points, total). We then poured a liquid gelatin phantom with graphite added to mimic the scattering effects of biological soft tissue. Once the phantom cast had set/solidified, we flowed a red blood cell phantom liquid (CAE Blue Phantom™ Doppler Fluid) through the tubing using a peristaltic pump and a long recirculating route with a low pass filter to create a smooth flow at velocities of approximately 0.1 mm/s.

6.5.5 In vivo functional ultrasound imaging comparative study in rat

Four Long-Evans male rats were used in this study (15-20 weeks old, 500–650 g). During the surgery and the subsequent imaging session, the animals were anesthetized using an initial intraperitoneal injection of xylazine (10 mg/kg) and ketamine (Imalgene, 80 mg.kg-1). The scalp of the animals was removed and the skull was cleaned with saline. A craniectomy was performed to remove a 0.5 mm × 1 cm portion of the skull by drilling (Foredom) at low speed using a micro drill steel burr (Burr

number 19007-07, Fine Science Tools). We took care to avoid damage to the dura and prevent inflammation. After surgery, the surface of the brain was rinsed with sterile saline and ultrasound coupling gel was placed on the window. The linear ultrasound transducer was positioned directly above the cranial window or cranial implant material and we performed fUSI scans during the visual experiment described below.

fUSI with visual stimuli was performed in all animals. Visual stimuli were delivered using a blue LED (450 nm wavelength) positioned at 5 cm in front of the head of the rats. Stimulation runs consisted of periodic flickering of the blue LED (flickering rate: 5 Hz) using the following parameters: 30 s dark, followed by 10 s of light flickering repeated three times for a total duration of 120 s. At this distance, the light luminance was of 14 lux when the light was on and ~0.01 lux when the light was off.

6.5.6 fUSI data processing

For the rodent and human in vivo experiments, we used a general linear model (GLM) to find which voxels were significantly modulated by the visual task. To perform this GLM, we first preprocessed the fUSI data with nonlinear motion correction (Pnevmatikakis and Giovannucci, 2017), spatial smoothing (2D Gaussian with sigma=1 (FWHM = 471 um), and a voxelwise moving average temporal filter (rat - 2-timepoints; human - 5-timepoints). We then scaled the fUSI signal by its voxelwise mean so that all of the runs and voxels had a similar signal range (Chen et al., 2017). To generate the GLM regressor for the visual task, we convolved the block task design with a single Gamma hemodynamic response function (HRF) (Boynton et al., 1996). For the rodent experiments, we used the following HRF parameters: time constant (τ)=0.7, time delay (δ)=1 sec, phase delay (n)=3 sec. For the human experiments, we used the following HRF parameters: τ=0.7, δ=3 sec, n=3 sec. We next fit the GLM using the convolved regressor and the scaled fUSI signal from each voxel. We determined statistical significance of the beta coefficients for each voxel using a 2-sided t-test with False Discovery Rate (FDR) correction (p (corrected) < 1e-5).

6.5.7 Decompressive hemicraniectomy and reconstruction procedure

Patient J underwent a decompressive hemicraniectomy to relieve intracranial pressure following a severe traumatic brain injury on April 9, 2019. The approximate size of the hemicraniectomy was 16 cm in the anterior-posterior axis by 10 cm in the dorsal-ventral axis (**Fig. 4B**). A 700 um isotropic anatomical MRI was acquired shortly after the hemicraniectomy. The patient underwent a

cranioplasty to repair the skull defect with the custom skull implant on September 22, 2021. CL performed these surgeries at Keck Hospital of USC.

6.5.8 Skull implant design

The PMMA skull implant (Longeviti ClearFit) was designed to fit the hemicraniectomy and match the geometry of the right side of the intact skull. The implant was 4-mm thick to match the patient's nominal bone thickness except for a 34 x 50 mm parallelogram-shaped "window" of 2 mm thick PMMA positioned over the area of the brain known to be active during finger tapping, based on the results of a functional MRI experiment.

6.5.9 Human participant

We recruited and consented a 37-year-old male participant (Patient J) with a traumatic brain injury to participate in a research study examining the ability to record functional ultrasound signals through a custom cranial implant. All procedures were approved by the Institutional Review Boards (IRB) of the University of Southern California (USC), California Institute of Technology (Caltech), and Rancho Los Amigos National Rehabilitation Hospital (RLA). All fUSI study sessions took place at Caltech. All CT and MRI scans occurred at the Keck Hospital of USC.

6.5.10 Human fUSI task

Patient J sat in a reclining chair with a 27-inch fronto-parallel screen (Acer XB271HU) positioned 70 cm in front of him. Patient J controlled the behavioral task using a Logitech F310 Gamepad. We used Gopher (https://github.com/Tylemagne/Gopher360) to enable control of the computer with the Logitech Gamepad. Right thumbstick controlled the position of the computer cursor while the left shoulder button functioned as the left mouse button. We used a block design for the drawing task with 30 or 60 frame rest blocks followed by 30 frame blocks of drawing with the Gamepad. We verbally instructed the patient for each rest or task block. The patient was instructed to complete one of multiple "Connect-The-Dots" drawings (**Fig. 6B**). When the patient finished one of the drawings, we presented a new drawing for him to complete. For the rest blocks, we instructed the patient to close their eyes and try to keep their mind relaxed. We acquired fUSI data at 0.6 Hz (1.65 sec/frame).

For the guitar playing task, we used an identical block design with 60 frame rest blocks followed by 30 frame task blocks. In the task blocks, the patient used his left hand to form chords on the fretboard and his right hand to strum the strings.

6.5.11 Task decoding

To decode whether a given timepoint was in a “task” or “rest” block, we used principal component analysis combined with a support vector machine (PCA+SVM). We first labeled each motion-corrected fUSI timepoint (“sample”) as “rest” or “task”. We then balanced the dataset to have equal number of “rest” and “task” timepoints. We then split the dataset at the level of block pairs (1 block pair = rest+task) to avoid training the classifier on time points immediately adjacent to the test time points. This helps ensure that the model would generalize and that our model was not “memorizing” local patterns for each block pair. We then applied a 2D Gaussian smoothing filter (sigma=1) to each sample in the train and test sets. We then preprocessed the train set with a 50-window detrend to remove drift across the run and voxelwise z-score across time. We then trained and validated the PCA+SVM classifier using a blockwise leave-one-out cross-validator; i.e., we trained on 5 blocks and then tested on the held-out block pair’s timepoints.

7 Conclusion

7.1 Summary of current work

This dissertation is a novel exploration of how an emerging neurotechnology, functional ultrasound imaging (fUSI), can help elucidate the mesoscopic representation of action variables (movement direction, task state, and reward) within PPC and how this technology can be used to develop less-invasive, yet high-performing, BMIs.

We first explored how saccadic movement direction was represented within and across different coronal PPC planes (**Chapter 3**). Discrete cortical patches encoded for different movement directions and enabled offline decoding of intended movement direction on individual trials. These cortical patches were stable across many months to years, suggesting that fUSI-based decoders would need minimal, if any, retraining on new sessions before they would have high decoding accuracy. We additionally confirmed a rough topography across LIP where cortical patches in anterior LIP more often encoded for contralateral upward directions while cortical patches in posterior LIP more often encoded for contralateral downward directions. Additionally, there was no statistically significant difference in decoder performance trained on the different coronal planes. This demonstrated that unique information about movement direction was distributed across the anterior-posterior aspects of LIP and suggested that an optimal fUSI-based decoder should capture information from a 3D volume rather than isolated coronal planes.

In **Chapter 4**, we explored how non-directional signals were encoded within PPC, including task state and variables related to action desirability. Trial-averaged fUSI revealed complex spatiotemporal patterns for the different states of the memory-guided saccade task. We could leverage linear fUSI-based decoders to predict the task state from single timepoints at well above chance level. Since the performance was ~60% (chance level 20%) with the highest confusion for temporally-adjacent states, we proposed improved decoder models that would incorporate temporal information, such as including a Hidden Markov Model in the decoder algorithm.

We additionally identified small mesoscopic populations within the dorsal LIP modulated by reward magnitude. These populations had increased hemodynamic activity for larger reward sizes. Using a linear fUSI-based decoder, we could simultaneously decode intended movement direction and expected reward magnitude. This supported that fUSI was sensitive to detect weaker non-directional

signals from PPC and would be a good candidate for neuropsychiatric BMIs aimed at decoding mood states.

Having demonstrated the types of signals that we could robustly decode from the PPC, we next developed an online, closed-loop ultrasonic BMI (i.e., fUSI-BMI) and trained two monkeys to use it for multiple directions of eye or hand movements (**Chapter 5**). Both monkeys could control the fUSI-BMI at well above chance level for two directions of reach movements and eight directions of eye movements. We additionally demonstrate that we can pretrain the fUSI-BMI using data from a previous session and that this allowed us to start decoding above chance level from close to the start of the session, even without retraining the model. This built upon our earlier work (Norman et al., 2021) where we had previously demonstrated the first proof-of-concept real-time fUSI-BMI using offline pre-recorded data. This chapter demonstrated the first high-performance ultrasonic BMI and supports future work on developing ultrasonic BMIs for other applications, such as detecting aberrant mood states (e.g., depression or anxiety) and restoring patients to more euthymic states (e.g., less depressed or anxious).

In pursuit of developing an ultrasonic BMI with human applications, we finally presented work where we recorded fUSI signals in an awake, behaving human through a sonolucent skull replacement (**Chapter 6**). To do this, we first characterize our ability to record fUSI signals through titanium mesh and different thickness polymethyl methyl acrylate (PMMA), two materials used for cranioplasties. Using our Doppler phantom, fUSI could detect functional signals through all the materials although the signal-to-noise ratio was inversely correlated with the PMMA thickness and was the worst in the titanium mesh. We next test the different cranioplasty materials in an *in vivo* rodent model. In agreement with the *in vitro* tests, fUSI sensitivity was inversely proportional to implant thickness and was worst in the titanium mesh. Finally, we tested fUSI in a human who received a PMMA cranioplasty with a 2-mm thinned window positioned above the posterior frontal lobe and anterior parietal lobe. While our subject performed a variety of blocked tasks, including connect-the-dot with a videogame controller and playing guitar, we could robustly detect task-related signals. We subsequently registered our fUSI imaging plane to previously acquired anatomical MRIs and identified that we had been recording above the hand region of the primary sensory cortex and the supramarginal gyrus, an area implicated in complex tool use and speech generation. The results presented in this chapter are the first high-quality fUSI images in an awake behaving human and we

propose some future directions of this work to continue translating pre-clinical fUSI results from rodents, monkeys, and other species into human applications.

7.2 Future directions

We presented work on a wide range of topics, including functional ultrasound neuroimaging, stability of mesoscopic populations across time, and encoding of action within PPC. This creates numerous opportunities for further interdisciplinary investigations that range from improved functional ultrasound acquisition methods to novel methods for cortical layer analyses to tracking learning in mesoscopic populations across months. We highlight a few possible extensions below.

7.2.1 Neuropsychiatric BMIs for treating mood disorders

Approximately 600 million, or approximately 10% of, people worldwide suffer from depression, anxiety, or other mood disorders (Dattani et al., 2021), making it a massive public health crisis (Lopes et al., 2022). The most common therapies consist of medications and/or behavioral therapy. However, medications and therapy only works for ~33% of patients, with the rest being treatment-resistant (Rush, 2023). Other therapies include electroconvulsive therapy (Espinoza and Kellner, 2022), transcranial magnetic and direct current stimulation (Loo et al., 2012; Xie et al., 2013), vagus nerve stimulation (Rush et al., 2005; Martin and Martín-Sánchez, 2012), and electrical stimulation via deep brain stimulation electrodes (Dougherty et al., 2015; Bergfeld et al., 2016; Holtzheimer et al., 2017). These methods have various downsides, including variable efficacy, invasiveness, and cognitive side effects (Delaloye and Holtzheimer, 2014).

One area of ongoing research to help these people with treatment-resistant depression is to develop BMIs for neuropsychiatric applications (Shanechi, 2019). This may help patients who have exhausted other treatments while also developing novel therapies with fewer adverse effects. If aberrant moods can be detected before they become severe, then less medication, therapy, or other treatments may be needed to restore them to a euthymic state or abort their aberrant mood progression. Ideally, the BMI would measure a brain signal, or biomarker, that is highly correlated with different mood states. When the beginning of an aberrant mood state is detected, the BMI could adjust the therapy, such as precisely stimulating specific brain regions (Scangos et al., 2021b). Many researchers have tried to identify biomarkers of different mood disorders, specifically whether someone is currently in an aberrant mood state, but it has proven challenging (Insel, 2014; Williams, 2016; Bouthour et al., 2019). Recently, researchers demonstrated the first closed-loop BMI for treatment-resistant

depression (Scangos et al., 2021a) in a single patient with depth electrodes (NeuroPace RNS System) placed in amygdala (sensing) and ventral capsule/ventral striatum (stimulation). Despite the promise of this technique, electrode-based sensing technologies have their limitations for neuropsychiatric applications. First, the electrodes can only sample from very small portions of the brain (**Figure 2.1**), making it difficult to precisely position the electrode(s) in locations that are effective for recording relevant signals or stimulating relevant brain circuits. Second, the electrophysiology signals drift across multiple hours to days, making it challenging to consistently record the same neural population that are predictive of different mood states. Third, the inflammatory response to depth electrodes typically leads to signal degradation within a few years, impairing the ability to sense mood biomarkers.

fUSI is a technique that may be ideally suited for a neuropsychiatric BMI. It can record from distributed brain regions via one or more transducers; the hemodynamic signal it measures varies on the order of minutes, thus matching the same timescale as mood; it can track the same anatomical volumes with high precision across days and months; it can be made portable (unlike fMRI); and it can potentially be used for ultrasound neuromodulation (Darmani et al., 2022). We believe there is tremendous opportunities for research along this direction, such as recording fUSI signals in patients with hemicraniectomies or sonolucent skull replacements from brain areas implicated in mood disorders (thalamus, amygdala, prefrontal cortex, etc.) while also tracking their mood states.

7.2.2 4D fUSI-BMI

All of the work in this dissertation used 3D (2D + time) fUSI acquisition with a linear ultrasound transducer. There has been tremendous progress in the last several years towards developing 4D (3D + time) fUSI acquisition systems with high sensitivity (Rabut et al., 2019; Brunner et al., 2020, 2021). As these systems become faster and more accessible to a wide range of researchers, they will enable a better understanding of the mesoscopic functional organization of entire brain regions. In **Chapter 3**, we recorded data from planes spaced 1.667 mm apart across multiple different sessions and found a rough topography. A volumetric fUSI system would have allowed us to collect fewer sessions of data. Additionally, it would have enabled us to track the spatiotemporal hemodynamic patterns that propagate throughout PPC rather than just within a narrow 2D imaging plane.

Additionally, the real-time fUSI-BMI would likely benefit from additional information captured by an entire volume rather than isolated planes in at least two regards. First, it would improve the

coregistration across days and likely improve the decoder's stability. Second, different planes have different preferred directions so that may lead to fUSI decoders with higher performance.

7.2.3 fUSI-guided electrophysiology

One of the challenges associated with invasive electrophysiology is identifying where to record. Historically, this was based upon lesion studies where removing certain parts of the brain affected certain behaviors. More recently, researchers have used fMRI to identify areas with macroscopic activity related to specific tasks. However, it remains challenging to precisely position invasive electrodes to the desired target. This is particularly difficult for small subcortical targets, such as the caudate tail, claustrum, or specific thalamic nuclei. Electrophysiologists frequently use guide grids with evenly spaced holes every 0.5-1 mm, but even with that, there is tremendous day-to-day variability in location of the electrode, especially for deep brain structures where small changes in penetration angle leads to recording from very different anatomical locations. Electrophysiologists frequently rely upon nearby anatomical structures to help identify where their electrode is on a given day. For example, for targeting the caudate tail, researchers will typically first find the boundaries of the lateral geniculate nucleus (LGN), a structure with well characterized visual response patterns, and then move their electrode lateral a few millimeters on subsequent recording sessions. fUSI can help with this problem. It can be used to identify mesoscopic locations with task-relevant activity. It can also be used to image the electrode itself and see where the electrode is in real-time relative to the ultrasound imaging plane or volume. A similar approach was used previously with B-mode ultrasound (Glimcher et al., 2001).

In addition to guiding placement of invasive electrodes, it can be used as a complementary recording technology to understand how localized activity within a small volume is related to broader activity in the entire region. Similar methods have already been used to better understand the relationship between the mesoscopic CBV changes measured by fUSI and the activity of individual or multiple neurons measured by electrophysiology or calcium imaging (Boido et al., 2019; Aydin et al., 2020; Bourgeais-Rambur et al., 2022; Nunez-Elizalde et al., 2022).

7.3 Final thoughts

Taken together, the work presented here is a novel characterization of how functional ultrasound neuroimaging may enable a new generation of BMIs. Additionally, this dissertation provides a large

corpus that supports fUSI as a robust and accessible neuroimaging technique for future neuroscience questions about mesoscopic populations and their interrelationships throughout the brain.

Functional ultrasound imaging is a rapidly advancing neurotechnology for pre-clinical and clinical research. We highlighted several applications, both human and nonhuman, for this technology, including ultrasonic BMIs and imaging through sonolucent skull replacements. We believe this technology will continue to develop rapidly and become a valuable tool for elucidating answers to currently difficult, if not intractable, neuroscience questions.

8 Bibliography

Achtman N, Afshar A, Santhanam G, Yu BM, Ryu SI, Shenoy KV (2007) Free-paced high-performance brain–computer interfaces. J Neural Eng 4:336.

Aflalo T, Kellis S, Klaes C, Lee B, Shi Y, Pejsa K, Shanfield K, Hayes-Jackson S, Aisen M, Heck C, Liu C, Andersen RA (2015) Decoding motor imagery from the posterior parietal cortex of a tetraplegic human. Science 348:906–910.

Ahn M, Jun SC (2015) Performance variation in motor imagery brain–computer interface: A brief review. J Neurosci Methods 243:103–110.

Akbari H, Khalighinejad B, Herrero JL, Mehta AD, Mesgarani N (2019) Towards reconstructing intelligible speech from the human auditory cortex. Sci Rep 9:874.

Alahi MEE, Liu Y, Khademi S, Nag A, Wang H, Wu T, Mukhopadhyay SC (2022) Slippery epidural ECoG electrode for high-performance neural recording and interface. Biosensors 12:1044.

Aleem I, Chau T (2013) Towards a hemodynamic BCI using transcranial Doppler without user-specific training data. J Neural Eng 10:016005.

Alvis-Miranda H, Castellar-Leones SM, Moscote-Salazar LR (2013) Decompressive craniectomy and traumatic brain injury: A review. Bull Emerg Trauma 1:60–68.

Andersen R (1988) Visual and visual-motor functions of the posterior parietal cortex. In: Neurobiology of Neocortex (Rakic P, Singer W, eds), pp 285–295. John Wiley & Sons Limited.

Andersen RA, Aflalo T, Kellis S (2019) From thought to action: The brain–machine interface in posterior parietal cortex. Proc Natl Acad Sci USA 116:26274–26279.

Andersen RA, Andersen KN, Hwang EJ, Hauschild M (2014) Optic ataxia: From Balint's syndrome to the parietal reach region. Neuron 81:967–983.

Andersen RA, Buneo CA (2002) Intentional maps in posterior parietal cortex. Annu Rev Neurosci 25:189–220.

Andersen RA, Cui H (2009) Intention, action planning, and decision making in parietal-frontal circuits. Neuron 63:568–583.

Andersen RA, Essick GK, Siegel RM (1985) Encoding of spatial location by posterior parietal neurons. Science 230:456–458.

Andersen RA, Essick GK, Siegel RM (1987) Neurons of area 7 activated by both visual stimuli and oculomotor behavior. Exp Brain Res 67 Available at: http://link.springer.com/10.1007/BF00248552 [Accessed March 26, 2020].

Anon (2021) Quick statistics about hearing. NIDCD Available at: https://www.nidcd.nih.gov/health/statistics/quick-statistics-hearing [Accessed February 15, 2023].

Anon (2023a) Electroencephalography. Wikipedia Available at: https://en.wikipedia.org/w/index.php?title=Electroencephalography&oldid=1136968000 [Accessed February 16, 2023].

Anon (2023b) Functional near-infrared spectroscopy. Wikipedia Available at: https://en.wikipedia.org/w/index.php?title=Functional_near-infrared_spectroscopy&oldid=1136370732 [Accessed February 17, 2023].

Anumanchipalli GK, Chartier J, Chang EF (2019) Speech synthesis from neural decoding of spoken sentences. Nature 568:493–498.

Arcaro MJ, Pinsk MA, Li X, Kastner S (2011) Visuotopic organization of macaque posterior parietal cortex: A functional magnetic resonance imaging study. J Neurosci 31:2064–2078.

Armenta Salas M, Bashford L, Kellis S, Jafari M, Jo H, Kramer D, Shanfield K, Pejsa K, Lee B, Liu CY, Andersen RA (2018) Proprioceptive and cutaneous sensations in humans elicited by intracortical microstimulation Romo R, ed. eLife 7:e32904.

Armour BS, Courtney-Long EA, Fox MH, Fredine H, Cahill A (2016) Prevalence and causes of paralysis—united states, 2013. Am J Public Health 106:1855–1857.

Aron AR, Poldrack RA (2006) Cortical and subcortical contributions to stop signal response inhibition: Role of the subthalamic nucleus. J Neurosci 26:2424–2433.

Ashayeri K, M Jackson E, Huang J, Brem H, Gordon CR (2016) Syndrome of the Trephined: A Systematic Review. Neurosurgery 79:525–534.

Ashby FG (2019) Statistical Analysis of fMRI Data, Second edition. Cambridge, MA: The MIT Press.

Attwell D, Buchan AM, Charpak S, Lauritzen M, Macvicar BA, Newman EA (2010) Glial and neuronal control of brain blood flow. Nature 468:232–243.

Aydin A-K, Haselden WD, Goulam Houssen Y, Pouzat C, Rungta RL, Demené C, Tanter M, Drew PJ, Charpak S, Boido D (2020) Transfer functions linking neural calcium to single voxel functional ultrasound signal. Nat Commun 11:2954.

Baldauf D, Cui H, Andersen RA (2008) The posterior parietal cortex encodes in parallel both goals for double-reach sequences. J Neurosci 28:10081–10089.

Bálint R (1909) Seelenlähmung des "Schauens", optische Ataxie, räumliche Störung der Aufmerksamkeit. Eur Neurol 25:51–66.

Ban HY et al. (2022) Kernel Flow: A high channel count scalable time-domain functional near-infrared spectroscopy system. J Biomed Opt 27:074710.

Bao P, She L, McGill M, Tsao DY (2020) A map of object space in primate inferotemporal cortex. Nature:1–6.

Barash S, Bracewell RM, Fogassi L, Gnadt JW, Andersen RA (1991) Saccade-related activity in the lateral intraparietal area. II. Spatial properties. J Neurophysiol 66:1109–1124.

Beauchamp MS, Oswalt D, Sun P, Foster BL, Magnotti JF, Niketeghad S, Pouratian N, Bosking WH, Yoshor D (2020) Dynamic stimulation of visual cortex produces form vision in sighted and blind humans. Cell 181:774-783.e5.

Ben Hamed S, Duhamel J-R, Bremmer F, Graf W (2001) Representation of the visual field in the lateral intraparietal area of macaque monkeys: A quantitative receptive field analysis. Exp Brain Res 140:127–144.

Benabid AL et al. (2019) An exoskeleton controlled by an epidural wireless brain-machine interface in a tetraplegic patient: A proof-of-concept demonstration. Lancet Neurol 18:1112–1122.

Bergel A, Deffieux T, Demené C, Tanter M, Cohen I (2018) Local hippocampal fast gamma rhythms precede brain-wide hyperemic patterns during spontaneous rodent REM sleep. Nat Commun 9:5364.

Berger M, Agha NS, Gail A (2020) Wireless recording from unrestrained monkeys reveals motor goal encoding beyond immediate reach in frontoparietal cortex Gold JI, Pesaran B, Santacruz SR, eds. eLife 9:e51322.

Bergfeld IO, Mantione M, Hoogendoorn MLC, Ruhé HG, Notten P, van Laarhoven J, Visser I, Figee M, de Kwaasteniet BP, Horst F, Schene AH, van den Munckhof P, Beute G, Schuurman R, Denys D (2016)

Deep brain stimulation of the ventral anterior limb of the internal capsule for treatment-resistant depression: a randomized clinical trial. JAMA Psychiatry 73:456–464.

Berthon B, Bergel A, Matei M, Tanter M (2023) Decoding behavior from global cerebrovascular activity using neural networks. Sci Rep 13:3541.

Bimbard C, Demene C, Girard C, Radtke-Schuller S, Shamma S, Tanter M, Boubenec Y (2018) Multi-scale mapping along the auditory hierarchy using high-resolution functional UltraSound in the awake ferret King AJ, ed. eLife 7:e35028.

Bjånes DA, Bashford L, Pejsa K, Lee B, Liu CY, Andersen RA (2022) Multi-channel intra-cortical micro-stimulation yields quick reaction times and evokes natural somatosensations in a human participant. medRxiv Available at: http://medrxiv.org/lookup/doi/10.1101/2022.08.08.22278389 [Accessed February 17, 2023].

Blaize K, Arcizet F, Gesnik M, Ahnine H, Ferrari U, Deffieux T, Pouget P, Chavane F, Fink M, Sahel J-A, Tanter M, Picaud S (2020) Functional ultrasound imaging of deep visual cortex in awake nonhuman primates. Proc Natl Acad Sci USA 117:14453–14463.

Blatt GJ, Andersen RA, Stoner GR (1990) Visual receptive field organization and cortico-cortical connections of the lateral intraparietal area (area LIP) in the macaque. J Comp Neurol 299:421–445.

Bode S, Haynes J-D (2009) Decoding sequential stages of task preparation in the human brain. NeuroImage 45:606–613.

Boido D, Rungta RL, Osmanski B-F, Roche M, Tsurugizawa T, Le Bihan D, Ciobanu L, Charpak S (2019) Mesoscopic and microscopic imaging of sensory responses in the same animal. Nat Commun 10.

Bokil HS, Pesaran B, Andersen RA, Mitra PP (2006) A method for detection and classification of events in neural activity. IEEE Trans Biomed Eng 53:1678–1687.

Bollimunta A, Totten D, Ditterich J (2012) Neural dynamics of choice: Single-trial analysis of decision-related activity in parietal cortex. J Neurosci 32:12684–12701.

Boucsein M (2022) napari-medical-image-formats: A plugin in order to read medical image formats such as DICOM and NIfTI. Available at: https://github.com/MBPhys/napari-medical-image-formats [Accessed February 13, 2023].

Bourgeais-Rambur L, Beynac L, Mariani J-C, Tanter M, Deffieux T, Lenkei Z, Villanueva L (2022) Altered cortical trigeminal fields excitability by spreading depolarization revealed with in vivo functional ultrasound imaging combined with electrophysiology. J Neurosci 42:6295–6308.

Bouthour W, Mégevand P, Donoghue J, Lüscher C, Birbaumer N, Krack P (2019) Biomarkers for closed-loop deep brain stimulation in Parkinson disease and beyond. Nat Rev Neurol 15:343–352.

Boynton GM, Engel SA, Glover GH, Heeger DJ (1996) Linear systems analysis of functional magnetic resonance imaging in human V1. J Neurosci 16:4207–4221.

Braver TS, Reynolds JR, Donaldson DI (2003) Neural mechanisms of transient and sustained cognitive control during task switching. Neuron 39:713–726.

British Medical Ultrasound Society (2010) Guidelines for the safe use of diagnostic ultrasound equipment. Ultrasound 18:52–59.

Brunner C, Grillet M, Sans-Dublanc A, Farrow K, Lambert T, Macé E, Montaldo G, Urban A (2020) A Platform for Brain-wide Volumetric Functional Ultrasound Imaging and Analysis of Circuit Dynamics in Awake Mice. Neuron 108:861-875.e7.

Brunner C, Grillet M, Urban A, Roska B, Montaldo G, Macé E (2021) Whole-brain functional ultrasound imaging in awake head-fixed mice. Nat Protoc 16:3547–3571.

Buchwald M, Przybylski Ł, Króliczak G (2018) Decoding brain states for planning functional grasps of tools: a functional magnetic resonance imaging multivoxel pattern analysis study. J Int Neuropsychol Soc 24:1013–1025.

Bullard AJ, Hutchison BC, Lee J, Chestek CA, Patil PG (2020) Estimating risk for future intracranial, fully implanted, modular neuroprosthetic systems: a systematic review of hardware complications in clinical deep brain stimulation and experimental human intracortical arrays. Neuromodulation 23:411–426.

Bundy DT, Zellmer E, Gaona CM, Sharma M, Szrama N, Hacker C, Freudenburg ZV, Daitch A, Moran DW, Leuthardt EC (2014) Characterization of the effects of the human dura on macro- and micro-electrocorticographic recordings. J Neural Eng 11:016006.

Butler RA (1953) Discrimination learning by rhesus monkeys to visual-exploration motivation. J Comp Physiol Psychol 46:95–98.

Buzsáki G, Anastassiou CA, Koch C (2012) The origin of extracellular fields and currents — EEG, ECoG, LFP and spikes. Nat Rev Neurosci 13:407–420.

Calabrese E, Badea A, Coe CL, Lubach GR, Shi Y, Styner MA, Johnson GA (2015) A diffusion tensor MRI atlas of the postmortem rhesus macaque brain. NeuroImage 117:408–416.

Callier T, Brantly NW, Caravelli A, Bensmaia SJ (2020) The frequency of cortical microstimulation shapes artificial touch. Proc Natl Acad Sci USA 117:1191–1200.

Campos M, Breznen B, Andersen RA (2010) A neural representation of sequential states within an instructed task. J Neurophysiol 104:2831–2849.

Cardinale F, Cossu M, Castana L, Casaceli G, Schiariti MP, Miserocchi A, Fuschillo D, Moscato A, Caborni C, Arnulfo G, Lo Russo G (2013) Stereoelectroencephalography: Surgical methodology, safety, and stereotactic application accuracy in 500 procedures. Neurosurgery 72:353–366.

Carrizosa J (2022) Transcranial Doppler (TCD/TCCS) Approaches: Acoustic Windows. In: Neurosonology in Critical Care : Monitoring the Neurological Impact of the Critical Pathology (Rodríguez CN, Baracchini C, Mejia-Mantilla JH, Czosnyka M, Suarez JI, Csiba L, Puppo C, Bartels E, eds), pp 177–194. Cham: Springer International Publishing. Available at: https://doi.org/10.1007/978-3-030-81419-9_10 [Accessed March 17, 2023].

Chang SWC, Papadimitriou C, Snyder LH (2009) Using a compound gain field to compute a reach plan. Neuron 64:744–755.

Chang SWC, Snyder LH (2012) The representations of reach endpoints in posterior parietal cortex depend on which hand does the reaching. J Neurophysiol 107:2352–2365.

Chassoux F, Navarro V, Catenoix H, Valton L, Vignal J-P (2018) Planning and management of SEEG. Neurophysiol Clin 48:25–37.

Chen G, Taylor PA, Cox RW (2017) Is the statistic value all we should care about in neuroimaging? NeuroImage 147:952–959.

Chen X, Wang F, Fernandez E, Roelfsema PR (2020) Shape perception via a high-channel-count neuroprosthesis in monkey visual cortex. Science 370:1191–1196.

Chen Y, Namburi P, Elliott LT, Heinzle J, Soon CS, Chee MWL, Haynes J-D (2011) Cortical surface-based searchlight decoding. NeuroImage 56:582–592.

Christopoulos V, Bonaiuto J, Andersen RA (2015) A biologically plausible computational theory for value integration and action selection in decisions with competing alternatives Körding K, ed. PLoS Comput Biol 11:e1004104.

Chung JE, Sellers KK, Leonard MK, Gwilliams L, Xu D, Dougherty ME, Kharazia V, Metzger SL, Welkenhuysen M, Dutta B, Chang EF (2022) High-density single-unit human cortical recordings using the Neuropixels probe. Neuron 110:2409-2421.e3.

Churchland MM, Cunningham JP, Kaufman MT, Foster JD, Nuyujukian P, Ryu SI, Shenoy KV (2012) Neural population dynamics during reaching. Nature 487:51–56.

Churchland MM, Cunningham JP, Kaufman MT, Ryu SI, Shenoy KV (2010) Cortical preparatory activity: Representation of movement or first cog in a dynamical machine? Neuron 68:387–400.

Churchland MM, Shenoy KV (2007) Temporal complexity and heterogeneity of single-neuron activity in premotor and motor cortex. J Neurophysiol 97:4235–4257.

Cohen YE, Andersen RA (2002) A common reference frame for movement plans in the posterior parietal cortex. Nat Rev Neurosci 3:553–562.

Colby CL, Duhamel J-R (1996) Spatial representations for action in parietal cortex. Cognitive Brain Research 5:105–115.

Colby CL, Duhamel J-R, Goldberg ME (1995) Oculocentric spatial representation in parietal cortex. Cerebral Cortex 5:470–481.

Colby CL, Duhamel JR, Goldberg ME (1996) Visual, presaccadic, and cognitive activation of single neurons in monkey lateral intraparietal area. J Neurophysiol 76:2841–2852.

Colby CL, Goldberg ME (1999) Space and attention in parietal cortex. Ann Rev Neurosci 22:319–349.

Collinger JL, Wodlinger B, Downey JE, Wang W, Tyler-Kabara EC, Weber DJ, McMorland AJ, Velliste M, Boninger ML, Schwartz AB (2013) High-performance neuroprosthetic control by an individual with tetraplegia. The Lancet 381:557–564.

Côté SL, Elgbeili G, Quessy S, Dancause N (2020) Modulatory effects of the supplementary motor area on primary motor cortex outputs. J Neurophysiol 123:407–419.

Coyle SM, Ward TE, Markham CM (2007) Brain computer interface using a simplified functional near-infrared spectroscopy system. J Neural Eng 4:219–226.

Crone EA, Wendelken C, Donohue SE, Bunge SA (2006) Neural evidence for dissociable components of task-switching. Cereb Cortex 16:475–486.

Cui H, Andersen RA (2007) Posterior parietal cortex encodes autonomously selected motor plans. Neuron 56:552–559.

Darmani G, Bergmann TO, Butts Pauly K, Caskey CF, de Lecea L, Fomenko A, Fouragnan E, Legon W, Murphy KR, Nandi T, Phipps MA, Pinton G, Ramezanpour H, Sallet J, Yaakub SN, Yoo SS, Chen R (2022) Non-invasive transcranial ultrasound stimulation for neuromodulation. Clin Neurophysiol 135:51–73.

Das K, Nenadic Z (2008) Approximate information discriminant analysis: A computationally simple heteroscedastic feature extraction technique. Pattern Recognit 41:1548–1557.

Das K, Nenadic Z (2009) An efficient discriminant-based solution for small sample size problem. Pattern Recognit 42:857–866.

Das K, Osechinskiy S, Nenadic Z (2007) A Classwise PCA-based Recognition of Neural Data for Brain-Computer Interfaces. In: 2007 29th Annual International Conference of the IEEE Engineering in Medicine and Biology Society, pp 6519–6522. Lyon, France: IEEE. Available at: http://ieeexplore.ieee.org/document/4353853/ [Accessed February 4, 2020].

Dattani S, Ritchie H, Roser M (2021) Mental Health. Our World in Data Available at: https://ourworldindata.org/mental-health [Accessed March 3, 2023].

de Guise E, Gosselin N, Leblanc J, Champoux M-C, Couturier C, Lamoureux J, Dagher J, Marcoux J, Maleki M, Feyz M (2011) Clock drawing and mini-mental state examination in patients with traumatic brain injury. Appl Neuropsychol 18:179–190.

Deffieux T, Demene C, Pernot M, Tanter M (2018) Functional ultrasound neuroimaging: A review of the preclinical and clinical state of the art. Curr Opin Neurobiol 50:128–135.

Degenhart AD, Bishop WE, Oby ER, Tyler-Kabara EC, Chase SM, Batista AP, Yu BM (2020) Stabilization of a brain–computer interface via the alignment of low-dimensional spaces of neural activity. Nat Biomed Eng 4:672–685.

Delaloye S, Holtzheimer PE (2014) Deep brain stimulation in the treatment of depression. Dialogues Clin Neurosci 16:83–91.

Demene C, Baranger J, Bernal M, Delanoe C, Auvin S, Biran V, Alison M, Mairesse J, Harribaud E, Pernot M, Tanter M, Baud O (2017) Functional ultrasound imaging of brain activity in human newborns. Sci Transl Med 9:eaah6756.

Demene C, Bernal M, Delanoe C, Auvin S, Biran V, Alison M, Mairesse J, Harribaud E, Pernot M, Tanter M, Baud O (2016) Functional ultrasound imaging of the brain activity in human neonates. In: 2016 IEEE International Ultrasonics Symposium (IUS), pp 1–3.

Demené C, Deffieux T, Pernot M, Osmanski B-F, Biran V, Gennisson J-L, Sieu L-A, Bergel A, Franqui S, Correas J-M (2015) Spatiotemporal clutter filtering of ultrafast ultrasound data highly increases Doppler and fUltrasound sensitivity. IEEE Trans Med Imaging 34:2271–2285.

Demené C, Maresca D, Kohlhauer M, Lidouren F, Micheau P, Ghaleb B, Pernot M, Tissier R, Tanter M (2018) Multi-parametric functional ultrasound imaging of cerebral hemodynamics in a cardiopulmonary resuscitation model. Sci Rep 8:16436.

Demené C, Tiran E, Sieu L-A, Bergel A, Gennisson JL, Pernot M, Deffieux T, Cohen I, Tanter M (2016) 4D microvascular imaging based on ultrafast Doppler tomography. NeuroImage 127:472–483.

Diomedi S, Vaccari FE, Galletti C, Hadjidimitrakis K, Fattori P (2021) Motor-like neural dynamics in two parietal areas during arm reaching. Prog Neurobiol 205:102116.

Diomedi S, Vaccari FE, Hadjidimitrakis K, Fattori P (2022) Using HMM to model neural dynamics and decode useful signals for neuroprosthetic control. In: Hidden Markov Models and Applications (Bouguila N, Fan W, Amayri M, eds), pp 59–79 Unsupervised and Semi-Supervised Learning. Cham: Springer International Publishing. Available at: https://doi.org/10.1007/978-3-030-99142-5_3 [Accessed March 3, 2023].

Dizeux A, Gesnik M, Ahnine H, Blaize K, Arcizet F, Picaud S, Sahel J-A, Deffieux T, Pouget P, Tanter M (2019) Functional ultrasound imaging of the brain reveals propagation of task-related brain activity in behaving primates. Nat Commun 10:1400.

Dorris MC, Glimcher PW (2004) Activity in posterior parietal cortex is correlated with the relative subjective desirability of action. Neuron 44:365–378.

Dotson NM, Hoffman SJ, Goodell B, Gray CM (2017) A large-scale semi-chronic microdrive recording system for non-human primates. Neuron 96:769-782.e2.

Dougherty DD et al. (2015) A randomized sham-controlled trial of deep brain stimulation of the ventral capsule/ventral striatum for chronic treatment-resistant depression. Biol Psychiatry 78:240–248.

Downey JE, Schwed N, Chase SM, Schwartz AB, Collinger JL (2018) Intracortical recording stability in human brain-computer interface users. J Neural Eng 15:046016.

Drew L (2023) Decoding the business of brain–computer interfaces. Nat Electron 6:90–95.

Dumoulin SO, Fracasso A, van der Zwaag W, Siero JCW, Petridou N (2018) Ultra-high field MRI: Advancing systems neuroscience towards mesoscopic human brain function. NeuroImage 168:345–357.

Duschek S, Schandry R (2003) Functional transcranial Doppler sonography as a tool in psychophysiological research. Psychophysiology 40:436–454.

Dyer EL, Gheshlaghi Azar M, Perich MG, Fernandes HL, Naufel S, Miller LE, Körding KP (2017) A cryptography-based approach for movement decoding. Nat Biomed Eng 1:967–976.

Ebbesen CL, Brecht M (2017) Motor cortex — to act or not to act? Nat Rev Neurosci 18:694–705.

Eklund A, Nichols TE, Knutsson H (2016) Cluster failure: Why fMRI inferences for spatial extent have inflated false-positive rates. Proc Natl Acad Sci USA 113:7900–7905.

Espinoza RT, Kellner CH (2022) Electroconvulsive therapy. N Engl J Med 386:667–672.

Faress A, Chau T (2013) Towards a multimodal brain–computer interface: Combining fNIRS and fTCD measurements to enable higher classification accuracy. NeuroImage 77:186–194.

Fifer MS, McMullen DP, Osborn LE, Thomas TM, Christie B, Nickl RW, Candrea DN, Pohlmeyer EA, Thompson MC, Anaya MA, Schellekens W, Ramsey NF, Bensmaia SJ, Anderson WS, Wester BA, Crone NE, Celnik PA, Cantarero GL, Tenore FV (2022) Intracortical somatosensory stimulation to elicit fingertip sensations in an individual with spinal cord injury. Neurology 98:e679–e687.

Fleming JFR, Crosby EC (1955) The parietal lobe as an additional motor area; The motor effects of electrical stimulation and ablation of cortical areas 5 and 7 in monkeys. J Comp Neurol 103:485–512.

Flesher SN, Collinger JL, Foldes ST, Weiss JM, Downey JE, Tyler-Kabara EC, Bensmaia SJ, Schwartz AB, Boninger ML, Gaunt RA (2016) Intracortical microstimulation of human somatosensory cortex. Sci Transl Med 8:361ra141-361ra141.

Flesher SN, Downey JE, Weiss JM, Hughes CL, Herrera AJ, Tyler-Kabara EC, Boninger ML, Collinger JL, Gaunt RA (2021) A brain-computer interface that evokes tactile sensations improves robotic arm control. Science 372:831-+.

Foley NC, Jangraw DC, Peck C, Gottlieb J (2014) Novelty enhances visual salience independently of reward in the parietal lobe. J Neurosci 34:7947–7957.

Foley NC, Kelly SP, Mhatre H, Lopes M, Gottlieb J (2017) Parietal neurons encode expected gains in instrumental information. Proc Natl Acad Sci USA 114:E3315–E3323.

Freedman DJ, Assad JA (2006) Experience-dependent representation of visual categories in parietal cortex. Nature 443:85–88.

Fried I, MacDonald KA, Wilson CL (1997) Single neuron activity in human hippocampus and amygdala during recognition of faces and objects. Neuron 18:753–765.

Fried I, Wilson CL, Maidment NT, Engel J, Behnke E, Fields TA, MacDonald KA, Morrow JW, Ackerson L (1999) Cerebral microdialysis combined with single-neuron and electroencephalographic recording in neurosurgical patients. Technical note. J Neurosurg 91:697–705.

Gallivan JP, Chapman CS, Wolpert DM, Flanagan JR (2018) Decision-making in sensorimotor control. Nat Rev Neurosci 19:519–534.

Gallivan JP, McLean DA, Valyear KF, Culham JC (2013) Decoding the neural mechanisms of human tool use Angelaki D, ed. eLife 2:e00425.

Garcea FE, Buxbaum LJ (2019) Gesturing tool use and tool transport actions modulates inferior parietal functional connectivity with the dorsal and ventral object processing pathways. Hum Brain Mapp 40:2867–2883.

Georges A, M Das J (2023) Traumatic Brain Injury. In: StatPearls. Treasure Island (FL): StatPearls Publishing. Available at: http://www.ncbi.nlm.nih.gov/books/NBK459300/ [Accessed April 21, 2023].

Ghazizadeh A, Fakharian MA, Amini A, Griggs W, Leopold DA, Hikosaka O (2020) Brain networks sensitive to object novelty, value, and their combination. Cereb Cortex Comm.

Ghazizadeh A, Griggs W, Hikosaka O (2016) Ecological origins of object salience: Reward, uncertainty, aversiveness, and novelty. Frontiers in Neuroscience 10 Available at: https://doi.org/10.3389%2Ffnins.2016.00378 [Accessed February 24, 2019].

Ghazizadeh A, Griggs W, Leopold DA, Hikosaka O (2018) Temporal–prefrontal cortical network for discrimination of valuable objects in long-term memory. Proc Natl Acad Sci USA 115:E2135–E2144.

Glickfeld LL, Andermann ML, Bonin V, Reid RC (2013) Cortico-cortical projections in mouse visual cortex are functionally target specific. Nat Neurosci 16:219–226.

Glimcher PW, Ciaramitaro VM, Platt ML, Bayer HM, Brown MA, Handel A (2001) Application of neurosonography to experimental physiology. J Neurosci Methods 108:131–144.

Gnadt JW, Andersen RA (1988) Memory related motor planning activity in posterior parietal cortex of macaque. Exp Brain Res:5.

Goense J, Bohraus Y, Logothetis NK (2016) fMRI at high spatial resolution: Implications for BOLD-models. Front Comput Neurosci 10.

Goense JBM, Logothetis NK (2008) Neurophysiology of the BOLD fMRI signal in awake monkeys. Curr Biol 18:631–640.

Gopinath K, Krishnamurthy V, Lacey S, Sathian K (2018a) Accounting for non-gaussian sources of spatial correlation in parametric functional magnetic resonance imaging paradigms II: A method to obtain first-level analysis residuals with uniform and gaussian spatial autocorrelation function and independent and identically distributed time-series. Brain Connect 8:10–21.

Gopinath K, Krishnamurthy V, Sathian K (2018b) Accounting for non-gaussian sources of spatial correlation in parametric functional magnetic resonance imaging paradigms I: Revisiting cluster-based inferences. Brain Connect 8:1–9.

Gottlieb J, Snyder LH (2010) Spatial and non-spatial functions of the parietal cortex. Curr Opin Neurobiol 20:731–740.

Griggs WS, Norman SL, Deffieux T, Segura F, Osmanski B-F, Chau G, Christopoulos V, Liu C, Tanter M, Shapiro MG, Andersen RA (2022) Decoding motor plans using a closed-loop ultrasonic brain-machine interface. bioRxiv:2022.11.10.515371 Available at: https://www.biorxiv.org/content/10.1101/2022.11.10.515371v1 [Accessed November 23, 2022].

Guan C, Aflalo T, Kadlec K, Leon JG de, Rosario ER, Bari A, Pouratian N, Andersen RA (2022a) Compositional coding of individual finger movements in human posterior parietal cortex and motor cortex enables ten-finger decoding. medRxiv:2022.12.07.22283227 Available at: https://www.medrxiv.org/content/10.1101/2022.12.07.22283227v1 [Accessed March 8, 2023].

Guan C, Aflalo T, Zhang CY, Amoruso E, Rosario ER, Pouratian N, Andersen RA (2022b) Stability of motor representations after paralysis. eLife 11:e74478.

Güresir E, Schuss P, Vatter H, Raabe A, Seifert V, Beck J (2009) Decompressive craniectomy in subarachnoid hemorrhage. Neurosurg Focus 26:E4.

Hader WJ, Tellez-Zenteno J, Metcalfe A, Hernandez-Ronquillo L, Wiebe S, Kwon C-S, Jette N (2013) Complications of epilepsy surgery—A systematic review of focal surgical resections and invasive EEG monitoring. Epilepsia 54:840–847.

Hadjidimitrakis K, Bakola S, Wong YT, Hagan MA (2019) Mixed spatial and movement representations in the primate posterior parietal cortex. Front Neural Circuits 13.

Han C, O'Sullivan J, Luo Y, Herrero J, Mehta AD, Mesgarani N (2019) Speaker-independent auditory attention decoding without access to clean speech sources. Sci Adv 5:eaav6134.

Hauschild M, Mulliken GH, Fineman I, Loeb GE, Andersen RA (2012) Cognitive signals for brain–machine interfaces in posterior parietal cortex include continuous 3D trajectory commands. Proc Natl Acad Sci USA 109:17075–17080.

Heider B, Nathanson JL, Isacoff EY, Callaway EM, Siegel RM (2010) Two-photon imaging of calcium in virally transfected striate cortical neurons of behaving monkey Lowenstein PR, ed. PLoS ONE 5:e13829.

Herff C, Krusienski DJ, Kubben P (2020) The potential of stereotactic-EEG for brain-computer interfaces: Current progress and future directions. Frontiers in Neuroscience 14.

Hikosaka O, Yamamoto S, Yasuda M, Kim HF (2013) Why skill matters. Trends Cogn Sci 17:434–441.

Hillman EMC (2014) Coupling mechanism and significance of the BOLD signal: A status report. Ann Rev Neurosci 37:161–181.

Hochberg LR, Serruya MD, Friehs GM, Mukand JA, Saleh M, Caplan AH, Branner A, Chen D, Penn RD, Donoghue JP (2006) Neuronal ensemble control of prosthetic devices by a human with tetraplegia. Nature 442:164–171.

Hoff MN, McKinney A, Shellock FG, Rassner U, Gilk T, Watson RE, Greenberg TD, Froelich J, Kanal E (2019) Safety considerations of 7-T MRI in clinical practice. Radiology 292:509–518.

Holsapple J, Preston J, Strick P (1991) The origin of thalamic inputs to the "hand" representation in the primary motor cortex. J Neurosci 11:2644–2654.

Holtzheimer PE et al. (2017) Subcallosal cingulate deep brain stimulation for treatment-resistant depression: A multisite, randomised, sham-controlled trial. The Lancet Psychiatry 4:839–849.

Horan M, Daddaoua N, Gottlieb J (2019) Parietal neurons encode information sampling based on decision uncertainty. Nat Neurosci:1.

Hosp JA, Molina-Luna K, Hertler B, Atiemo CO, Stett A, Luft AR (2008) Thin-film epidural microelectrode arrays for somatosensory and motor cortex mapping in rat. J Neurosci Methods 172:255–262.

Huang D, Lin P, Fei D-Y, Chen X, Bai O (2009) Decoding human motor activity from EEG single trials for a discrete two-dimensional cursor control. J Neural Eng 6:046005.

Huber L, Goense J, Kennerley AJ, Trampel R, Guidi M, Reimer E, Ivanov D, Neef N, Gauthier CJ, Turner R, Möller HE (2015) Cortical lamina-dependent blood volume changes in human brain at 7T. NeuroImage 107:23–33.

Hudson N, Burdick JW (2007) Learning hybrid system models for supervisory decoding of discrete state, with applications to the parietal reach region. In: 2007 3rd International IEEE/EMBS Conference on Neural Engineering, pp 587–592.

Hwang EJ, Andersen RA (2009) Brain control of movement execution onset using local field potentials in posterior parietal cortex. J Neurosci 29:14363–14370.

Hyvarinen J (1981) Regional distribution of functions in parietal association area 7 of the monkey. Brain Res 206:287–303.

Iaccarino C, Kolias AG, Roumy L-G, Fountas K, Adeleye AO (2020) Cranioplasty following decompressive craniectomy. Front Neurol 10:1357.

Iadecola C (2017) The neurovascular unit coming of age: a journey through neurovascular coupling in health and disease. Neuron 96:17–42.

Ibbotson M, Krekelberg B (2011) Visual perception and saccadic eye movements. Curr Opin Neurobiol 21:553–558.

Imbault M, Chauvet D, Gennisson J-L, Capelle L, Tanter M (2017) Intraoperative functional ultrasound imaging of human brain activity. Sci Rep 7:7304.

Insel TR (2014) The NIMH Research Domain Criteria (RDoC) Project: Precision medicine for psychiatry. Am J Psychiatry 171:395–397.

Institute of Health Metrics and Evaluation (2019) Global Health Data Exchange (GHDx). Available at: https://vizhub.healthdata.org/gbd-results [Accessed August 12, 2022].

Iyer A, Lindner A, Kagan I, Andersen RA (2010) Motor preparatory activity in posterior parietal cortex is modulated by subjective absolute value. PLOS Biology 8:e1000444.

Jaegle A, Mehrpour V, Rust N (2019) Visual novelty, curiosity, and intrinsic reward in machine learning and the brain. Curr Opin Neurobiol 58:167–174.

John SE, Opie NL, Wong YT, Rind GS, Ronayne SM, Gerboni G, Bauquier SH, O'Brien TJ, May CN, Grayden DB, Oxley TJ (2018) Signal quality of simultaneously recorded endovascular, subdural and epidural signals are comparable. Sci Rep 8:8427.

Johnston WA, Hawley KJ, Plewe SH, Elliott JMG, DeWitt MJ (1990) Attention capture by novel stimuli. J Exp Psychol 119:397–411.

Kagan I, Iyer A, Lindner A, Andersen RA (2010) Space representation for eye movements is more contralateral in monkeys than in humans. Proc Natl Acad Sci USA 107:7933–7938.

Kao JC, Nuyujukian P, Ryu SI, Shenoy KV (2017a) A high-performance neural prosthesis incorporating discrete state selection with hidden Markov models. IEEE Trans Biomed 64:935–945.

Kao JC, Ryu SI, Shenoy KV (2017b) Leveraging neural dynamics to extend functional lifetime of brain-machine interfaces. Sci Rep 7:7395.

Kaplan L, Chow BW, Gu C (2020) Neuronal regulation of the blood–brain barrier and neurovascular coupling. Nat Rev Neurosci:1–17.

Kawakami R, Sawada K, Sato A, Hibi T, Kozawa Y, Sato S, Yokoyama H, Nemoto T (2013) Visualizing hippocampal neurons with in vivo two-photon microscopy using a 1030 nm picosecond pulse laser. Sci Rep 3:1014.

Kellis S, Sorensen L, Darvas F, Sayres C, O'Neill K, Brown RB, House P, Ojemann J, Greger B (2016) Multi-scale analysis of neural activity in humans: Implications for micro-scale electrocorticography. Clin Neurophysiol 127:591–601.

Kemere C, Santhanam G, Yu BM, Afshar A, Ryu SI, Meng TH, Shenoy KV (2008) Detecting neural-state transitions using hidden Markov models for motor cortical prostheses. J Neurophysiol 100:2441–2452.

Khalaf A, Sybeldon M, Sejdic E, Akcakaya M (2018) A brain-computer interface based on functional transcranial Doppler ultrasound using wavelet transform and support vector machines. J Neurosci Methods 293:174–182.

Khodagholy D, Gelinas JN, Thesen T, Doyle W, Devinsky O, Malliaras GG, Buzsáki G (2015) NeuroGrid: recording action potentials from the surface of the brain. Nat Neurosci 18:310–315.

Khodagholy D, Gelinas JN, Zhao Z, Yeh M, Long M, Greenlee JD, Doyle W, Devinsky O, Buzsáki G (2016) Organic electronics for high-resolution electrocorticography of the human brain. Sci Adv 2:e1601027.

Klaes C, Kellis S, Aflalo T, Lee B, Pejsa K, Shanfield K, Hayes-Jackson S, Aisen M, Heck C, Liu C, Andersen RA (2015) Hand shape representations in the human posterior parietal cortex. J Neurosci 35:15466–15476.

Klaus A, Alves da Silva J, Costa RM (2019) What, if, and when to move: Basal ganglia circuits and self-paced action initiation. Ann Rev Neurosci 42:459–483.

Knöpfel T, Song C (2019) Optical voltage imaging in neurons: Moving from technology development to practical tool. Nat Rev Neurosci 20:719–727.

Konerding WS, Froriep UP, Kral A, Baumhoff P (2018) New thin-film surface electrode array enables brain mapping with high spatial acuity in rodents. Sci Rep 8:3825.

Korinek AM (1997) Risk factors for neurosurgical site infections after craniotomy: A prospective multicenter study of 2944 patients. The French Study Group of Neurosurgical Infections, the SEHP, and the C-CLIN Paris-Nord. Service Epidémiologie Hygiène et Prévention. Neurosurgery 41:1073–1079; discussion 1079-1081.

Kozai TDY, Jaquins-Gerstl AS, Vazquez AL, Michael AC, Cui XT (2015) Brain tissue responses to neural implants impact signal sensitivity and intervention strategies. ACS Chem Neurosci 6:48–67.

Lacquaniti F, Guigon E, Bianchi L, Ferraina S, Caminiti R (1995) Representing spatial information for limb movement: Role of area 5 in the monkey. Cereb Cortex 5:391–409.

Lauer J, Zhou M, Ye S, Menegas W, Schneider S, Nath T, Rahman MM, Di Santo V, Soberanes D, Feng G, Murthy VN, Lauder G, Dulac C, Mathis MW, Mathis A (2022) Multi-animal pose estimation, identification and tracking with DeepLabCut. Nat Methods 19:496–504.

Leathers ML, Olson CR (2012) In monkeys making value-based decisions, LIP neurons encode cue salience and not action value. Science 338:132–135.

Li G, Jiang S, Xu Y, Wu Z, Chen L, Zhang D (2017) A preliminary study towards prosthetic hand control using human stereo-electroencephalography (SEEG) signals. In: 2017 8th International IEEE/EMBS Conference on Neural Engineering (NER), pp 375–378. Shanghai, China: IEEE. Available at: http://ieeexplore.ieee.org/document/8008368/ [Accessed March 16, 2023].

Li Y, Cui H (2013) Dorsal parietal area 5 encodes immediate reach in sequential arm movements. J Neurosci 33:14455–14465.

Li Y, Daddaoua N, Horan M, Foley NC, Gottlieb J (2022) Uncertainty modulates visual maps during noninstrumental information demand. Nat Commun 13:5911.

Liu Y, Yttri EA, Snyder LH (2010) Intention and attention: Different functional roles for LIPd and LIPv. Nat Neurosci 13:495–500.

Logothetis NK, Pauls J, Augath M, Trinath T, Oeltermann A (2001) Neurophysiological investigation of the basis of the fMRI signal. Nature 412:150–157.

Loo CK, Alonzo A, Martin D, Mitchell PB, Galvez V, Sachdev P (2012) Transcranial direct current stimulation for depression: 3-week, randomised, sham-controlled trial. Br J Psychiatry 200:52–59.

Lopes da Silva F (2013) EEG and MEG: Relevance to neuroscience. Neuron 80:1112–1128.

Lopes L, Stokes M, 2022 (2022) KFF/CNN Mental Health In America Survey. KFF Available at: https://www.kff.org/other/report/kff-cnn-mental-health-in-america-survey/ [Accessed March 13, 2023].

Louie K, Grattan LE, Glimcher PW (2011) Reward value-based gain control: Divisive normalization in parietal cortex. J Neurosci 31:10627–10639.

Lu J, Mamun KA, Chau T (2015) Pattern classification to optimize the performance of transcranial Doppler ultrasonography-based brain machine interface. Pattern Recognit Lett 66:135–143.

Luppino G, Rizzolatti G (2000) The organization of the frontal motor cortex. Physiology 15:219–224.

Macé E, Montaldo G, Cohen I, Baulac M, Fink M, Tanter M (2011) Functional ultrasound imaging of the brain. Nat Methods 8:662–664.

Macé E, Montaldo G, Osmanski B, Cohen I, Fink M, Tanter M (2013) Functional ultrasound imaging of the brain: Theory and basic principles. IEEE Trans Ultrason Ferroelectr Freq Control 60:492–506.

Macé É, Montaldo G, Trenholm S, Cowan C, Brignall A, Urban A, Roska B (2018) Whole-brain functional ultrasound imaging reveals brain modules for visuomotor integration. Neuron 100:1241-1251.e7.

Mackenzie TN, Bailey AZ, Mi PY, Tsang P, Jones CB, Nelson AJ (2016) Human area 5 modulates corticospinal output during movement preparation. NeuroReport 27:1056–1060.

Makin JG, Moses DA, Chang EF (2020) Machine translation of cortical activity to text with an encoder–decoder framework. Nat Neurosci 23:575–582.

Malmivuo J (2012) Comparison of the properties of EEG and MEG in detecting the electric activity of the brain. Brain Topogr 25:1–19.

Maresca D, Payen T, Lee-Gosselin A, Ling B, Malounda D, Demené C, Tanter M, Shapiro MG (2020) Acoustic biomolecules enhance hemodynamic functional ultrasound imaging of neural activity. NeuroImage 209:116467.

Martin JLR, Martín-Sánchez E (2012) Systematic review and meta-analysis of vagus nerve stimulation in the treatment of depression: variable results based on study designs. Eur Psychiatry 27:147–155.

Masamizu Y, Tanaka YR, Tanaka YH, Hira R, Ohkubo F, Kitamura K, Isomura Y, Okada T, Matsuzaki M (2014) Two distinct layer-specific dynamics of cortical ensembles during learning of a motor task. Nat Neurosci 17:987–994.

Mathis A, Mamidanna P, Cury KM, Abe T, Murthy VN, Mathis MW, Bethge M (2018) DeepLabCut: markerless pose estimation of user-defined body parts with deep learning. Nat Neurosci 21:1281–1289.

Mathis A, Schneider S, Lauer J, Mathis MW (2020) A primer on motion capture with deep learning: Principles, pitfalls, and perspectives. Neuron 108:44–65.

McDowell T, Holmes NP, Sunderland A, Schürmann M (2018) TMS over the supramarginal gyrus delays selection of appropriate grasp orientation during reaching and grasping tools for use. Cortex 103:117–129.

Mellinger J, Schalk G, Braun C, Preissl H, Rosenstiel W, Birbaumer N, Kübler A (2007) An MEG-based brain-computer interface (BCI). NeuroImage 36:581–593.

Metzger SL, Liu JR, Moses DA, Dougherty ME, Seaton MP, Littlejohn KT, Chartier J, Anumanchipalli GK, Tu-Chan A, Ganguly K, Chang EF (2022) Generalizable spelling using a speech neuroprosthesis in an individual with severe limb and vocal paralysis. Nat Commun 13:6510.

Miyashita Y, Higuchi S-I, Sakai K, Masui N (1991) Generation of fractal patterns for probing the visual memory. Neurosci Res 12:307–311.

Mollman HD, Haines SJ (1986) Risk factors for postoperative neurosurgical wound infection. A case-control study. J Neurosurg 64:902–906.

Montaldo G, Urban A, Macé E (2022) Functional ultrasound neuroimaging. Ann Rev Neurosci 45:491–513.

Moreno JA, Mesalles E, Gener J, Tomasa A, Ley A, Roca J, Fernández-Llamazares J (2000) Evaluating the outcome of severe head injury with transcranial Doppler ultrasonography. Neurosurg Focus 8:e8.

Moses DA, Metzger SL, Liu JR, Anumanchipalli GK, Makin JG, Sun PF, Chartier J, Dougherty ME, Liu PM, Abrams GM, Tu-Chan A, Ganguly K, Chang EF (2021) Neuroprosthesis for decoding speech in a paralyzed person with anarthria. N Engl J Med 385:217–227.

Mosso A (1881) Ueber den Kreislauf des Blutes im Menschlichen Gehirn. Leipzig: Verlag von Veit & Comp.

Motter B, Mountcastle V (1981) The functional properties of the light-sensitive neurons of the posterior parietal cortex studied in waking monkeys: Foveal sparing and opponent vector organization. J Neurosci 1:3–26.

Mulliken GH, Musallam S, Andersen RA (2008) Decoding trajectories from posterior parietal cortex ensembles. J Neurosci 28:12913–12926.

Mullin JP, Shriver M, Alomar S, Najm I, Bulacio J, Chauvel P, Gonzalez-Martinez J (2016) Is SEEG safe? A systematic review and meta-analysis of stereo-electroencephalography–related complications. Epilepsia 57:386–401.

Musallam S, Corneil BD, Greger B, Scherberger H, Andersen RA (2004) Cognitive control signals for neural prosthetics. Science 305:258–262.

Myrden AJ, Kushki A, Sejdić E, Guerguerian A-M, Chau T (2011) A brain-computer interface based on bilateral transcranial Doppler ultrasound. PloS One 6:e24170.

Nabors NA, Millis SR, Rosenthal M (1997) Use of the neurobehavioral cognitive status examination (Cognistat) in traumatic brain injury. J Head Trauma Rehabil 12:79–84.

Naseer N, Hong MJ, Hong K-S (2014) Online binary decision decoding using functional near-infrared spectroscopy for the development of brain–computer interface. Exp Brain Res 232:555–564.

Norman SL, Maresca D, Christopoulos VN, Griggs WS, Demene C, Tanter M, Shapiro MG, Andersen RA (2021) Single-trial decoding of movement intentions using functional ultrasound neuroimaging. Neuron.

Norman SL, McFarland DJ, Miner A, Cramer SC, Wolbrecht ET, Wolpaw JR, Reinkensmeyer DJ (2018) Controlling pre-movement sensorimotor rhythm can improve finger extension after stroke. J Neural Eng 15:056026.

Nowlis DP, Kamiya J (1970) The control of electroencephalographic alpha rhythms through auditory feedback and the associated mental activity. Psychophysiology 6:476–484.

Nunez-Elizalde AO, Krumin M, Reddy CB, Montaldo G, Urban A, Harris KD, Carandini M (2022) Neural correlates of blood flow measured by ultrasound. Neuron.

Ogasawara T, Sogukpinar F, Zhang K, Feng Y-Y, Pai J, Jezzini A, Monosov IE (2022) A primate temporal cortex–zona incerta pathway for novelty seeking. Nat Neurosci 25:50–60.

Ogawa S, Lee TM, Kay AR, Tank DW (1990) Brain magnetic resonance imaging with contrast dependent on blood oxygenation. Proc Natl Acad Sci USA 87:9868–9872.

Ohbayashi M, Picard N, Strick PL (2016) Inactivation of the dorsal premotor area disrupts internally generated, but not visually guided, sequential movements. J Neurosci 36:1971–1976.

O'Herron P, Chhatbar PY, Levy M, Shen Z, Schramm AE, Lu Z, Kara P (2016) Neural correlates of single-vessel haemodynamic responses in vivo. Nature 534:378–382.

Op de Beeck HP, DiCarlo JJ, Goense JBM, Grill-Spector K, Papanastassiou A, Tanifuji M, Tsao DY (2008) Fine-scale spatial organization of face and object selectivity in the temporal lobe: Do functional

magnetic resonance imaging, optical imaging, and electrophysiology agree? J Neurosci 28:11796–11801.

Orban GA, Caruana F (2014) The neural basis of human tool use. Front Psychol 5.

O'Shea DJ, Trautmann E, Chandrasekaran C, Stavisky S, Kao JC, Sahani M, Ryu S, Deisseroth K, Shenoy KV (2017) The need for calcium imaging in nonhuman primates: New motor neuroscience and brain-machine interfaces. Exp Neurol 287:437–451.

Oxley TJ et al. (2021) Motor neuroprosthesis implanted with neurointerventional surgery improves capacity for activities of daily living tasks in severe paralysis: first in-human experience. J Neurointerv Surg 13:102–108.

Oxley TJ, Opie NL, Rind GS, Liyanage K, John SE, Ronayne S, McDonald AJ, Dornom A, Lovell TJH, Mitchell PJ, Bennett I, Bauquier S, Warne LN, Steward C, Grayden DB, Desmond P, Davis SM, O'Brien TJ, May CN (2018) An ovine model of cerebral catheter venography for implantation of an endovascular neural interface. J Neurosurg 128:1020–1027.

Pallesen L-P, Barlinn K, Puetz V (2019) Role of decompressive craniectomy in ischemic stroke. Front Neurol 9:1119.

Pandarinath C, Ames KC, Russo AA, Farshchian A, Miller LE, Dyer EL, Kao JC (2018) Latent factors and dynamics in motor cortex and their application to brain–machine interfaces. J Neurosci 38:9390–9401.

Park IM, Meister MLR, Huk AC, Pillow JW (2014) Encoding and decoding in parietal cortex during sensorimotor decision-making. Nat Neurosci 17:1395–1403.

Park J, Shimojo E, Shimojo S (2010) Roles of familiarity and novelty in visual preference judgments are segregated across object categories. Proc Natl Acad Sci U S A 107:14552–14555.

Parvathaneni A, Das JM (2020) Balint Syndrome. In: StatPearls. Treasure Island (FL): StatPearls Publishing. Available at: http://www.ncbi.nlm.nih.gov/books/NBK544347/ [Accessed July 13, 2020].

Patel GH, Kaplan DM, Snyder LH (2014) Topographic organization in the brain: Searching for general principles. Trends Cogn Sci 18:351–363.

Patel GH, Shulman GL, Baker JT, Akbudak E, Snyder AZ, Snyder LH, Corbetta M (2010) Topographic organization of macaque area LIP. Proc Natl Acad Sci USA 107:4728–4733.

Paulk AC, Kfir Y, Khanna AR, Mustroph ML, Trautmann EM, Soper DJ, Stavisky SD, Welkenhuysen M, Dutta B, Shenoy KV, Hochberg LR, Richardson RM, Williams ZM, Cash SS (2022) Large-scale neural recordings with single neuron resolution using Neuropixels probes in human cortex. Nat Neurosci 25:252–263.

Peirce JW (2007) PsychoPy—Psychophysics software in Python. J Neurosci Methods 162:8–13.

Penny WD, Friston KJ, Ashburner JT, Kiebel SJ, Nichols TE eds. (2006) Statistical parametric mapping: The analysis of functional brain images, Illustrated edition. Amsterdam ; Boston: Academic Press.

Pesaran B, Pezaris JS, Sahani M, Mitra PP, Andersen RA (2002) Temporal structure in neuronal activity during working memory in macaque parietal cortex. Nat Neurosci 5:805–811.

Platt ML, Glimcher PW (1997) Responses of intraparietal neurons to saccadic targets and visual distractors. J Neurophysiol 78:1574–1589.

Platt ML, Glimcher PW (1998a) Response fields of intraparietal neurons quantified with multiple saccadic targets. Exp Brain Res 121:65–75.

Platt ML, Glimcher PW (1998b) Response fields of intraparietal neurons quantified with multiple saccadic targets. Exp Brain Res 121:65–75.

Platt ML, Glimcher PW (1999) Neural correlates of decision variables in parietal cortex. Nature 400:233–238.

Pnevmatikakis EA, Giovannucci A (2017) NoRMCorre: An online algorithm for piecewise rigid motion correction of calcium imaging data. J Neurosci Methods 291:83–94.

Potok W, Maskiewicz A, Króliczak G, Marangon M (2019) The temporal involvement of the left supramarginal gyrus in planning functional grasps: A neuronavigated TMS study. Cortex 111:16–34.

Pratt EJ et al. (2021) Kernel Flux: A whole-head 432-magnetometer optically-pumped magnetoencephalography (OP-MEG) system for brain activity imaging during natural human experiences. In: Optical and Quantum Sensing and Precision Metrology, pp 162–179. SPIE.

Purkayastha S, Sorond F (2013) Transcranial doppler ultrasound: Technique and application. Semin Neurol 32:411–420.

Rabut C, Correia M, Finel V, Pezet S, Pernot M, Deffieux T, Tanter M (2019) 4D functional ultrasound imaging of whole-brain activity in rodents. Nat Methods 16:994–997.

Rabut C, Yoo S, Hurt RC, Jin Z, Li H, Guo H, Ling B, Shapiro MG (2020) Ultrasound technologies for imaging and modulating neural activity. Neuron 108:93–110.

Rao P (2020) How to build a neural interface: Lessons from cochlear implants. Available at: https://www.from-the-interface.com/neural-interface-cochlear-implant/ [Accessed February 15, 2023].

Rau R, Kruizinga P, Mastik F, Belau M, de Jong N, Bosch JG, Scheffer W, Maret G (2018) 3D functional ultrasound imaging of pigeons. NeuroImage 183:469–477.

Rosenberg JB, Shiloh AL, Savel RH, Eisen LA (2011) Non-invasive methods of estimating intracranial pressure. Neurocrit Care 15:599–608.

Rowe J, Hughes L, Eckstein D, Owen AM (2008) Rule-selection and action-selection have a shared neuroanatomical basis in the human prefrontal and parietal cortex. Cereb Cortex 18:2275–2285.

Rungta RL, Chaigneau E, Osmanski B-F, Charpak S (2018) Vascular compartmentalization of functional hyperemia from the synapse to the pia. Neuron 99:362-375.e4.

Rush AJ (2023) Unipolar major depression in adults: Choosing initial treatment - UpToDate. Available at: https://www.uptodate.com/contents/unipolar-major-depression-in-adults-choosing-initial-treatment/print [Accessed March 3, 2023].

Rush AJ, Marangell LB, Sackeim HA, George MS, Brannan SK, Davis SM, Howland R, Kling MA, Rittberg BR, Burke WJ, Rapaport MH, Zajecka J, Nierenberg AA, Husain MM, Ginsberg D, Cooke RG (2005) Vagus nerve stimulation for treatment-resistant depression: A randomized, controlled acute phase trial. Biol Psychiatry 58:347–354.

Sadakane O, Masamizu Y, Watakabe A, Terada S-I, Ohtsuka M, Takaji M, Mizukami H, Ozawa K, Kawasaki H, Matsuzaki M, Yamamori T (2015) Long-term two-photon calcium imaging of neuronal populations with subcellular resolution in adult non-human primates. Cell Rep 13:1989–1999.

Sakai J (2022) Functional near-infrared spectroscopy reveals brain activity on the move. Proc Natl Acad Sci USA 119:e2208729119.

Saleem KS (2012) A combined MRI and histology atlas of the rhesus monkey brain: in stereotaxic coordinates. Academic Press.

Sampat MP, Zhou Wang, Gupta S, Bovik AC, Markey MK (2009) Complex wavelet structural similarity: A new image similarity index. IEEE Trans on Image Process 18:2385–2401.

Sauvage J, Flesch M, Férin G, Nguyen-Dinh A, Porée J, Tanter M, Pernot M, Deffieux T (2018) A large aperture row column addressed probe for in vivo 4D ultrafast Doppler ultrasound imaging. Phys Med Biol 63:215012.

Savaki HE, Gregoriou GG, Bakola S, Raos V, Moschovakis AK (2010) The place code of saccade metrics in the lateral bank of the intraparietal sulcus. J Neurosci 30:1118–1127.

Scangos KW, Khambhati AN, Daly PM, Makhoul GS, Sugrue LP, Zamanian H, Liu TX, Rao VR, Sellers KK, Dawes HE, Starr PA, Krystal AD, Chang EF (2021a) Closed-loop neuromodulation in an individual with treatment-resistant depression. Nat Med 27:1696–1700.

Scangos KW, Makhoul GS, Sugrue LP, Chang EF, Krystal AD (2021b) State-dependent responses to intracranial brain stimulation in a patient with depression. Nat Med 27:229–231.

Scheibel RS (2017) Functional magnetic resonance imaging of cognitive control following traumatic brain injury. Front Neurol 8:352.

Schendel AA, Nonte MW, Vokoun C, Richner TJ, Brodnick SK, Atry F, Frye S, Bostrom P, Pashaie R, Thongpang S, Eliceiri KW, Williams JC (2014) The effect of micro-ECoG substrate footprint on the meningeal tissue response. J Neural Eng 11:046011.

Shadlen MN, Newsome WT (2001) Neural basis of a perceptual decision in the parietal cortex (area LIP) of the rhesus monkey. J Neurophysiol 86:1916–1936.

Shanechi MM (2019) Brain–machine interfaces from motor to mood. Nat Neurosci 22:1554–1564.

Shapson-Coe A et al. (2021) A connectomic study of a petascale fragment of human cerebral cortex. :2021.05.29.446289 Available at: https://www.biorxiv.org/content/10.1101/2021.05.29.446289v4 [Accessed August 4, 2022].

Shay T, Mitchell K-A, Belzberg M, Zelko I, Mahapatra S, Qian J, Mendoza L, Huang J, Brem H, Gordon C (2020) Translucent Customized Cranial Implants Made of Clear Polymethylmethacrylate: An Early Outcome Analysis of 55 Consecutive Cranioplasty Cases. Ann Plast Surg 85:e27–e36.

Shenoy KV, Meeker D, Cao S, Kureshi SA, Pesaran B, Buneo CA, Batista AP, Mitra PP, Burdick JW, Andersen RA (2003) Neural prosthetic control signals from plan activity. NeuroReport 14:591.

Shimoda K, Nagasaka Y, Chao ZC, Fujii N (2012) Decoding continuous three-dimensional hand trajectories from epidural electrocorticographic signals in Japanese macaques. J Neural Eng 9:036015.

Shin J, Im C-H (2020) Performance improvement of near-infrared spectroscopy-based brain-computer interface using regularized linear discriminant analysis ensemble classifier based on bootstrap aggregating. Front Neurosci 14.

Singh A, Kusunose J, Phipps MA, Wang F, Chen LM, Caskey CF (2022) Guiding and monitoring focused ultrasound mediated blood–brain barrier opening in rats using power Doppler imaging and passive acoustic mapping. Sci Rep 12:14758.

Sitaram R, Zhang H, Guan C, Thulasidas M, Hoshi Y, Ishikawa A, Shimizu K, Birbaumer N (2007) Temporal classification of multichannel near-infrared spectroscopy signals of motor imagery for developing a brain–computer interface. NeuroImage 34:1416–1427.

Smith-Knapp K, Corrigan JD, Arnett JA (1996) Predicting functional independence from neuropsychological tests following traumatic brain injury. Brain Inj 10:651–661.

Snyder LH, Batista AP, Andersen RA (1997) Coding of intention in the posterior parietal cortex. Nature 386:167–170.

Snyder LH, Batista AP, Andersen RA (2000) Saccade-related activity in the parietal reach region. J Neurophysiol 83:1099–1102.

Sofroniew N et al. (2022) napari: A multi-dimensional image viewer for Python. Available at: https://zenodo.org/record/3555620 [Accessed February 13, 2023].

Soloukey S, Vincent AJPE, Satoer DD, Mastik F, Smits M, Dirven CMF, Strydis C, Bosch JG, van der Steen AFW, De Zeeuw CI, Koekkoek SKE, Kruizinga P (2020) Functional Ultrasound (fUS) During Awake Brain Surgery: The Clinical Potential of Intra-Operative Functional and Vascular Brain Mapping. Front Neurosci 13 Available at: https://www.frontiersin.org/articles/10.3389/fnins.2019.01384/full?report=reader [Accessed April 19, 2020].

Sorger B, Goebel R (2020) Chapter 21 - Real-time fMRI for brain-computer interfacing. In: Handbook of Clinical Neurology (Ramsey NF, Millán J del R, eds), pp 289–302 Brain-Computer Interfaces. Elsevier. Available at: https://www.sciencedirect.com/science/article/pii/B9780444639349000214 [Accessed March 9, 2023].

Sponheim C, Papadourakis V, Collinger JL, Downey J, Weiss J, Pentousi L, Elliott K, Hatsopoulos NG (2021) Longevity and reliability of chronic unit recordings using the Utah, intracortical multi-electrode arrays. J Neural Eng 18:066044.

Spüler M, Walter A, Ramos-Murguialday A, Naros G, Birbaumer N, Gharabaghi A, Rosenstiel W, Bogdan M (2014) Decoding of motor intentions from epidural ECoG recordings in severely paralyzed chronic stroke patients. J Neural Eng 11:066008.

Sugrue LP (2004) Matching behavior and the representation of value in the parietal cortex. Science 304:1782–1787.

Sugrue LP, Corrado GS, Newsome WT (2005) Choosing the greater of two goods: Neural currencies for valuation and decision making. Nat Rev Neurosci 6:363–375.

Sussillo D, Stavisky SD, Kao JC, Ryu SI, Shenoy KV (2016) Making brain–machine interfaces robust to future neural variability. Nat Commun 7:13749.

Svoboda K, Li N (2018) Neural mechanisms of movement planning: Motor cortex and beyond. Curr Opin Neurobiol 49:33–41.

Tadayon M, Pottie G (2020) Comparative analysis of the hidden Markov model and LSTM: A simulative approach. arXiv Available at: http://arxiv.org/abs/2008.03825 [Accessed March 3, 2023].

Taira M, Mine S, Georgopoulos AP, Murata A, Sakata H (1990) Parietal cortex neurons of the monkey related to the visual guidance of hand movement. Exp Brain Res 83.

Taylor DM, Tillery SIH, Schwartz AB (2002) Direct cortical control of 3D neuroprosthetic devices. Science 296:1829–1832.

Thier P, Andersen RA (1998) Electrical microstimulation distinguishes distinct saccade-related areas in the posterior parietal cortex. J Neurophysiol 80:1713–1735.

Tiran E, Ferrier J, Deffieux T, Gennisson J-L, Pezet S, Lenkei Z, Tanter M (2017) Transcranial functional ultrasound imaging in freely moving awake mice and anesthetized young rats without contrast agent. Ultrasound Med Biol 43:1679–1689.

Townsend BR, Paninski L, Lemon RN (2006) Linear encoding of muscle activity in primary motor cortex and cerebellum. J Neurophysiol 96:2578–2592.

Trautmann EM et al. (2021) Dendritic calcium signals in rhesus macaque motor cortex drive an optical brain-computer interface. Nat Commun 12:3689.

Trautmann EM et al. (2023) Large-scale brain-wide neural recording in nonhuman primates. bioRxiv:2023.02.01.526664.

Tsai PS, Kaufhold JP, Blinder P, Friedman B, Drew PJ, Karten HJ, Lyden PD, Kleinfeld D (2009) Correlations of neuronal and microvascular densities in murine cortex revealed by direct counting and colocalization of nuclei and vessels. J Neurosci 29:14553–14570.

Vadera S, Marathe AR, Gonzalez-Martinez J, Taylor DM (2013) Stereoelectroencephalography for continuous two-dimensional cursor control in a brain-machine interface. Neurosurg Focus 34:E3.

Vass LK, Copara MS, Seyal M, Shahlaie K, Farias ST, Shen PY, Ekstrom AD (2016) Oscillations go the distance: Low frequency human hippocampal oscillations code spatial distance in the absence of sensory cues during teleportation. Neuron 89:1180–1186.

Vingerhoets G (2014) Contribution of the posterior parietal cortex in reaching, grasping, and using objects and tools. Front Psychol 5.

Wandelt SK, Bjånes DA, Pejsa K, Lee B, Liu C, Andersen RA (2022a) Online internal speech decoding from single neurons in a human participant. medRxiv:2022.11.02.22281775 Available at: https://www.medrxiv.org/content/10.1101/2022.11.02.22281775v1 [Accessed January 13, 2023].

Wandelt SK, Kellis S, Bjånes DA, Pejsa K, Lee B, Liu C, Andersen RA (2022b) Decoding grasp and speech signals from the cortical grasp circuit in a tetraplegic human. Neuron 110:1777-1787.e3.

Wang T, Mitchell CJ (2011) Attention and relative novelty in human perceptual learning. J Exp Psychol Anim Behav Process 37:436–445.

Wang W, Degenhart AD, Collinger JL, Vinjamuri R, Sudre GP, Adelson PD, Holder DL, Leuthardt EC, Moran DW, Boninger ML, Schwartz AB, Crammond DJ, Tyler-Kabara EC, Weber DJ (2009) Human motor cortical activity recorded with Micro-ECoG electrodes, during individual finger movements. In: 2009 Annual International Conference of the IEEE Engineering in Medicine and Biology Society, pp 586–589. Minneapolis, MN: IEEE. Available at: http://ieeexplore.ieee.org/document/5333704/ [Accessed February 17, 2023].

Wang Z, Sampat M, Bovik A (2023) Complex-Wavelet Structural Similarity Index (CW-SSIM). MATLAB Central File Exchange Available at: https://www.mathworks.com/matlabcentral/fileexchange/43017-complex-wavelet-structural-similarity-index-cw-ssim [Accessed January 27, 2023].

Wardak C, Olivier E, Duhamel J-R (2004) A deficit in covert attention after parietal cortex inactivation in the monkey. Neuron 42:501–508.

Watrous AJ, Miller J, Qasim SE, Fried I, Jacobs J (2018) Phase-tuned neuronal firing encodes human contextual representations for navigational goals Behrens TE, ed. eLife 7:e32554.

Wessberg J, Stambaugh CR, Kralik JD, Beck PD, Laubach M, Chapin JK, Kim J, Biggs SJ, Srinivasan MA, Nicolelis MAL (2000) Real-time prediction of hand trajectory by ensembles of cortical neurons in primates. Nature 408:361–365.

Whitlock JR (2017) Posterior parietal cortex. Curr Biol 27:R691–R695.

Wilke M, Kagan I, Andersen RA (2012) Functional imaging reveals rapid reorganization of cortical activity after parietal inactivation in monkeys. Proc Natl Acad Sci USA 109:8274–8279.

Willett F, Kunz E, Fan C, Avansino D, Wilson G, Choi EY, Kamdar F, Hochberg LR, Druckmann S, Shenoy KV, Henderson JM (2023) A high-performance speech neuroprosthesis. bioRxiv:2023.01.21.524489.

Willett FR, Avansino DT, Hochberg LR, Henderson JM, Shenoy KV (2021) High-performance brain-to-text communication via handwriting. Nature 593:249–254.

Williams LM (2016) Precision psychiatry: A neural circuit taxonomy for depression and anxiety. The Lancet Psychiatry 3:472–480.

Wimalasena LN, Miller LE, Pandarinath C (2020) From unstable input to robust output. Nat Biomed Eng 4:665–667.

Wittevrongel B, Holmes N, Boto E, Hill R, Rea M, Libert A, Khachatryan E, Van Hulle MM, Bowtell R, Brookes MJ (2021) Practical real-time MEG-based neural interfacing with optically pumped magnetometers. BMC Biology 19:158.

Wolpaw JR, McFarland DJ (2004) Control of a two-dimensional movement signal by a noninvasive brain-computer interface in humans. Proc Natl Acad Sci U S A 101:17849–17854.

Wolpaw JR, McFarland DJ, Neat GW, Forneris CA (1991) An EEG-based brain-computer interface for cursor control. Electroencephalogr Clin Neurophysiol 78:252–259.

Wolpaw JR, Millán J del R, Ramsey NF (2020) Chapter 2 - Brain-computer interfaces: Definitions and principles. In: Handbook of Clinical Neurology (Ramsey NF, Millán J del R, eds), pp 15–23 Brain-Computer Interfaces. Elsevier.

Worsley KJ, Marrett S, Neelin P, Vandal AC, Friston KJ, Evans AC (1996) A unified statistical approach for determining significant signals in images of cerebral activation. Hum Brain Mapp 4:58–73.

Xie J, Chen J, Wei Q (2013) Repetitive transcranial magnetic stimulation versus electroconvulsive therapy for major depression: a meta-analysis of stimulus parameter effects. Neurol Res 35:1084–1091.

Yamamoto S, Monosov IE, Yasuda M, Hikosaka O (2012) What and where information in the caudate tail guides saccades to visual objects. J Neurosci 32:11005–11016.

Yin TC, Mountcastle VB (1977) Visual input to the visuomotor mechanisms of the monkey's parietal lobe. Science 197:1381–1383.

Zhang CY, Aflalo T, Revechkis B, Rosario ER, Ouellette D, Pouratian N, Andersen RA (2017) Partially mixed selectivity in human posterior parietal association cortex. Neuron 95:697-708.e4.

Zhu MH, Jang J, Milosevic MM, Antic SD (2021) Population imaging discrepancies between a genetically-encoded calcium indicator (GECI) versus a genetically-encoded voltage indicator (GEVI). Sci Rep 11:5295.